DISSERTATION

Advanced Methods for Mechanical Analysis and Simulation of Through Silicon Vias

ausgeführt zum Zwecke der Erlangung des akademischen Grades
eines Doktors der technischen Wissenschaften

eingereicht an der Technischen Universität Wien
Fakultät für Elektrotechnik und Informationstechnik
von

Anderson Pires Singulani

[redacted]

[redacted]

Wien, im Juni 2014

Abstract

Device miniaturization has steadily progressed since the invention of the integrated circuit in the 1950s. The many challenges which arose along the years were surpassed by advancements in processing technologies. Smaller devices meant more chips per wafer, lower power consumption, and higher speeds. Eventually, it is expected that device miniaturization will reach a limit and the basics elements of the current device technology have shown signs of weariness.

Naturally, several ideas have appeared with claims to overcome the challenges. Some involve the reformulation of a device or a process, while others involve enhancements of the current technology. Depending on the chosen path, the cost of implementation can be a drawback for the fast implementation of the technology by industry. It is not uncommon that a new semiconductor plant requires investments in the excess of two billion US dollars. It is unlikely that any industry would be willing to invest, in the short and middle term, in the development of technologies not compatible with their current plant. Therefore, a solution for the current integration problems should take into consideration the processing technologies available in the industry today.

Three-dimensional integration is a well balanced solution. It presents possibilities for an increase in device integration in every sense: device miniaturization, lower power consumption, and higher speeds. There are varying approaches for the manufacture of devices, but the majority relies on a “through silicon via” (TSV) to electrically bind the devices along the third dimension. The construction of a TSV is challenging, mainly due to its size. Among the required processing steps are the etching of high aspect ratio structures, wafer thinning, and several film depositions. A particular problem with TSVs is the mechanical stability of the structure and its influence on its surroundings. Such a large metal structure in the middle of the silicon circuit is prone to create a high level of stress during device operation and processing.

Within this work an extensive analysis of the mechanical aspects of the TSV is performed by means of simulations. A macro scale investigation of the mechanical effects of the TSV on its surroundings is performed. Subsequently, the via is analyzed locally, with a consideration of processing and handling scenarios. Lastly, microstructural effects are studied for the formation of residual stress during metal growth. The main objective is to provide a comprehensive characterization of the mechanical stability of the TSV, from its effects on the silicon circuit down to the manufacturing of the via. A collection of simulation techniques and models is developed and presented as the main contribution of this work.

Kurzfassung

Seit der Erfindung des integrierten Schaltkreises im Jahr 1950 schreitet die Miniaturisierung der Bauelemente kontinuierlich voran. Kleinere Bauelemente bedeuteten niedrigere Kosten, geringeren Energieverbrauch und höhere Geschwindigkeit. Früher oder später wird dieser Miniaturisierungsprozess an seine Grenzen stoßen und bereits jetzt ist zu erkennen, dass grundlegende Elemente Schwachstellen aufweisen.

Um die daraus resultierenden Herausforderungen zu bewältigen, wurden bereits verschiedene Ansätze entwickelt. Manche beinhalten die Verbesserung von bestehenden Technologien, während andere die Entwicklung von neuen Bauelementen beziehungsweise Fertigungsverfahren erfordern. Je nach Ansatz können die Kosten einen Nachteil darstellen, was die Einführung der Technologien in die Industrie erschwert. Eine Fertigungsanlage kann Investitionen in der Höhe von zwei Mrd. US Dollar erfordern. Es ist daher unwahrscheinlich, dass eine Industrie bereit ist, mittelfristig in die Entwicklung von Technologien zu investieren, die nicht zu ihrer Anlage kompatibel sind.

Dreidimensionale Integration gibt die Möglichkeit die Miniaturisierung der Halbleiterbauelemente voranzuführen und gleichzeitig den Energieverbrauch zu verringern und die Geschwindigkeit zu erhöhen. Es gibt eine Vielzahl an unterschiedlichen Ansätzen für die Herstellung eines dreidimensionalen Bauelements. Die meist verbreitetste Methode ist eine Durchkontaktierung durch das Silizium (through silicon via, TSV), um eine elektrische Verbindung in der dritten Dimension zu ermöglichen. Der Aufbau eines TSV ist vor allem wegen seiner Größe eine Herausforderung. Zu den notwendigen Schritten zählen das Ätzen von Strukturen mit einem großem Höhe zu Breite Verhältnis, Waferdünnung, und mehrere Schichtabscheidungen. Ein besonderes Problem, das TSVs mit sich bringen, ist die mechanische Stabilität des Aufbaus und ihr Einfluss auf ihre Umgebung. Solche großen metallischen Strukturen inmitten der Silizium-Schaltung sind während des Betriebs der Fertigung stressanfällig.

In dieser Arbeit wurde eine ausführliche mechanische Analyse von TSVs durch Simulationen durchgeführt. Die mechanischen Auswirkungen der TSVs auf ihre Umgebung wurden auf Makroebene untersucht. Anschließend wurde die Durchkontaktierung lokal analysiert. Abschließend wurden die makrostrukturellen Effekte, die zum Aufbau von Spannungen im Schichtsystem von TSVs während der Metallabscheidung führen, untersucht. Das Hauptziel war eine umfassende Charakterisierung der mechanischen Stabilität von TSVs vorzunehmen, welche die Auswirkungen auf den Silizium-Schaltkreis bis zur Herstellung der TSVs beinhaltet. Eine Reihe von Simulationstechniken und Modelle wurden entwickelt und als Mittelpunkt dieser Arbeit vorgestellt.

Resumo

A miniaturização de dispositivos eletrônicos progrediu regularmente desde a invenção do circuito integrado em 1950. Os muitos desafios ao longo dos anos foram superados por avanços nas tecnologias de fabricação de semicondutores. Eventualmente, espera-se que o processo de miniaturização atinja o seu limite, de fato elementos básicos da tecnologia atual de processamento tem mostrado sinais de desgaste.

Naturalmente, várias idéias surgiram para superar os atuais desafios da miniaturização. Algumas envolvem a reformulação de um dispositivo ou um processo, enquanto outras envolvem o aperfeiçoamento da tecnologia atual de processamento. Dependendo do caminho escolhido, o custo de implementação pode ser inconveniente para uma rápida adoção da tecnologia pela indústria. Uma nova fábrica de semicondutores pode demandar investimentos na altura de dois bilhões de dólares. É improvável que qualquer indústria esteja disposta a investir, a curto e médio prazo, para o desenvolvimento de tecnologias não compatíveis com a sua planta atual.

A integração em 3D é uma solução equilibrada. Ela apresenta possibilidades de um aumento na integração de dispositivos em todos os sentidos: miniaturização dos dispositivos, menor consumo de energia e maior velocidade. Existem diversas abordagens para a produção de um dispositivo 3D, mas a maioria baseia-se na construção de uma via através do silício (through silicon via, TSV) para ligar eletricamente os dispositivos ao longo da terceira dimensão. A fabricação de um TSV é complexa, principalmente devido ao seu tamanho. Dentre as etapas necessárias para o processamento encontram-se a criação de estruturas com alta razão de aspecto, redução da espessura do wafer e várias deposições de filmes finos. Um problema em particular com os TSVs é a estabilidade mecânica da estrutura e do seu entorno. Tal estrutura de metal no meio de um circuito integrado tende a originar um grande nível de estresse durante o funcionamento e o processamento do dispositivo devido a variações de temperatura.

Neste trabalho, uma extensa análise dos aspectos mecânicos do TSV é realizada por meio de simulações. Uma investigação dos efeitos mecânicos em macro escala do TSV em seus arredores é realizada. Em seguida, a via é analisada localmente, considerando diferentes cenários de processamento e manuseio. Por fim, os efeitos microestruturais são estudados para a formação da tensão residual durante o crescimento de metais no TSV. O principal objetivo é fornecer uma caracterização completa da estabilidade mecânica do TSV, desde seus efeitos sobre o integrado até a fabricação da via. Uma coleção de técnicas de simulação e modelos são desenvolvidos e apresentados como a principal contribuição deste trabalho.

Acknowledgement

I would like to thank Prof. Siegfried Selberherr for the opportunity to pursue my scientific goals, when it was only a distant ambition. I also appreciate his sympathy and support along the years, especially in the improvement of the quality of my work and to push me to take risks.

I am very grateful to Dr. Hajdin Ceric for his guidance, support, and kindness since the very beginning of my studies. I am thankful for his patience in reviewing my publications and for teaching me how to create a neat work.

I thank Dr. Roberto Lacerda de Orio and Dr. Lado Filipovic for their friendship, and all the support regarding immigration paperwork and personal matters. My first months in Vienna would have been much harder without their help.

I would also like to thank Dr. Filipovic for the thoughtful revision, suggestions, and comments to improve the quality of this work.

Additional thanks for all my friends and colleagues at the Institute for Microelectronics, especially for Dr. Josef Weinbub, Dr. Markus Bina, and Dr. Karl Rupp for creating such a nice and friendly environment in our office.

I am grateful to all my colleagues in ams AG for cheering me up during the writing of this work. Especially to Sara Carniello, for supporting me along this entire work and for pointing me out the path through mechanical simulations, and Andrea Kraxner for improving considerably the German version of the abstract of this dissertation.

To my parents, I shall remain grateful my entire life for showing me that the greatest gift a child can receive is a good education.

Lastly, to my beloved wife Emanuella, I am deeply grateful for her tenderness, patience, and love throughout the years. I appreciate sincerely all her efforts in the unfortunate task of being my first editor and reviewer. In addition, I could not let to acknowledge her ability to cheer up my spirit by preparing the greatest food in the darkest hours of my studies. Finally, I shall be eternally in debt with her for teaching me that, if one will embark in an adventure, one should never go alone.

Contents

List of Figures

List of Tables

List of Abbreviations

IC	Integrated circuit
ENIAC	Electronic numerical integrator and computer
TSV	Through silicon via
FEOL	Front-end of line
BEOL	Back-end of line
CTE	Coefficient of themal expansion
PDE	Partial differential equation
FEM	Finite element method
BVP	Boundary value problem
ODE	Ordinary differential equation
IVP	Initial value problem
BDF	Back differentiation formula
CVD	Chemical vapor deposition
PVD	Physical vapor deposition
CMOS	Complementary metal-oxide-semiconductor
GA	Genetic algorithm
PECVD	Plasma enhanced chemical vapor deposition
VW	Volmer-Weber

List of Symbols

$u(x, y, z)$	Displacement field
u_x	Displacement field in the x-direction
u_y	Displacement field in the y-direction
u_z	Displacement field in the z-direction
D_x	Difference between displacement fields in the x-direction
α , β	Congruent skew angles in the xy plane
γ , ϕ	Congruent skew angles in the yz plane
ω , θ	Congruent skew angles in the xz plane
ϵ_{ii}	Normal strain in the i-direction
γ_{ij}	Engineering shear strain in the ij plane
F	External force applied in a solid
A	Surface area
σ	Stress tensor
ϵ	Strain tensor
σ_{ii}	Normal stress in the i-direction
σ_{ij}	Shear stress in the ij plane
$T(e_x)$	Traction in the x-direction
$T(e_y)$	Traction in the y-direction
$T(e_z)$	Traction in the z-direction
c	Linear mapping between stress and strain
E	Young's modulus
ν	Poisson ratio
τ	Shear stress
G	Shear modulus
ΔT	Temperature variation
U_T	Total strain energy per unit of area
U_H	Hydrostatic strain energy per unit of area
U_D	Distortion strain energy per unit of area
V	Sub-space with infinity dimension of continuous with piecewise continuous derivatives
v	An element in V space
ϕ_j	FEM basis function
V_h	Discrete sub-space of V
u_h	A sample function in the sub-space V_h
v_h	A second sample function in the sub-space V_h
$P_{s-1}(t)$	Lagrangian polynomial in the BDF method
σ_{rr}	Normal stress in r direction of a cylindrical coordinate system

$\sigma_{\phi\phi}$	Normal stress in θ direction of a cylindrical coordinate system
σ_T	Thermal stress due to temperature variation
$B(t)$	Bézier polygon
$\dot{\gamma}$	Strain rate in the low temperature dislocation glide model
γ_0	Pre-exponential factor
ΔF	Activation energy of an obstacle
σ_s	Shear stress in the low temperature dislocation glide model
T	Temperature
T_0	Initial temperature
k	Boltzmann constant
$\hat{\tau}$	Shear stress required to trigger dislocations movement
ϵ_T	Thermal strain
ϵ_e	Elastic strain
ϵ_p	Plastic strain
σ_F	Stress in the film
M_f	Biaxial modulus
s	Schmid factor
δ_{ij}	Dirac delta
t	Time
$\dot{\epsilon}$	Strain rate tensor
$\dot{\epsilon_{ij}}$	Components of the strain rate tensor
E_1	System free energy per unit of area in Hoffman's model
E_0	Free surface energy per unit of area ot island's top in Hoffman's model
γ_{sv}	Free surface energy per unit of area of the island's lateral surface
γ_{gb}	Energy per unit of area spent in the formation of a grain boundary
Δ	Critical distance between two islands in Hoffman's model
E_2	Free energy per unit of area after coalescence in Hoffman's model
G_R	Strain energy release rate
K_f	Stress intensity factor
R	Island radius
Y_0	Height of island coalescence
Z_0	Maximum displacement of the island surface due to coalescence
E_{total}	Total energy in Seel's model
D_R	Deposition rate

1. Introduction

1.1. History of Device Integration Technology

By the end of World War II, the power of computational devices was brought to the society attention and, by the advent of mechanical and electrical machines, their advancement has reached the technological limits of the time. These machines were responsible for the automation of complex calculation procedures, such as projectile trajectories and cryptography. A famous example is the crack of the cryptography messages produced by the German machines known as Enigma [1]. At the time, the British army built a decrypt machine named Bombe based on an earlier Polish technology. The Bombe was 2.1m wide, 1.98m tall and 0.61m deep and weighted approximately one ton [1]. It was an enormous machine which was dedicated to perform an algorithm which fits today in a few hundreds lines of code and which can be executed in almost every modern computer. The technological revolution which allowed this miniaturization outbreak began in the mid of 1950s with the first steps towards the invention and realization of the integrated circuit (IC).

Contrary to common sense, IC invention was not driven mainly by miniaturization of electronic devices, but by the need for reliability [2][3]. The first general purpose computer known as ENIAC had 17468 vacuum tubes, 7200 crystal diodes, 1500 relays, 70000 resistors, 10000 capacitors and around 5 million hand-soldered joints [4]. Having a vacuum tube burn out was quite a common occurrence during the warm-up or cool-down process, and every failure had to be manually fixed. There are rumors which state that ENIAC has had a non-operation time of 50%, which is quite unlikely. At the height of ENIAC reliability technology the computer was able to operate, on average, every 2 days without burning a tube [5]. The invention of the transistor in 1947 eliminated the problems associated with the vacuum tubes as electronic devices became more reliable [6]. However, the need for more computation power required more devices. The huge amount of electronic devices led to the problem known as "Tyranny of numbers" [6]. The design of new devices was very complex and the amount of wiring connections required between the components was absurd, considering they all needed to be done manually. A solder fail was quite a frequent event which was very difficult to locate and to diagnose.

Circuit integration was presented as a solution for this reliability problem [2][3][6]. The idea of manufacturing electronic components in a monolithic piece of semiconductor was very tempting. The number of manually wired connections would be drastically reduced and more than one device could be manufactured at once, reducing the production costs. However, circuit integration faced three major challenges at the beginning of the 1950s [7]. First, for the integration itself, there was no available technology which was able to create different components on a single semiconductor substrate. Second, the isolation: if a multiple number of components were successfully produced in a single substrate, they would need to be electrically isolated from each other. However, nobody really knew how to do this, at the time. Lastly, the interconnections: there was no financially feasible solution to electrically connect the integrated components.

The first successful solution for integration was developed by Jack Kilby in the summer of 1958 [8][9]. He realized that all circuit elements (e.g. resistors and capacitors) could be made using a semiconductor material, moreover they can be formed on a single substrate. Kilby used several earlier developments such as mesa transistor and mesa diodes to build a single-transistor oscillator with a distributed RC feedback. It is considered by many the first IC ever made, a schematic of which is shown in Fig. 1.1 [2][3].

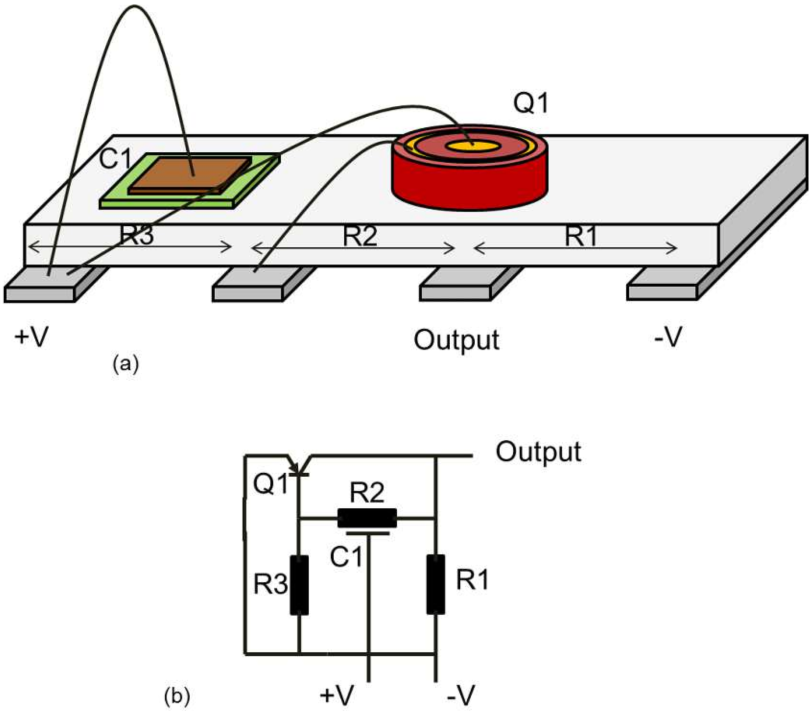

Figure 1.1.: Kilby's device with mesa components (a) and circuit description of the single-transistor oscillator (b). Image based on [8].

Kilby's biggest contribution was to show that any electrical component could be built in a single chip. However, his implementation had some flaws; the device isolation was made by cutting grooves and the connections were manually wired.

At the end of 1958, Kurt Lehovec developed a method to electrically isolate multiple components which are placed on a single substrate[10]. He claimed that the use of several p-n junctions in series could prevent current flow between the elements. The junction could be biased, if needed, in the blocking direction. Lehovec's idea was successfully tested using the structure depicted in Fig. 1.2.

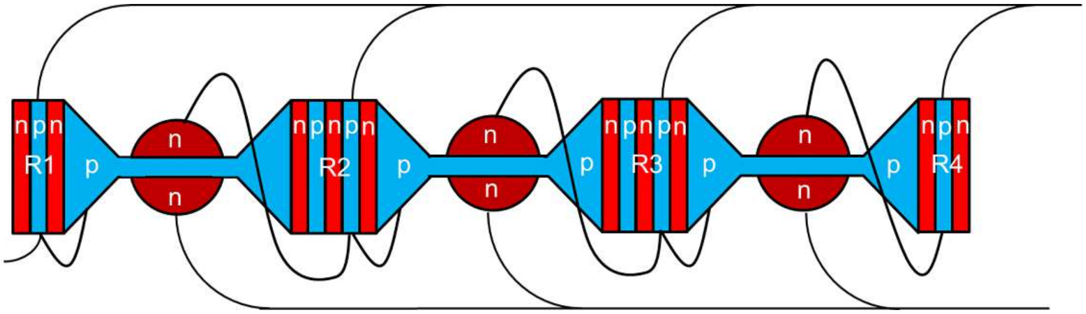

Figure 1.2.: Schematic of the device constructed by Lehovec. The PN junction in series works as a barrier to prevent the undesired current flow through the silicon. Image based on [10].

In 1959 Robet Noyce developed, based on Jean Hoerni's work, the manufacturing process, which would enable the adaptation of ICs on large scale. He adapted the ideas of Kilby and Lehovec to the new planar transistor developed by Hoerni [11]. The process of planar transistor fabrication is very similar to the manner in which devices are fabricated today. The process is initiated with an undoped silicon wafer covered by a layer of silicon oxide. Then, a window is opened by photolithography in the corresponding device planned location. Finally, impurities are diffused to form the conduction wells and the planar transistor is complete. A summary of the process is depicted in Fig. 1.3.

In addition to the planar process, Noyce developed a method to make the electrical connections of the devices without manual intervention. The idea was quite obvious after the development of the planar transistor; it consists of the preservation of the oxide layer on the top of the device (except on the contact points with the active regions). In that way, metal layers could be deposited on the oxide, which would work as isolation between the metal interconnections and the substrate.

The invention of ICs was the object of discussion for several years, which led to a patent war between several leading electrical companies [2]. For many years the invention was mainly accredited to Jack Kilby and Robert Noyce. But in 2000, only Jack Kilby received the physics Nobel prize "for his part in the invention of the integrated circuit" [12]. This led to a new debate of the legitimate inventors of the IC, but in the end the invention of the IC is viewed as a collaborative result with contributions from several engineers and scientists, which improved the fabrication process step by step until enabling mass production.

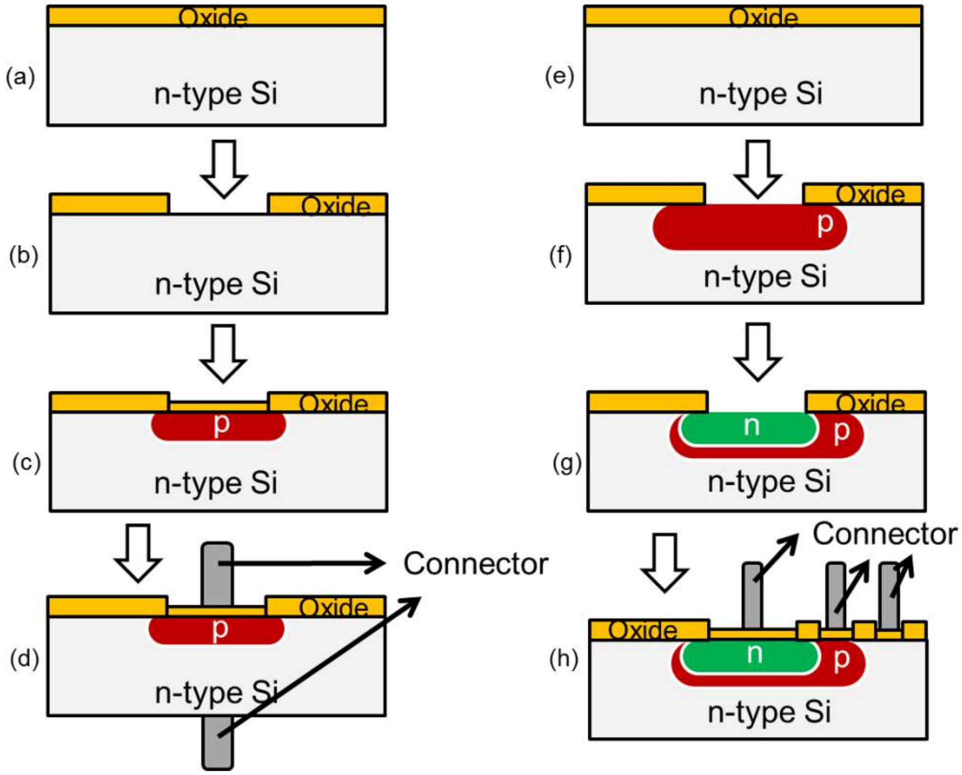

Figure 1.3.: Description of the planar process developed by Jean Hoerni for a diode (left side) and a transistor (right side). A sample of an n-type Silicon substrate is prepared with silicon oxide on top (a and e). In predetermined regions the oxide is etched (b and f), opening spots for impurity diffusion (c, f, and g). After diffusion, an oxide layer is regrown in the etched openings and the metal contacts are deposited (d and h). Image based on [11].

1.2. Limitations of the Current Technology

After the successful invention of the IC, the benefits of continuous integration became evident as time progressed. Smaller devices yielded higher speed, lower power consumption, and reduced manufacturing costs, since it was possible to produce more devices on a single wafer [13]. Gordon Moore, a renowned pioneer in the semiconductor industry, predicted in 1965 that the number of transistors on IC would double approximately every two years, a trend shown in Fig. 1.4 [13][14]. His estimative has been proven accurate through the years, but such exponential growth cannot persist indefinitely. A minor slow-down in the miniaturization pace has already been detected and leading foundries have been discussing the post-Moore era [15][16][17].

Further integration in the current semiconductor technology is bounded by device operation and processing limitations. A not exhaustive list is presented below with the most common scaling problems for various applications.

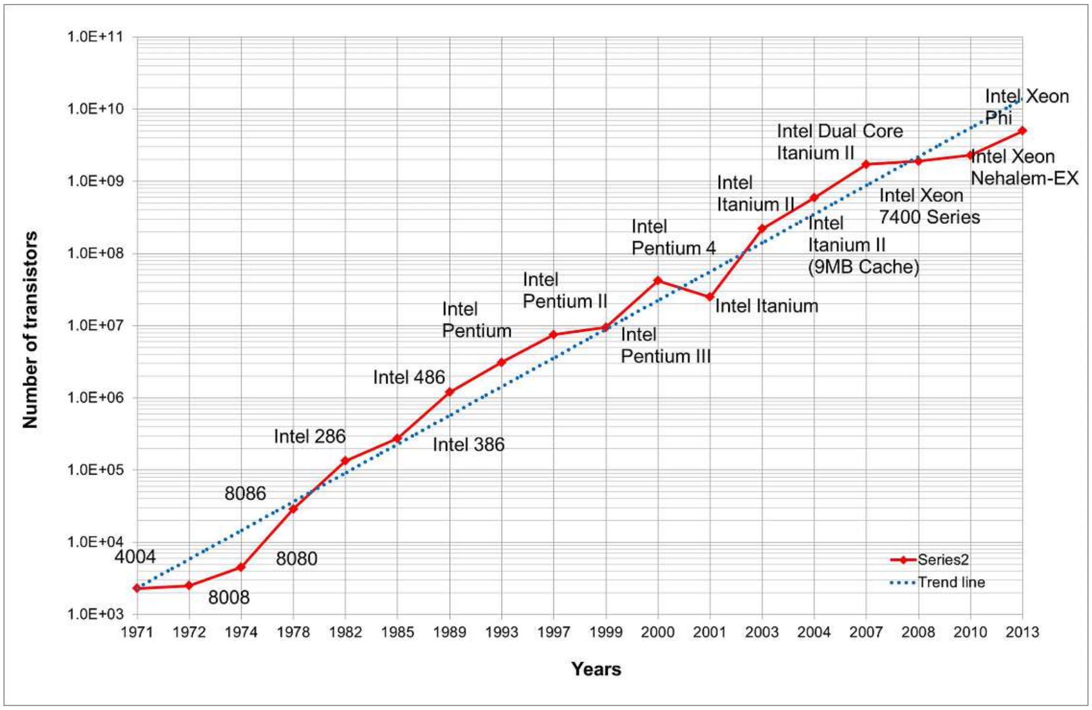

Figure 1.4.: Moore's law in semi-log scale.

Current Leakage

When analyzing digital circuits, a transistor has two modes of operation: "on" and "off". Ideally, the current flows through the device only, when the transistor is "on". During the "off" state the flow is blocked and there is no power consumption. In real devices the "off" state is not completely free of power consumption. There is a small current flow, which should be negligible in comparison to the "on" state. Such undesired flow of current in a transistor is defined as current leakage [18].

As the devices get smaller current leakage increases mainly by two mechanisms. The first is known as gate leakage. It occurs due to the thin gate isolation in smaller devices. In that situation the electrons present in the gate tunnels to the conducting channel, deteriorating the transistor operation. The second mechanism is the subthreshold leakage. The channel length and threshold voltage of a transistor decreases as the overall device size decreases. The reduction of these two parameters increases the current flow between drain and source during "off" state. Leakage currents are severe problems of modern devices fabrication and, in some cases, they can account for more than 50% of the device's power consumption [19].

Process Variation

Smaller devices are very susceptible to eventual processing deviations. For example, as described by Haselman and Hauck [18], the gate oxide in current devices is only five atoms thick. A misplacement of only one atom can modify the device design specification by 20%. Such sensitivity of device fabrication can damage yield and increases fabrication costs.

Lithography

For many years, lithography improvements were made by enhancements on the lens, improvements in the imaging material technology, and the reduction of the source wavelength. Naturally, it is expected that at some point the feature size becomes smaller than the resolution power of optical systems [18][20]. In fact, such a situation is already true in modern lithography technology. The 32nm node had to implement advanced optical techniques such as, optical proximity, phase-shift masks, and immersion lithography [21]. However, those enhancements are not enough for the 22nm and 16nm nodes, and new advancements in pattern transfer are needed [20][21] [22][23].

Interconnections

The increasing integration of devices demands longer and thinner interconnects. Such conditions lead to slower interconnections and higher power dissipation, increasing the device temperature during operation. Low resistivity metals and low-k oxides are currently employed to ease the Joule dissipation and signal delay, respectively [24]. However, they suffer from processing and reliability problems which can lead to increased production costs. The interconnection can be engineered in a more efficient way with the development of optical interconnects and three-dimensional (3D) integration technologies.

1.3. Three-Dimensional Integration and TSVs

Since the development of the planar process, the integration paradigm is to increase the number of devices on the wafer surface. However, one can clearly see that there is plenty of available space along the depth of the wafer. What prevented its utilization was the lack of processing know-how to handle three-dimensional (3D) integration. Furthermore, there was no commercial reason to invest in vertical integration, since planar devices sufficed so far. However, in the last decade, the scenario has changed due to the limitations presented in Section 1.2, and the proper use of the third dimension provides an alternative to continue along the miniaturization path. Moreover, 3D integration promises additional benefits, such as increased bandwidth, reduced power consumption, improved performance, and multi-functionality [25].

1.3.1. Types of Three-Dimensional Integration

There are at least three different modes to implement 3D integration: Monolithic, die stacking, and wafer stacking [25]. The first relates to the construction of two or more device layers in one single wafer. The other two consist of piling up multiple die or wafers and a connection through the intermittent layers, as depicted in Fig. 1.5.

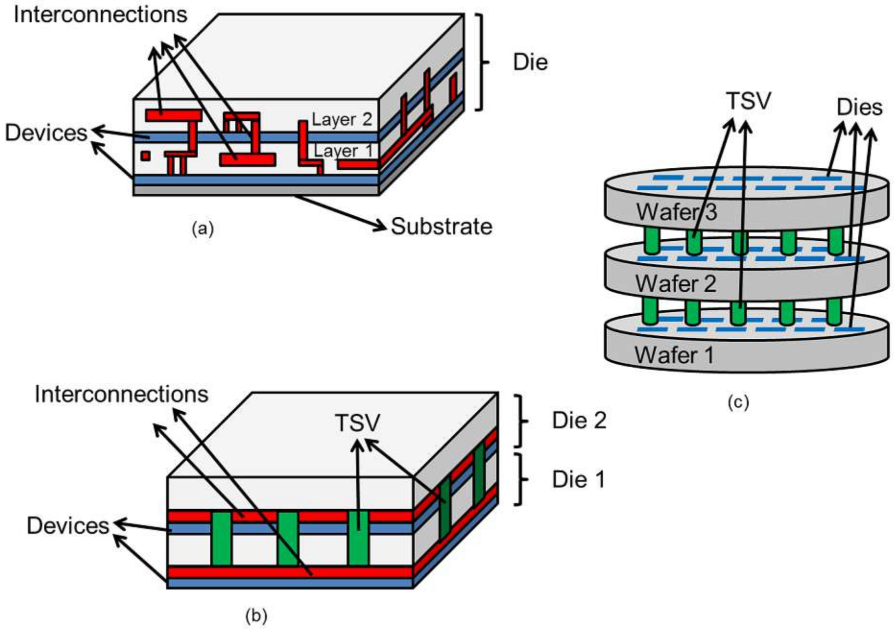

Figure 1.5.: Different implementations of a 3D IC: Monolithic device (a), Die-to-die integration (b), and Wafer-to-wafer integration (c).

Naturally, every approach has a specific process to reach its final configuration. The maturity of the technology and the process involved in the fabrication will determine the mode to be adopted by industry. Monolithic devices are the farthest from commercial use and there are few reports from companies using this technology [26][27], while for die and wafer stacking there is a variety of publications from the industry and academy [28][29].

Die or wafers stacking presents similar challenges due to the nature of the concept. However, a very specific requirement for both methods is the communication between different stacked layers. A vertical interconnection is needed to go through the entire wafer in order to bind the devices in a 3D network. Those interconnections are known as Through Silicon Vias (TSV). The importance of the TSVs for the successful implementation of 3D integration is reflected in the great amount of literature available.

1.3.2. TSV Fabrication

TSVs are big vertical interconnections, usually made of metal. The structure can be bulky (filled TSV) or hollow (unfilled TSV) depending on the design and process requirements. TSV fabrication can be split in 4 steps: Etching, metal deposition, wafer thinning, and bonding [30][31].

The Bosch process is usually employed to etch the planned TSVs wells, but other processes such as Non-Bosch DRIE and Laser drilling can be used. Subsequently, a metal or poly-Si is deposited in order to create the conduction path inside the via. However, it is very tough to produce a TSV which is long enough to go through the entire depth of a commercial wafer (∼750μm). Hence, in addition to the TSV building, a polishing process is needed to reduce the wafer thickness. After polishing, the wafers (or die) are aligned and piled upon each other using a bonding process shown in Fig. 1.6.

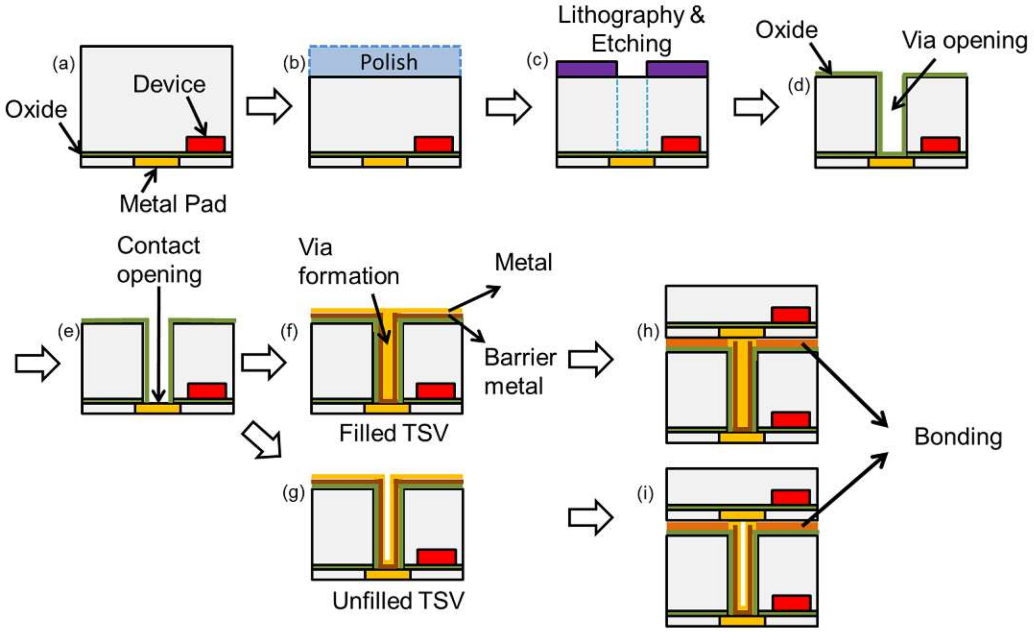

Figure 1.6.: Typical processing of a TSV. A Die (or wafer) ready (a) for TSV manufacturing is polished (b) on its backside to reduce the thickness. In the following, the sample is structured by photolithography (c) and the via hole is etched (d). Then, the metal pad is exposed (e) and the conduction metal is deposited (f and g), accordingly to the TSV type. Finally, the die (or wafers) are stacked and bonded.

1.3.3. Via First, Via Middle, and Via Last

The execution order of the TSV fabrication steps depends on the chip fabrication stage at which the via is formed. There are three approaches available [32]: before the devices fabrication (Via first), before metal lines fabrication (Via middle) and after metal lines fabrication (Via last), as sketched in Fig. 1.7.

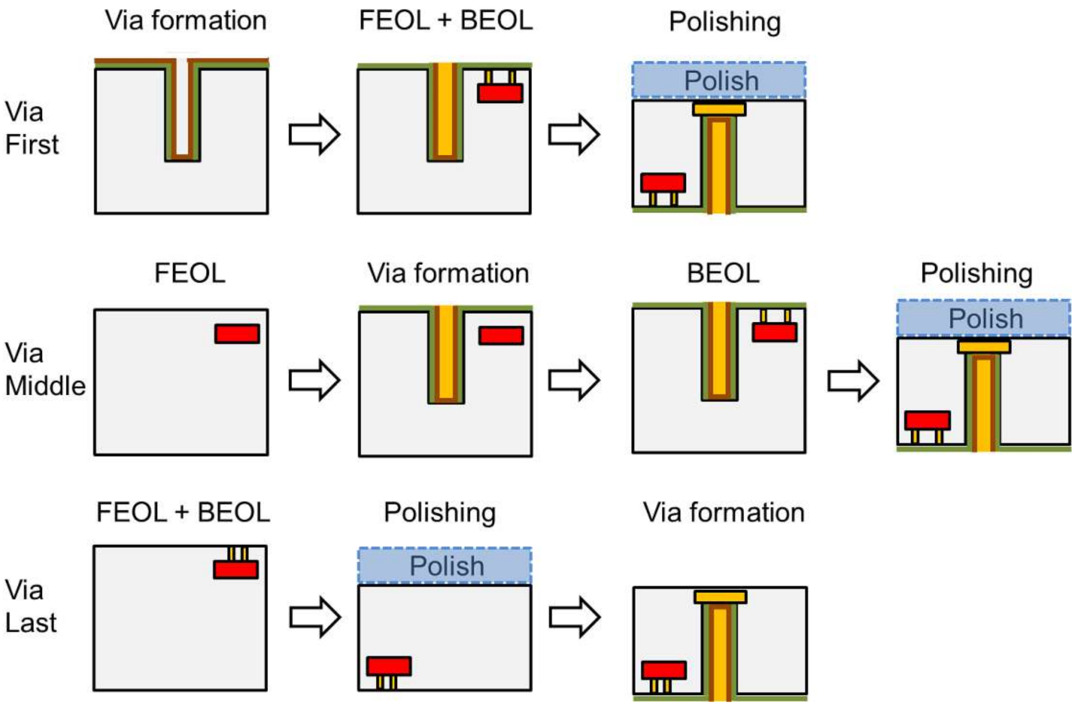

Figure 1.7.: The three main approaches for TSV fabrication: Via First, Via Middle and Via Last. Image based on [32].

1.4. Challenges and Opportunities

There are many expectations surrounding 3D integration [31]. Some commercial applications are already available on the market, but there is a general feeling in the engineering community that a "killer application" is missing. Actually, the mass production of 3D devices in the mainstream is not yet a reality. The technology still faces many challenges [33]. In the processing steps, TSVs suffer from high mechanical and thermal stresses, which compromises their structural stability. Obtaining a high yield is also a concern, since an economically viable yield rate is difficult to achieve. There are also open concerns during device operation, such as thermal management being of particular concern. The piling up of devices can hinder the thermal dissipation and temperatures beyond the devices' operation range can be easily reached. In addition to the process and operation issues there is also a lack of software design tools. A 3D IC needs a specific tool for design and the currently available software is unable to handle the particularities of this technology. Finally, the last obstacle involves test. New methodologies to probe the devices are needed, especially the devices which are found in the lower layers.

Judging by the amount of obstacles, it appears unlikely that the realization of 3D IC technology is feasible in the near future in a large volume. However, such analysis shows a very pessimistic view. The 3D IC technology based on TSVs is already available on some markets for commercial applications, especially sensors and digital cameras [34][35]. Naturally, very high density integration is not the goal of these markets but they point in the direction which could lead to solving the problems associated with this technology. TSVs are also being employed in so called 2.5D technologies such as interposers [36]. The dies are not piled up but instead, they can be placed closer to each other, thereby reducing metal lines length as depict in Fig. 1.8.

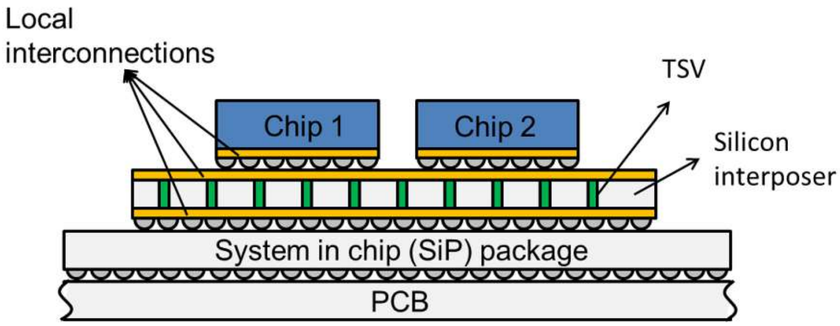

Figure 1.8.: A conceptual example of 2.5D technology. The silicon interposer is used to reduce the connection paths between the chips.

1.5. Outline of the Thesis

This work contains ultimately a collection of techniques to assess the impact of TSVs in silicon-based technologies. The goal of the work is to present a comprehensive analysis of the mechanical behavior of TSVs in different scenarios by means of simulations. In order to fulfill the objective, new simulation schemes, material and mechanical models were developed. They constitute a substantial part of the work and are described in detail in the sections to follow.

This dissertation is divided into seven chapters, including this introductory chapter. Chapter 2 and Chapter 3 provide the general background for the approach taken for the simulation of mechanical problems in TSVs. In Chapter 2, the classical mechanics theory is explained with a focus on microelectronics applications. In the chapter to follow, the mathematical fundamentals of the simulation techniques used are discussed. Chapter 4, Chapter 5, and Chapter 6 present the developed novel approaches and form the bulk of this thesis. The flow of the document starts with the analysis of TSVs on a macro scale and move toward a micro scale analysis. Chapter 4 considers the TSV as a big structure on a silicon wafer and discusses the mechanical impact in its neighborhood. Chapter 5 deals with the local stress in the TSV, which is created by small features, processing, and handling. Chapter 6 closes the work describing an estimation for residual stress in the metal layers of the TSVs. Finally, Chapter 7 summarizes the thesis with the main achievements and presents an outlook for further steps.

2. Mechanics in Microelectronics

The mechanics reliability problems in microelectronics require a careful approach. The small dimensions and the thin layers modify the material behavior, leading to the development of phenomena not yet fully understood. This chapter presents the basic framework common to all mechanics problems in engineering. Meanwhile, the specifics in dealing with the mechanics of the TSV structure are described in Chapter 4, Chapter 5 and Chapter 6.

2.1. Mechanical Systems

A semiconductor device is a complex piece of engineering. Its concept and operation span through electronics, optics, materials science, and several other fields of science. A proper understanding and control of such technology demands a multidisciplinary approach. For instance, using strained semiconductors is a relatively old field – but still very active – in which the main goal is to understand how stress and strain impact the carriers' mobility in the device. In order to have full comprehension of strained devices, one should consider a combined knowledge from electronics, mechanics, and materials science. The overlap between disciplines in semiconductor research and development is quite common. Therefore, mechanics in microelectronics requires a different approach by the engineer who must consider the interaction between several physical and chemical phenomena.

Mechanical stress in microelectronics arises mainly from two sources: intrinsic stress of films and thermal stress. Those effects are present in front-end of line (FEOL) processes, back-end of line (BEOL) processes, packaging, and device operation [37]. The device is under stress during its entire lifetime and the invention of a technology which neglects it is quite unlikely. Thus, one can only try to manage the stress, either by taking advantage of it or limiting its effects in order to prevent damage to the device.

To control the stress, engineers use the structural geometry of the device, material properties, thermal management, and different manufacturing techniques. However, stress management is a difficult task, especially in microelectronics. The small scale of layers and components invalidate some aspects of classical mechanics theory. Additionally, materials' microstructural effects play a significant role in such dimensions and cannot be neglected. Even material properties can be different when comparing thin films and bulk films with the same material composition [38]. Well documented bulk material properties cannot be used freely in small structures. Sometimes a relationship can be traced between them, but this is not always the case. Naturally, experimental procedures are used to extract material properties, but to complete this task, experimentalists face challenges of their own. In summary, mechanics in microelectronics is a multiscale physical problem, where at small dimensions, the modification of material properties gives rise to new physical effects.

2.2. Mechanical Theory

Atoms of a solid object move as response to an applied force. This movement changes the object's shape and size, and it is called deformation [39]. A deformation can be temporary or permanent. A temporary deformation is reversible and linearly dependent on the applied force. When the force ceases to exist, the object returns to its original size and shape. This behavior of solids is called elasticity. On the other hand, permanent deformations are usually non-linearly dependent on the applied force and, as the name suggests, are irreversible. This behavior is called plasticity. The vast majority of materials presents both elastic and plastic behavior depending on how big the applied force is. A typical evolution of deformation regarding force is shown in Fig. 2.1.

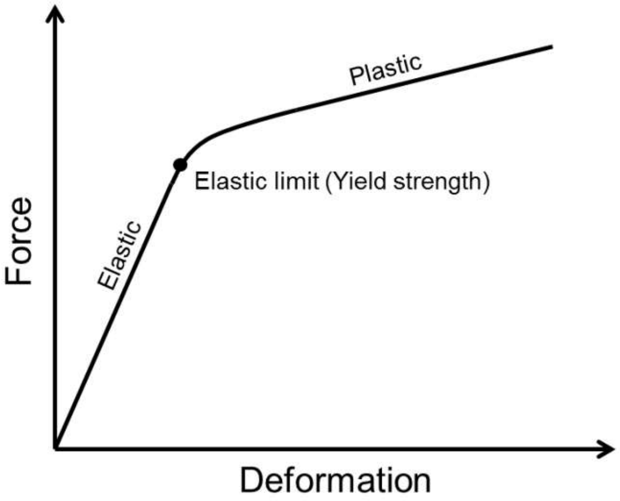

Figure 2.1.: Relationship between force and deformation. The linear region is known as the elastic regime and any deformation in this regime is temporary and ceases to exist after unloading. Beyond the elastic limit the deformations become permanent and the material enters the plastic regime.

In order to quantitatively study the deformation of solids, a traditional approach is to look at the material as a continuum [39]. This means that the solid is not considered as a set of arranged atoms, but rather it is treated as a body of matter without empty spaces and every point has the same properties, even if it is sub-divided infinitesimally. Therefore, the solid is treated as a single material defined by its geometry and confined to a single set of parameters. With these considerations, it is possible to describe mathematically the elastic portion of the graphics in Fig. 2.1 for small deformations.

2.2.1. Infinitesimal Strain Theory

Infinitesimal strain theory describes solid behavior for deformations much smaller than the body dimensions [37][39]. Qualitatively, this means that the body geometry is assumed unchanged during the deformation process. It can sound inconsistent, but it is the most common situation for solids. For example, when a car drives over a bridge, it certainly applies some force on the bridge and such force leads to some deformation. However, one can say that the bridge remains immutable, since any deformation is irrelevant, when the full enormity of the bridge is considered. For an engineer it is still important to know the effect which the car has on the bridge. For that analysis, the infinitesimal strain theory is applied.

There are two different ways to describe very small deformations of solids. The first one is based on the linearization of Lagrangian or Eulerian strain tensors of finite strain theory [40], a generalization of infinite strain theory. The second method is a geometric based description, which is derived in the section which follows.

Strain Tensor Derivation

Consider the infinitesimal volume of a solid as in Fig. 2.2a. Due to some external influence (e.g. force, heat) this infinitesimal body is deformed, assuming the shape of the Fig. 2.2b. Deformation can be quantified as the amount of elongation, contraction or torsion an infinitesimal side suffers.

The displacement field accounts for every movement inside the solid, therefore rigid body translation and rotation are included. To measure the deformation of a body, the side ab can be taken into consideration. The deformation of the side ab ($\boldsymbol{D_x}$) is given by the difference between the displacement vectors ($\boldsymbol{u}(x, y, z)$) of the points b and a

$$\boldsymbol{D_x} = \boldsymbol{u}(x + dx, y, z) - \boldsymbol{u}(x, y, z) \ . \tag{2.1}$$

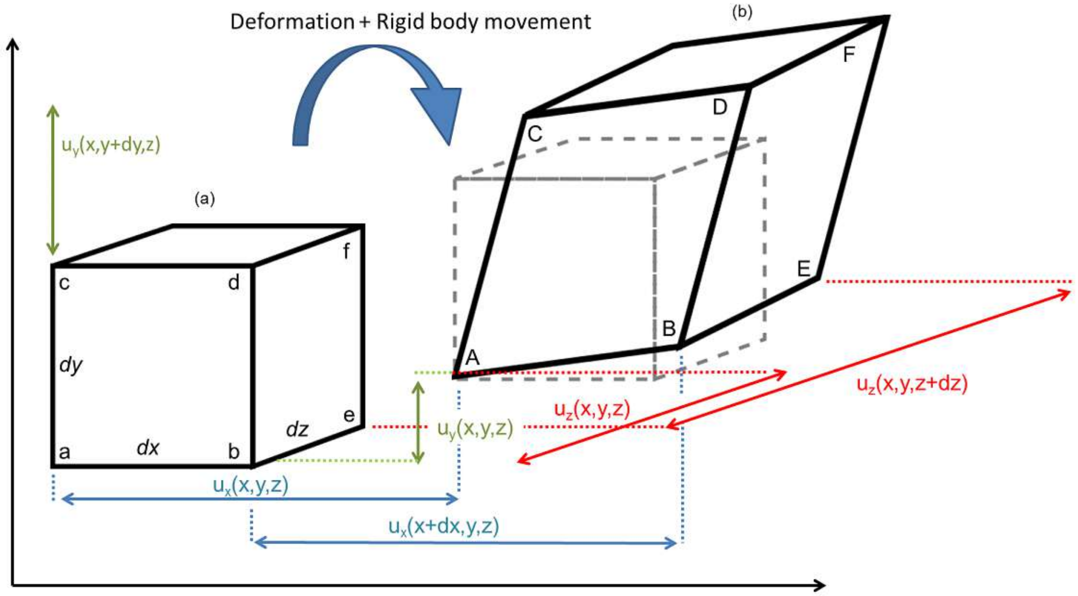

Figure 2.2.: General deformation of a body after external loading. Rigid body movements such as translation and rotation are included, although they should not count for the final body deformed state.

The vector $\boldsymbol{D_x}$ can be explicitly defined in terms of each of its components

$$\boldsymbol{D_x} = \begin{bmatrix} u_x(x+dx,y,z) - u_x(x,y,z) \\ u_y(x+dx,y,z) - u_y(x,y,z) \\ u_z(x+dx,y,z) - u_z(x,y,z) \end{bmatrix} \quad . \tag{2.2}$$

The first term of each component can be expanded in Taylor series as shown in (2.3). Only the term for u_x is shown for the sake of brevity:

$$u_x(x+dx) = u_x(x,y,z) + \frac{\partial u_x}{\partial x}dx + O(dx^2) \ . \tag{2.3}$$

Since very small deformations are considered, any term of the second order can be ignored and the vector $\boldsymbol{D_x}$ is rewritten as in

$$\boldsymbol{D_x} = \begin{bmatrix} \dfrac{\partial u_x}{\partial x}dx \\ \dfrac{\partial u_y}{\partial x}dx \\ \dfrac{\partial u_z}{\partial x}dx \end{bmatrix} \quad . \tag{2.4}$$

The vector $\boldsymbol{D_x}$ specifies the extent of the deformation of the side ab in the direction of the three coordinate axis. However, it is more convenient to express the deformation in normalized units related to the original ab size (dx) as in

$$\boldsymbol{\epsilon_x} = \frac{\boldsymbol{D_x}}{dx} = \begin{bmatrix} \dfrac{\partial u_x}{\partial x} \\ \dfrac{\partial u_x}{\partial y} \\ \dfrac{\partial u_x}{\partial z} \end{bmatrix} . \tag{2.5}$$

This relative measure of deformation is known as strain. This definition provides a better feeling of how much the solid has changed in comparison to the undeformed solid. The strain in the original direction of the side ab (x-direction) is called normal strain ($\partial \boldsymbol{u}/\partial x$). It reflects the tendency of the points, originally aligned (in this case, parallel to x-axis), to move away (stretch) or to approach (contract) each other along the same direction of the side ab. The deformation of the other two components of $\boldsymbol{e_x}$ describes the tendency of the points to skew in relation to each other toward the direction of each component (y or z). The same procedure can be repeated for each side (cd and ef) parallel to the coordinate axis of the infinitesimal solid. The same result holds, except for an index change.

$$\boldsymbol{\epsilon_y} = \begin{bmatrix} \dfrac{\partial u_x}{\partial y} \\ \dfrac{\partial u_y}{\partial y} \\ \dfrac{\partial u_z}{\partial y} \end{bmatrix} , \tag{2.6}$$

$$\boldsymbol{\epsilon_z} = \begin{bmatrix} \dfrac{\partial u_x}{\partial z} \\ \dfrac{\partial u_y}{\partial z} \\ \dfrac{\partial u_z}{\partial z} \end{bmatrix} . \tag{2.7}$$

The skew deformations are related to the angles formed between the original sides and the deformed sides as defined in Fig. 2.3 (α, β, γ, ϕ, θ, and ω). For example, the angle α can be expressed in terms of the skew y-component according to

$$\tan\alpha = \frac{\dfrac{\partial u_y}{\partial x}dx}{dx + \dfrac{\partial u_x}{\partial x}dx} = \frac{\dfrac{\partial u_y}{\partial x}}{1 + \dfrac{\partial u_x}{\partial x}} . \tag{2.8}$$

Where, for $\alpha << 1$ the relation (2.8) can be further simplified by

$$\alpha \approx \frac{\partial u_x}{\partial y} \, . \tag{2.9}$$

A similar relation also holds for β regarding the skew x-component.

A common method to measure the skew of a solid is to sum up the angular deviation in a particular coordinate plane. For example the skew of the solid in the plane-xy is given by the sum of α and β. For the plane-xz is the sum of θ and ω, and for the plane-yz is the sum of ϕ and γ. This measure is called shear strain.

In summary, a solid deformation is represented by 3 normal strain components (one for each direction) and 3 shear strain components (one for each coordinate plane). The usual nomenclature is stated below and the geometrical view of the strained component is sketched in Fig. 2.3.

$$\begin{array}{ccc} \varepsilon_{xx} = \dfrac{\partial u_x}{\partial x} & \varepsilon_{yy} = \dfrac{\partial u_y}{\partial x} & \varepsilon_{zz} = \dfrac{\partial u_z}{\partial x} \\ \gamma_{xy} = \dfrac{\partial u_x}{\partial y} + \dfrac{\partial u_y}{\partial x} & \gamma_{xz} = \dfrac{\partial u_x}{\partial z} + \dfrac{\partial u_z}{\partial x} & \gamma_{yz} = \dfrac{\partial u_y}{\partial z} + \dfrac{\partial u_z}{\partial y} \end{array} \tag{2.10}$$

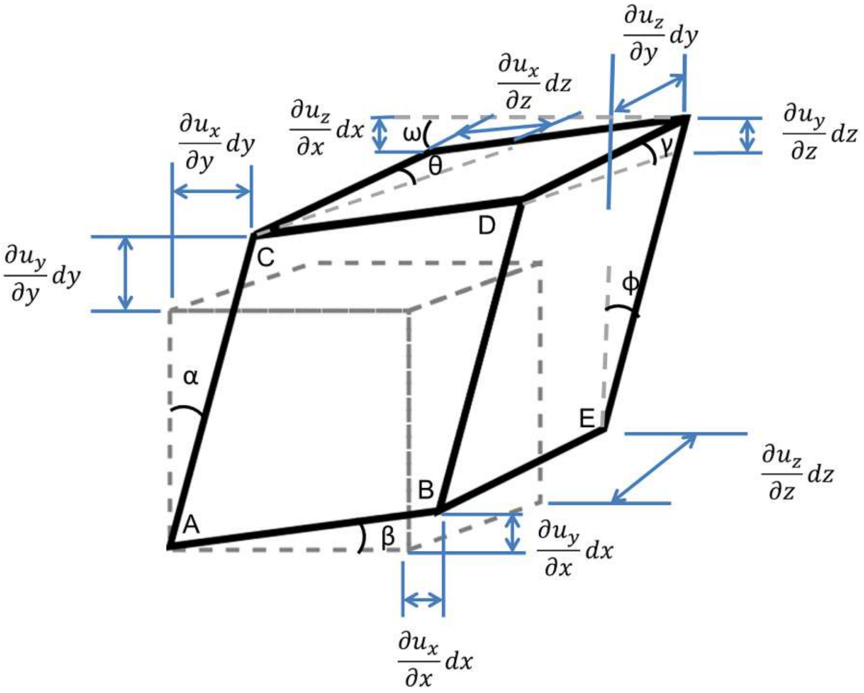

Figure 2.3.: Geometrical representation of the normal and shear strain.

For mathematical handling, it is very convenient to represent the strains of a solid deformation as a tensor:

$$\begin{bmatrix} \varepsilon_{xx} & \varepsilon_{xy} & \varepsilon_{xz} \\ \varepsilon_{yx} & \varepsilon_{yy} & \varepsilon_{yz} \\ \varepsilon_{zx} & \varepsilon_{zy} & \varepsilon_{zz} \end{bmatrix} = \begin{bmatrix} \varepsilon_{xx} & \dfrac{\gamma_{xy}}{2} & \dfrac{\gamma_{xz}}{2} \\ \dfrac{\gamma_{yx}}{2} & \varepsilon_{yy} & \dfrac{\gamma_{yz}}{2} \\ \dfrac{\gamma_{zx}}{2} & \dfrac{\gamma_{zy}}{2} & \varepsilon_{zz} \end{bmatrix} . \tag{2.11}$$

The factor 1/2 is added in order to simplify the manipulation of constants in future applications of the strain tensor. The strain tensor is symmetric and has 3 components not discussed previously, namely ϵ_{yx}, ϵ_{zx}, and ϵ_{zy}, where $\epsilon_{yx} = \epsilon_{xy}$, $\epsilon_{zx} = \epsilon_{xz}$, and $\epsilon_{zy} = \epsilon_{yz}$. Those components represent the complement of the skew angles in each coordinate plane, as depicted in Fig. 2.4.

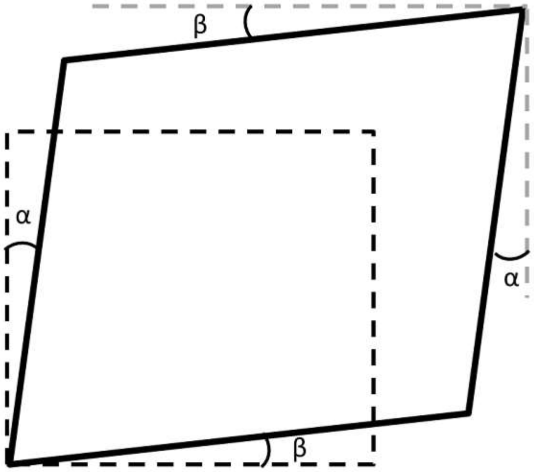

Figure 2.4.: Complementary angles in the plane xy. The indicated angles on the bottom left corner of the quadrilateral are equal to those on the upper right corner, due to triangle symmetry.

Stress

Every solid body reacts to deformations. Internal forces arise in the solid as a response to strain, similar to the restoration force in a spring. These forces are known as stress and act to restore the undeformed state of the body [39]. Stress might have several sources: it can be a reaction to external forces, temperature variation, or electromagnetic fields (e.g. piezoelectric devices). Stress can also arise during material fabrication, due to microstructural phenomena. Those are referred to as residual stress or intrinsic stress. An example is the formation of metal lines for semiconductor devices. The characteristics of the metal growth process and the particular interaction between the metal and silicon create residual stress in the lines. The same situation occurs in oxide growth, material deposition, and any other process which involves the introduction of new materials during thin films fabrication.

The stress is defined qualitatively as the force between adjacent parts of a solid acting on an imaginary surface, divided by the area of this surface, as sketched in Fig. 2.5. The force's magnitude and direction usually depend on the chosen surface. The situation depicted in Fig. 2.6 is used as an example.

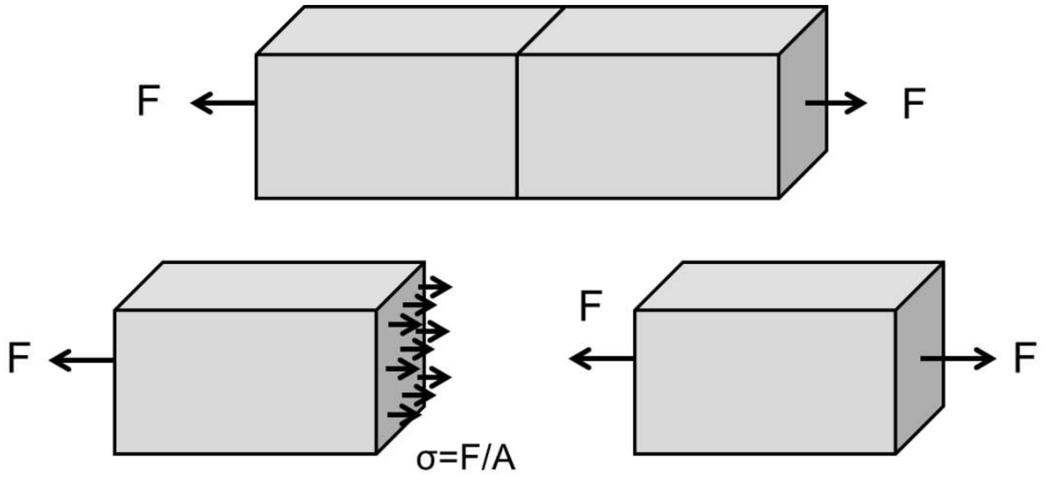

Figure 2.5.: Uniaxal load of a body. The stress is defined as the force divided by the area.

According to the chosen imaginary plane, the force applied on it will be such as to satisfy the force equilibrium condition of the solid. Therefore a proper description of the stress at a point of a body cannot be accomplished by a single vector and the information about the chosen plane should be included. Augustin-Louis Cauchy realized that the force has a linear relationship with the surface normal [39][40]. He described this relationship as tensor which is independent of the chosen surface and describes only the stress state at a specific point in a body, as defined in

$$\begin{bmatrix} T_1 \\ T_2 \\ T_3 \end{bmatrix} = \begin{bmatrix} \sigma_{xx} & \sigma_{xy} & \sigma_{xz} \\ \sigma_{yx} & \sigma_{yy} & \sigma_{yz} \\ \sigma_{zx} & \sigma_{zy} & \sigma_{zz} \end{bmatrix} \begin{bmatrix} n_1 \\ n_2 \\ n_3 \end{bmatrix} , \tag{2.12}$$

where $\boldsymbol{T}$ is the force vector on the surface with normal $\boldsymbol{n}$ and σ is the stress tensor suggested by Cauchy. Additionally, Cauchy has shown that the stress tensor at a point P is formed by the stress vectors of 3 mutually perpendicular planes which pass through P [41]. The stress vector in any other plane passing through P can be obtained by a coordinate transformation of the stress tensor. Fig. 2.7 depicts Cauchy stress definition in a cube.

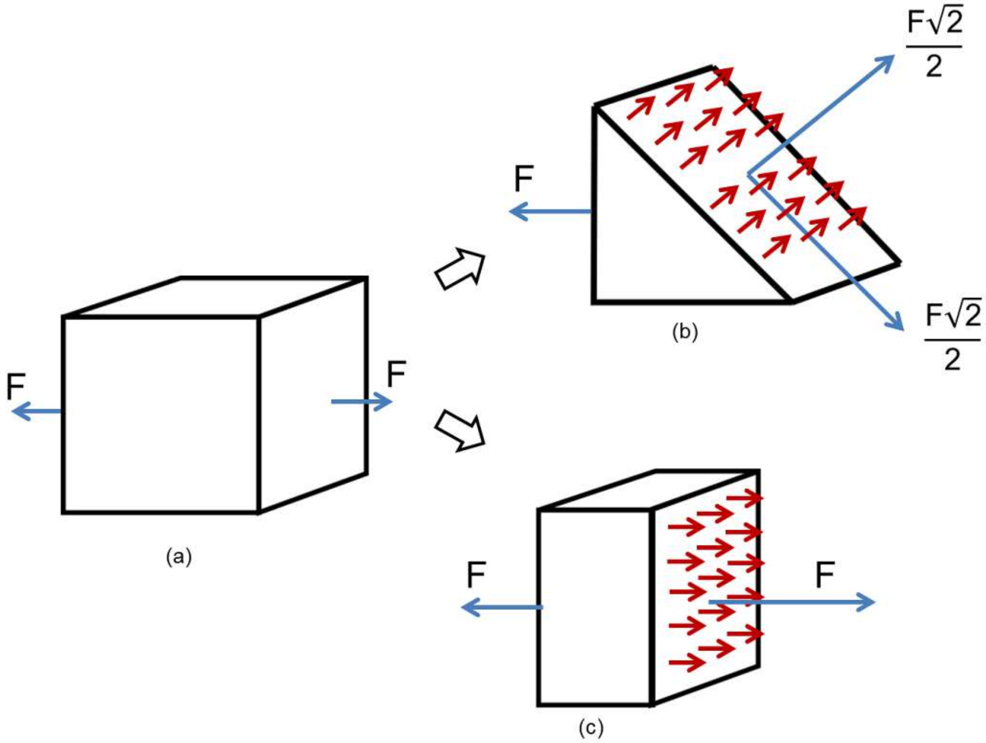

Figure 2.6.: The dependence of stress on the chosen plane. A body under a load (a) can have different stress configurations at a point, depending on the considered plane (b and c). However, they must describe the same physical phenomenon.

Like the strain nomenclature, the stress components have special names according to their direction. The components aligned to the normal of the three perpendicular planes are called normal stress and those perpendicular to the normal of the plane are the shear stress. The Cartesian coordinate system is suitable for the application of Cauchy's definition. The sub-indexes used in (2.12) refer to the Cartesian coordinate system (But any other coordinate system can be used without (2.12) losing its generality).

An important stress tensor's property is symmetry. The stress must hold this property, in order to satisfy conservation of angular momentum. Since the stress tensor is a second-order object (matrix), the symmetry eases the mathematical handling of the tensor. It is possible to prove that a symmetric matrix has real eigenvalues and perpendicular eigenvectors [42]. Hence, the eigenvectors can define a space to apply the Cauchy stress definition. Furthermore, in this space the stress tensor is a diagonal matrix of the eigenvalues. This means that, in the "eigenspace" the stress tensor has no shear stress, it has only normal stress. These components (eigenvalues) are called principal stresses and the eigenvectors are known as the principal stress directions.

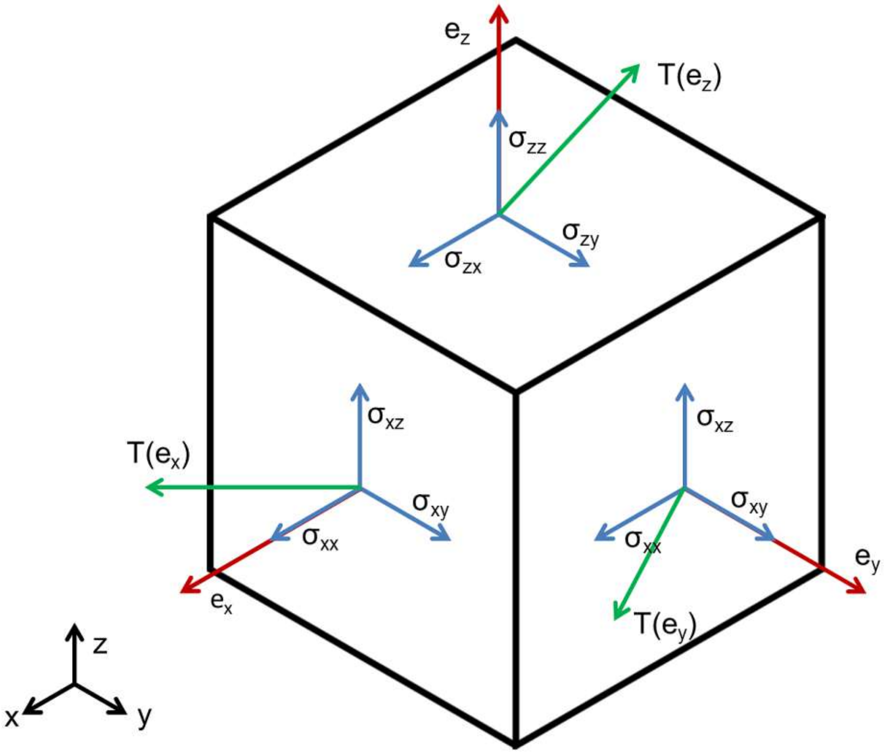

Figure 2.7.: Stress definition in a cube.

2.2.2. Hooke's Law

The elastic behavior of solids can be modeled by the same principle which governs spring deformations, known as Hooke's law. The law suggests a linear relationship between the deformation and the force applied to a string or in a solid. Hence, the relation stress-strain in solid bodies in the elastic regime can be expressed by

$$\bar{\bar{\sigma}} = \boldsymbol{C}\bar{\bar{\epsilon}} \; , \tag{2.13}$$

where $\boldsymbol{C}$ is a linear mapping between the two tensors $\bar{\bar{\sigma}}$ and $\bar{\bar{\epsilon}}$. This implies that $\boldsymbol{C}$ is a fourth-order tensor with 81 components (each of the 9 strain tensor components is related with each of the 9 stress tensor components). However, due to the symmetry of the strain and stress tensors the number of independent components of $\boldsymbol{C}$ can be reduced to 21. This simplification process can be seen graphically in Fig. 2.8. Therefore a 6x6 symmetric matrix is a convenient way for representing the tensor $\boldsymbol{C}$ and the stress-strain relation can be rewritten as in

$$\begin{bmatrix} \varepsilon_{xx} \\ \varepsilon_{yy} \\ \varepsilon_{zz} \\ \gamma_{xy} \\ \gamma_{xz} \\ \gamma_{yz} \end{bmatrix} = \begin{bmatrix} C_1 & C_2 & C_3 & 0 & 0 & 0 \\ C_4 & C_5 & C_6 & 0 & 0 & 0 \\ C_7 & C_8 & C_9 & 0 & 0 & 0 \\ 0 & 0 & 0 & C_{10} & 0 & 0 \\ 0 & 0 & 0 & 0 & C_{11} & 0 \\ 0 & 0 & 0 & 0 & 0 & C_{12} \end{bmatrix} \begin{bmatrix} \sigma_{xx} \\ \sigma_{yy} \\ \sigma_{zz} \\ \sigma_{xy} \\ \sigma_{xz} \\ \sigma_{yz} \end{bmatrix}, \tag{2.14}$$

where C_i are constants to be determined in the next sections. The matrix in (2.14) is also known as stiffness matrix.

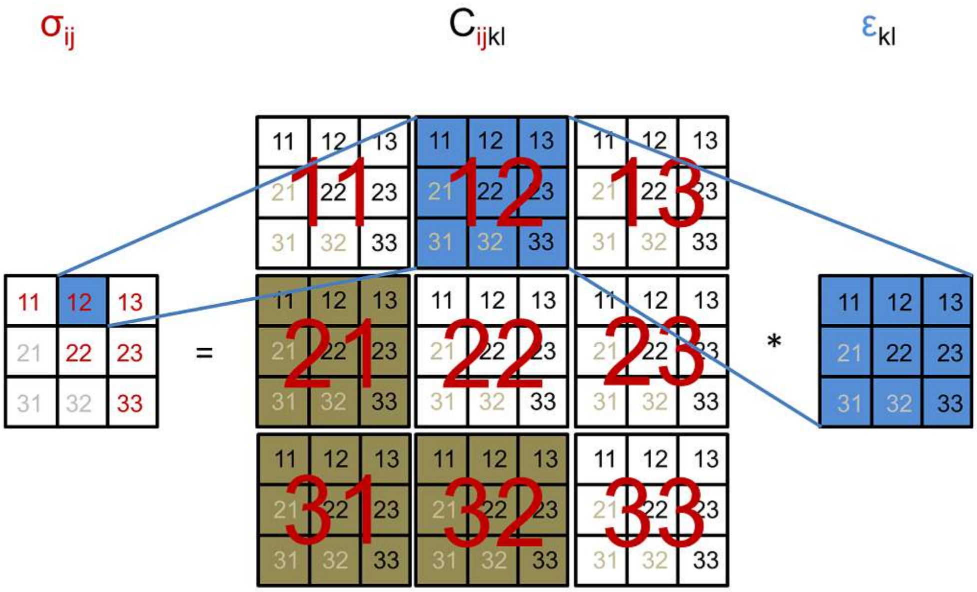

Figure 2.8.: Visualization of the tensorial Hooke's law. Strain symmetry forces symmetry on the $\boldsymbol{C}$ tensor on all components in the form C_{ij21}, C_{ij31}, and C_{ij32} indicated by numbers in gray. Strain symmetry is enforced on the components C_{21kl}, C_{31kl}, and C_{32kl} indicated by the brown squares.

Coefficient Determination for the Normal Components

The coefficients of the stiffness matrix for the normal components can be obtained from the superposition of two effects in a solid. For doing so, a force which is applied to a body is considered, as depicted in Fig. 2.9.

The body stretches in the same direction of the load and shrinks in the perpendicular direction. These two deformations can be treated separately and then added together by the principle of linear superposition of the resulting strains produced by each phenomena depicted in Fig. 2.9. The strain in the parallel direction is given by

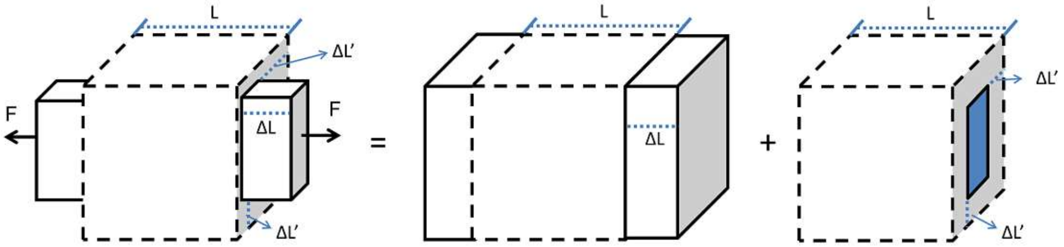

Figure 2.9.: Superposition of effects during an uniaxial loading of a body, where $\Delta L/L$ is the normal strain $\epsilon_{parallel}$ along the direction of the applied force and $\Delta L'/L$ is the normal strain ϵ_{perp} in the directions perpendicular to the force.

the uniaxial (1D) Hooke's Law. Consequently, the linear mapping between the stress and strain is described by a constant

$$\sigma = E\epsilon_{parallel} \ , \tag{2.15}$$

where, $\epsilon_{parallel}$ is the strain in the direction to the parallel to the applied force. It should be noted that in the one-dimensional case the stress and the strain are no longer a tensor but a scalar. The proportionality constant E is known as Young modulus (or elastic modulus). The Young's modulus depends on the material of the solid and characterizes the material stiffness. Materials with high values of E are stiffer and harder to deform. Typical values of Young's modulus for different materials essential in semiconductor industry are listed in Table 2.1.

Table 2.1.: Mechanical properties of common materials used in semiconductor device manufacturing.

Material	Young Modulus (GPa)	Poisson ration	CTE (K/10^{-6})	Reference
W	410	0.30	4	[39][43]
Cu	124	0.34	16	[39][44]
Al	69-79	0.35	22	[39]
Si	107	0.22	5	[39]
SiO2	94	0.16	0.5	[39]
Ti	116	0.30	9	[39]
TiN	440-640	0.25-0.29	9.4	[45][46][47]
Ta	185	0.35	6.5	[48][49][50]
SiN	270-320	0.22	3	[39]

The strain in the perpendicular direction is also defined by the uniaxial Hooke's Law but with a different proportionality constant as in

$$\sigma = \frac{E}{\nu}\epsilon_{perp} \; , \tag{2.16}$$

where ν is known as the Poisson ratio and ϵ_{perp} is the strain in a direction perpendicular to the applied force. The Poisson ration describes the deformation in the perpendicular direction as a proportion of the deformation in the parallel direction. Typical values of the Poisson ratio for semiconductor materials are also given in Table 2.1.

For a general treatment, forces applied in all three coordinate directions should be considered. A complete description for a 3D system is given by the set of equations

$$\begin{array}{lll} \epsilon^1_{xx} = \frac{1}{E}\sigma_{xx} & \epsilon^1_{yy} = -\frac{\nu}{E}\sigma_{xx} & \epsilon^1_{zz} = -\frac{\nu}{E}\sigma_{xx} \\ \epsilon^2_{xx} = \frac{\nu}{E}\sigma_{yy} & \epsilon^2_{yy} = -\frac{1}{E}\sigma_{yy} & \epsilon^2_{zz} = -\frac{\nu}{E}\sigma_{yy} \\ \epsilon^3_{xx} = \frac{\nu}{E}\sigma_{zz} & \epsilon^3_{yy} = -\frac{\nu}{E}\sigma_{zz} & \epsilon^3_{zz} = -\frac{1}{E}\sigma_{zz} \end{array} \; , \tag{2.17}$$

where the indexes xx, yy, and zz stand for the normal strains and stresses. The super-indexes 1, 2, and 3 refer to the deformations induced by forces in the x, y, and z directions, respectively.

Finally, all the strains in each direction can be superimposed ($\epsilon_{ii} = \epsilon^1_{ii} + \epsilon^2_{ii} + \epsilon^3_{ii}$) and with some algebraic manipulation the final total strain in each direction is given by

$$\begin{array}{l} \epsilon_{xx} = \frac{(1+\nu)}{E}\sigma_{xx} - \frac{\nu}{E}(\sigma_{xx} + \sigma_{yy} + \sigma_{zz}) \\ \epsilon_{yy} = \frac{(1+\nu)}{E}\sigma_{yy} - \frac{\nu}{E}(\sigma_{xx} + \sigma_{yy} + \sigma_{zz}) \\ \epsilon_{zz} = \frac{(1+\nu)}{E}\sigma_{zz} - \frac{\nu}{E}(\sigma_{xx} + \sigma_{yy} + \sigma_{zz}) \end{array} \; . \tag{2.18}$$

Coefficient Determination for the Shear Components

Regarding the shear components, the coefficient determination follows directly from the uniaxial Hooke's Law. Similarly to the previous case, the shear stress relates to the strain by a coefficient as in

$$\tau = \frac{G}{\gamma} \; , \tag{2.19}$$

where τ and γ are the shear stress and strain. G is the shear modulus and defines the resistance of a body to torsion. The shear modulus can be written in terms of the Young modulus and the Poisson ratio according to

$$G = \frac{E}{2(1+\nu)} \,. \tag{2.20}$$

In conclusion, Hooke's law with all constants is given by

$$\begin{bmatrix} \varepsilon_{xx} \\ \varepsilon_{yy} \\ \varepsilon_{zz} \\ 2\varepsilon_{xy} \\ 2\varepsilon_{xz} \\ 2\varepsilon_{yz} \end{bmatrix} = \begin{bmatrix} \varepsilon_{xx} \\ \varepsilon_{yy} \\ \varepsilon_{zz} \\ \gamma_{xy} \\ \gamma_{xz} \\ \gamma_{yz} \end{bmatrix} = \frac{1}{E} \begin{bmatrix} 1 & -\nu & -\nu & 0 & 0 & 0 \\ -\nu & 1 & -\nu & 0 & 0 & 0 \\ -\nu & -\nu & 1 & 0 & 0 & 0 \\ 0 & 0 & 0 & (1+\nu) & 0 & 0 \\ 0 & 0 & 0 & 0 & (1+\nu) & 0 \\ 0 & 0 & 0 & 0 & 0 & (1+\nu) \end{bmatrix} \begin{bmatrix} \sigma_{xx} \\ \sigma_{yy} \\ \sigma_{zz} \\ \sigma_{xy} \\ \sigma_{xz} \\ \sigma_{yz} \end{bmatrix} \,. \tag{2.21}$$

The inverse relation with the stress on the left side is written as

$$\begin{bmatrix} \sigma_{xx} \\ \sigma_{yy} \\ \sigma_{zz} \\ \sigma_{xy} \\ \sigma_{xz} \\ \sigma_{yz} \end{bmatrix} = \begin{bmatrix} 1-\nu & \nu & \nu & 0 & 0 & 0 \\ \nu & 1-\nu & \nu & 0 & 0 & 0 \\ \nu & \nu & 1-\nu & 0 & 0 & 0 \\ 0 & 0 & 0 & \frac{(1-2\nu)}{2} & 0 & 0 \\ 0 & 0 & 0 & 0 & \frac{(1-2\nu)}{2} & 0 \\ 0 & 0 & 0 & 0 & 0 & \frac{(1-2\nu)}{2} \end{bmatrix} \begin{bmatrix} \varepsilon_{xx} \\ \varepsilon_{yy} \\ \varepsilon_{zz} \\ 2\varepsilon_{xy} \\ 2\varepsilon_{xz} \\ 2\varepsilon_{yz} \end{bmatrix} \,. \tag{2.22}$$

2.2.3. Thermal Expansion

So far the discussion has treated indistinguishably the source of stress. However, for thermal sources a special treatment is suitable, due to its importance in engineering problems. Temperature variation in a solid leads to its expansion or retraction, and consequently to deformations. Thus, thermal strains can be described by

$$\varepsilon_{th} = \alpha \Delta T \,, \tag{2.23}$$

where ε_{th} is the thermal strain, ΔT is the temperature variation and α is the coefficient of thermal expansion (CTE). Typical values of CTE for materials in semiconductor industry are listed in Table 2.1.

Thermal expansion is an isotropic effect, which means that the material expands according to (2.23) in every direction. Additionally, there is no skew deformations induced by thermal variations, meaning only normal components of the strain tensor are affected. Hooke's law, with thermal effects included is given by

$$\begin{bmatrix}\varepsilon_{xx}\\ \varepsilon_{yy}\\ \varepsilon_{zz}\\ \gamma_{xy}\\ \gamma_{xz}\\ \gamma_{yz}\end{bmatrix} = \frac{1}{E}\begin{bmatrix}1 & -\nu & -\nu & 0 & 0 & 0\\ -\nu & 1 & -\nu & 0 & 0 & 0\\ -\nu & -\nu & 1 & 0 & 0 & 0\\ 0 & 0 & 0 & (1+\nu) & 0 & 0\\ 0 & 0 & 0 & 0 & (1+\nu) & 0\\ 0 & 0 & 0 & 0 & 0 & (1+\nu)\end{bmatrix}\begin{bmatrix}\sigma_{xx}\\ \sigma_{yy}\\ \sigma_{zz}\\ \sigma_{xy}\\ \sigma_{xz}\\ \sigma_{yz}\end{bmatrix} + \alpha\Delta T\begin{bmatrix}1\\1\\1\\0\\0\\0\end{bmatrix}, \quad (2.24)$$

which can be represented inversely with

$$\begin{bmatrix}\sigma_{xx}\\ \sigma_{yy}\\ \sigma_{zz}\\ \sigma_{xy}\\ \sigma_{xz}\\ \sigma_{yz}\end{bmatrix} = \bar{\bar{K}}\begin{bmatrix}\varepsilon_{xx}\\ \varepsilon_{yy}\\ \varepsilon_{zz}\\ 2\varepsilon_{xy}\\ 2\varepsilon_{xz}\\ 2\varepsilon_{yz}\end{bmatrix} - \frac{E\alpha\Delta T}{1-2\nu}\begin{bmatrix}1\\1\\1\\0\\0\\0\end{bmatrix}, \quad (2.25)$$

where

$$\bar{\bar{K}} = \begin{bmatrix}1-\nu & \nu & \nu & 0 & 0 & 0\\ \nu & 1-\nu & \nu & 0 & 0 & 0\\ \nu & \nu & 1-\nu & 0 & 0 & 0\\ 0 & 0 & 0 & \frac{(1-2\nu)}{2} & 0 & 0\\ 0 & 0 & 0 & 0 & \frac{(1-2\nu)}{2} & 0\\ 0 & 0 & 0 & 0 & 0 & \frac{(1-2\nu)}{2}\end{bmatrix}.$$

To conclude this section, it is worth to make some remarks regarding the presented approach. First, the adopted strain definition is commonly referred as engineering strain, but there are other measures (e.g. True strain [51], Stretch ratio [51], Green strain [40], and Almansi strain [40]) which are particularly useful for describing phenomena outside the infinitesimal strain theory [39][40][41]. Usually, mechanical deformation in semiconductor devices can be properly treated solely by implementing the engineering strain definition, but some scenarios may demand the True strain definition.

Second, Hooke's law was derived assuming that the solid was made of an isotropic material, which assures that the material constants (E, ν, and α) are independent of direction. However, for some materials this condition is not valid as in the case of silicon, where the Young modulus can variate between 130GPa and 189GPa depending on the direction [52].

Lastly, in literature it is possible to find Hooke's law described using other material constants, for example the Lamé parameters [39]. There is a suitable relation between the set of constants and it is a matter of preference or ease of notation for one to use one as opposed to the other.

2.3. Reliability

Reliability concerns the characteristic of a device to remain functional during a period of time under established environmental conditions. Ultimately, every device will eventually fail. The task of the reliability study is to provide technology to keep a device economically viable despite failure. Reliability of semiconductors has its own particularities, which were summarized in a 2010 report from the Reneseas Electronics Corporation of 2010 [53] as:

1. *Semiconductor devices have a configuration, which is fundamentally very sensitive to impurities and particles, and the stability status of the surface state is extremely important. Consequently, to manufacture these devices it is necessary to manage many processes while completely controlling the level of impurities and particles. Furthermore, the quality of the finished product depends upon the complex relationship of each interacting substance in the semiconductor, including chip material, metallization and package.*
2. *The problems of thin films and micro-processes must be fully understood as they apply to metallization and bonding. It is also necessary to analyze surface phenomena from the aspect of thin films.*
3. *Due to the rapid advances in technology, many new products are developed using new processes and materials, and there is a high demand for product development in a short time period. Consequently, it is not possible to refer to the reliability achievements of existing devices.*
4. *In greed, semiconductor products are manufactured in high in volume. In addition, repair of finished semiconductor products is impractical. Therefore incorporation of reliability at the design stage and reduction of variation in the production stage have become essential.*
5. *Reliability of semiconductor devices may depend on assembly, use, and environmental conditions. Stress factors effecting device reliability include voltage, current density, temperature, humidity, gas, dust, contamination, mechanical stress, vibration, shock, radiation, and intensity of electrical and magnetic fields.*

Those five points emphasize the importance of a good design and process control to prevent device failure. The mechanisms of failure must be understood during the development stage of the product, otherwise it can be too late to repair it.

A device failure can have different reasons. It can arise from electrical effects (e.g. negative-bias temperature instability), mechanical forces, material degradation, environmental, and even a combination of several effects (e.g. electromigration). The mechanical reliability of semiconductor devices are commonly associated with fracture and fatigue prevention. The main goal of the mechanical study is to identify situations, where a device structure could be damaged beyond repair. Therefore, in addition to the stress-strain theory established in the last section, a method is needed to determine when a deformation ceases to be elastic and becomes plastic and permanent.

2.3.1. Yield

Yield is the name given to the point in the stress-strain curve where the material's response to an applied force switches from an elastic to an inelastic behavior [39]. A body unloaded under a plastic regime keeps some strain (permanent deformations). Thus, a future loading starts with an offset and the elastic regime is retained until the prior unload point is reached, as sketched in Fig. 2.10. This means that the yield point shifts accordingly to the load history of the material. Moreover, the yield strength increases and the material becomes less prone to plastic deformations. This phenomenon is known as hardening. It is behind the manufacturing of several engineering products, such as the creation of blades. When a smith hits the metal, hardening takes place and it becomes tougher to deform the metal permanently in any subsequent load, especially during the use of the blade.

2.3.2. Yield Criteria

Although hardening modifies the position of the yield point, it is possible to treat both effects separately. The yield point is considered fixed at its first position and the hardening effects are added incrementally whenever needed.

In the literature are a variety of criteria to establish material yielding [39][40][41]. The main challenge is to derive, from the stress tensor, a criterion which triggers yield for different types of materials. For example, in brittle materials it is considered a good criterion that yielding occurs – in fact, brittle materials fracture rather than yield – whenever the largest principal stress surpasses an experimentally established threshold [54]. However, for ductile materials functions of the maximum shear stress is a more suited criterion. Furthermore, anisotropic materials need a different treatment altogether, which considers the directional dependence of the material properties.

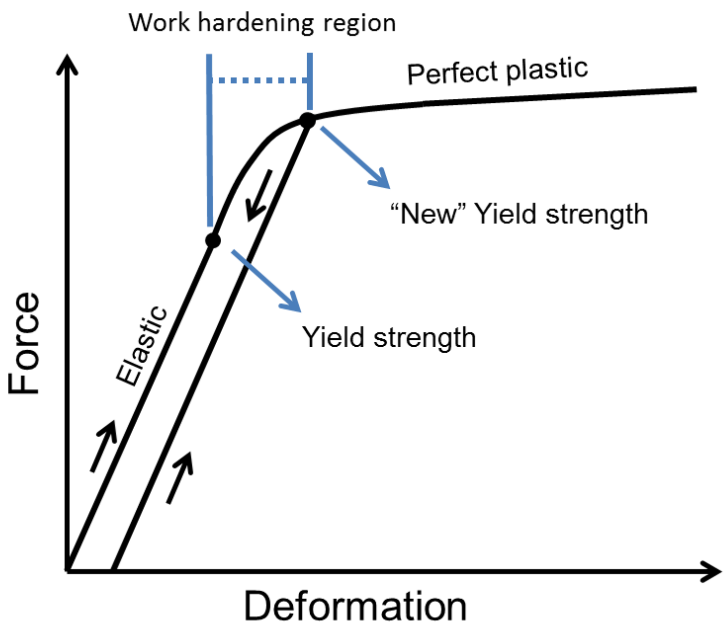

Figure 2.10.: Material plasticity in the stress-strain curve. Unloads in the work hardening region retain the deformation history and any subsequent load will relate linearly with the strain until the original unload point is reached ("New" Yield strength). Beyond the work hardening region the material enters a perfect plastic regime, where increases to the yield strength can be considered (most of the time) negligible.

Usually, materials used in the semiconductor industry are ductile. For these types of materials there are two most often implemented theories: Tresca theory (or the Maximum Shear Stress) and von Mises theory (or Distortion Energy theory).

Tresca Theory

The study of yielding was, since the very beginning, motivated by the wish to predict mechanical failure of materials. Yielding is considered as the beginning of a process which will eventually lead to fracture, characterized by the breaking of the bonds between atoms and separation of the material. It is possible to show that the stress required to break the atom bonds is roughly one third of the material's Young's modulus [54]. However, ductile materials fail with stress values far smaller than this estimate. For example, aluminium has a theoretical strength of 22GPa, but the stress required for material failure is approximately 100MPa [54]. This inconsistency is justified by the split mechanism of ductile materials. Instead of the rupture of atomic bonds, the material is separated by sliding of atoms as shown in Fig. 2.11.

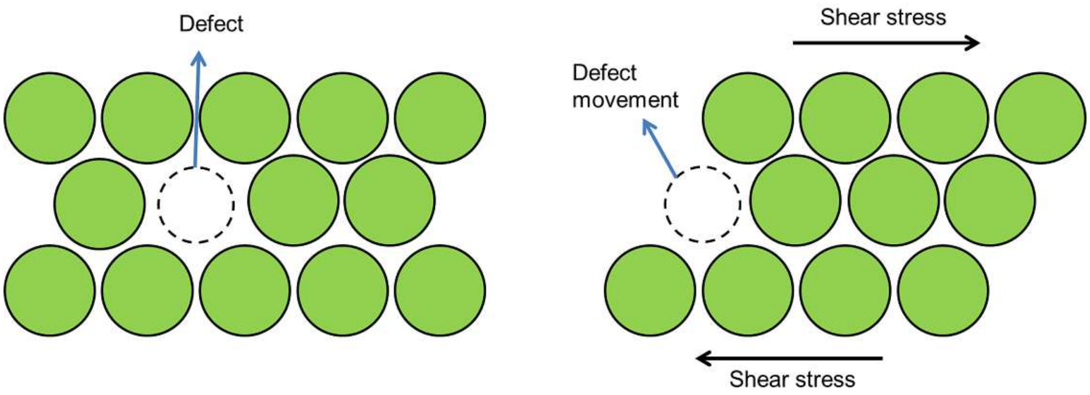

Figure 2.11.: Defect movement triggered by shear stress.

This phenomenon is related to defects and the way they move inside the materials. Chapter 5 discusses this phenomenon in greater detail. In conclusion, failure in ductile materials is caused by shear deformations. Hence, it is logical to establish a yield criterion in terms of the amount of shear stress a material is able to sustain. This is the principle of the Tresca theory which can be quantified by

$$\frac{1}{2}\max(|\sigma_1 - \sigma_2|, |\sigma_2 - \sigma_3|, |\sigma_3 - \sigma_1|) > \tau_{max} \ , \tag{2.26}$$

where σ_1, σ_2, and σ_3 are the principal stresses and τ_{max} is the maximum shear strain a material can sustain until it starts to yield (usually obtained experimentally). It is convenient to to define yield criteria by the principal components, since they are invariant to any coordinate system.

Von Mises Theory

Like the Tresca criterion, the von Mises criterion also considers shear deformations as the main mechanism to trigger yielding. However, instead of using the maximum shear stress as the limit of elasticity, the strain energy of shear deformations (distortion energy) is used [55]. In principle there is a critical distortion energy which, if surpassed, pushes the material into the plastic regime. The total strain energy per unit of volume of a body can be calculated in terms of the principal stresses by

$$\begin{aligned} U_T &= \tfrac{1}{2}\sigma_1\epsilon_1 + \tfrac{1}{2}\sigma_2\epsilon_2 + \tfrac{1}{2}\sigma_3\epsilon_3 \\ &= \tfrac{1}{2E}\left[\sigma_1^2 + \sigma_2^2 + \sigma_3^2 - 2\nu\left(\sigma_1\sigma_2 + \sigma_1\sigma_3 + \sigma_2\sigma_3\right)\right] \ , \end{aligned} \tag{2.27}$$

where ϵ_1, ϵ_2 and ϵ_3 are the principal strains. The relation (2.27) accounts for every deformation in the body, while for yielding only shear deformations are relevant.

Therefore, the energy stored by normal deformations (hydrostatic energy) must be subtracted from (2.27) in order to obtain the distortion energy. The hydrostatic energy is given by

$$U_H = \tfrac{1-2\nu}{6E}\left(\sigma_1^2 + \sigma_2^2 + \sigma_3^2 + (\sigma_1\sigma_2 + \sigma_1\sigma_3 + \sigma_2\sigma_3)\right) \ . \tag{2.28}$$

Consequently, the distortion energy is given by

$$\begin{aligned} U_D &= U_T - U_H \\ &= \tfrac{(1+\nu)}{6E}\left[(\sigma_1-\sigma_2)^2 + (\sigma_1-\sigma_3)^2 + (\sigma_2-\sigma_3)^2\right] \ . \end{aligned} \tag{2.29}$$

Yielding occurs whenever U_D exceeds a critical energy (U_{Dmax}) [54]. The experimental determination of U_{Dmax} is challenging and it is more convenient to use a critical stress value. Nonetheless, an uniaxial determination of the critical stress is straightforward to obtain experimentally and the von Mises criterion remains valid in any situation. Moreover U_{Dmax} is a material property and must be independent of the load configuration. Hence, for a body under an uniaxial load the relation (2.29) can be further simplified for $[(1+\nu)/6E]\sigma_{Max}^2$, where σ_{Max}^2 is the critical stress required to yield the material. The critical stress obtained by the uniaxial stress test can be used in (2.30) to establish a criterion in terms of stress.

$$\begin{aligned} U_D &< U_{Dmax} \\ \tfrac{(1+\nu)}{6E}\left[(\sigma_1-\sigma_2)^2 + (\sigma_1-\sigma_3)^2 + (\sigma_2-\sigma_3)^2\right] &< \tfrac{(1+\nu)}{6E}\sigma_{Max}^2 \\ \left[(\sigma_1-\sigma_2)^2 + (\sigma_1-\sigma_3)^2 + (\sigma_2-\sigma_3)^2\right]^{1/2} &< \sigma_{Max} \qquad , \end{aligned} \tag{2.30}$$

where the left hand side of the inequality is the equivalent stress which leads to yielding, explicitly described by

$$\sigma_{Mises} = \left[(\sigma_1-\sigma_2)^2 + (\sigma_1-\sigma_3)^2 + (\sigma_2-\sigma_3)^2\right]^{1/2} \ . \tag{2.31}$$

The equivalent stress is also known as von Mises stress.

Tresca Criterion vs. Von Mises Criterion

A comparison between the criteria is a good exercise to obtain a better understanding of both theories. Consider the orthogonal space S defined by the principal stress vectors. A point in S is called stress state. The inequalities (2.26) and (2.30) delineate a region in S, where every stress state internal to the border is in the elastic regime, while the states at the border and external to it refer to the plastic regime, as shown in Fig. 2.12.

The Tresca theory is more conservative than the von Mises theory. It predicts a narrower elastic region. The Tresca criterion can be safer from the design point of view, but it could lead the engineer to take unnecessary measures to prevent an unlikely failure. The criterion choice depends on the type of design and personal taste of the designer.

To conclude this session a final remark regarding plasticity in the dimensions of microelectronic devices is warranted. At this scale, the traditional plasticity theory is often unreliable. Sometimes the materials have a different plastic mechanism, while at other times the material is not thick enough for plasticity to take place. Therefore, the classical approach for plasticity is not considered and the plastic models used in the further sections will be presented together with the situation where the mechanism originates.

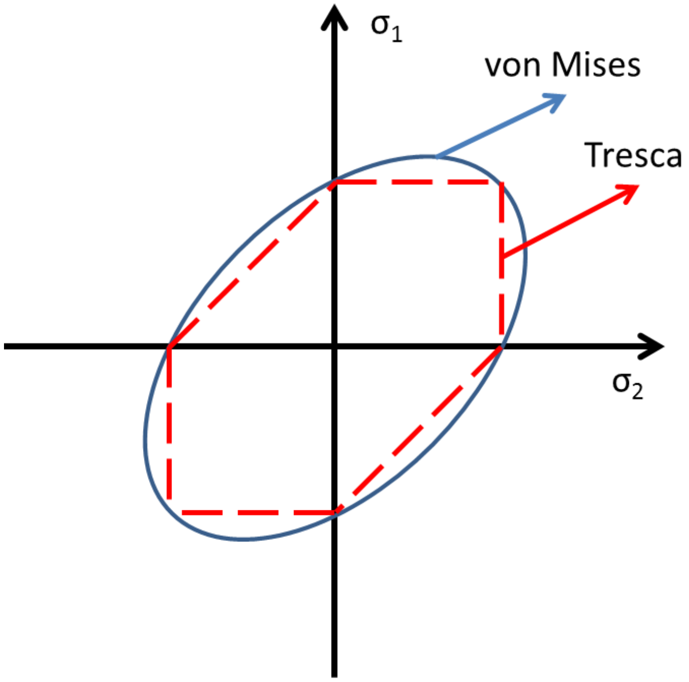

Figure 2.12.: Von Mises versus Tresca criteria in a 2D system.

3. Simulation of Mechanical Systems

An substantial part of modeling and simulation of microelectronic phenomena involves finding a solution to partial differential equations (PDEs). Solving PDEs is an essential step in the simulation of semiconductor processing, device performance, and reliability. A general solution to PDEs is usually unknown and the few known cases are only available for simple problems under very confined conditions. However, engineering problems are diversified and simplified solutions can spoil the analysis. With the advent of the electronic computer, numerical methods with high quality approximations could be applied enabling physical simulations as a helpful tool in engineering analysis and design. In this chapter the Finite Element Method (FEM) is briefly presented as the technique to solve the PDEs. First, the mathematical background of the method is discussed, then its application is analyzed with a general elastic problem. In the last section, numerical schemes for time-dependent problems are treated, closing the set of techniques used within this work.

3.1. Finite Element Method

The Finite Element Method (FEM) is a numerical technique used to approximate solutions of PDEs [56]. The technique has surged in the mids 60s and it was intended for solving problems which emerged from elastic theory and structural analysis, for instance, to calculate stress in dams, buildings, and airplanes [57]. In the beginning, FEM was shaped by structural analysts. Thus, the method presentation and nomenclature was particularly suitable for structural mechanics problems. However, the successful progress of the FEM and the rise of the electronic computing industry in the 70s attracted a lot of interest from the scientific community. In the same decade, several mathematicians worked through the details of the FEM, and they could relate the theory behind it to the works of Galerkin, Ritz, and Rayleigh from the late 19th century [57][58]. This development has led to the generalization of the FEM and enabled its use outside the structural mechanics field.

The main idea behind FEM is to approximate the solution of a PDE by a linear combination of functions. Those functions are defined in discrete portions of the PDE domain, the so called finite elements. In principle, FEM can be applied to solve every kind of PDE, but in practice some types of equations are more numerically challenging than others, and FEM would not be a suitable choice, or a modification on the traditional approach is required. The method presented here will be restricted to elliptic PDEs [56], since solid mechanics problems can be represented by one of those.

3.1.1. Variational Form

As a starting point, consider the boundary value problems (BVP) described by

$$\begin{gathered} -u''(x) = f(x) \\ x \in (0,1); u(0) = u(1) = 0 \ . \end{gathered} \tag{3.1}$$

Additionally, define a linear space V as:

> V = {v: continous functions in [0,1] with v' piecewise continous and bounded in [0,1], and v(0)=v(1)=0}

Along this session, it will be shown how the space V can be used to reformulate the problem (3.1). From this new version, a numerical method will be developed based on the particular definition of V, in order to obtain an approximate solution of (3.1).

To begin, take an element of the space V, multiply by (3.1) and integrate over the entire domain as in

$$\int u''v dx = \int f v dx \ . \tag{3.2}$$

The function v is known as a test function. Initially, it is not clear how (3.2) can help to solve (3.1), but it provides a different view of the problem (3.1). Indeed, it is possible to simplify (3.2) by integrating the left hand side by parts, according to

$$-\int u''v dx = -u'(1)v(1) + u'(0)v(0) + \int u'v' dx = \int u'v' dx \ . \tag{3.3}$$

Subsequently, substituting the results from (3.3) in (3.1) the relation holds

$$\int u'v' dx = \int f v dx \qquad \forall v \in V \ . \tag{3.4}$$

(3.4) is known as the variational formulation of the problem (3.1). Variational formulations can be handled by several numerical methods, and it is usually easier to prove the existence of the solution of a variational problem in comparison to a PDE.

Seemingly, the solution of (3.1) solves (3.4), but to be useful, the variational formulation should work in the opposite direction, where the solution of (3.4) solves (3.1). This is true for the form described by (3.4), but usually the methods applied to solve variational problems impose some restriction in the solution, which should also satisfy (3.1).

3.1.2. Galerkin's Method

The Galerkin method was developed by the mathematicians Boris Galerkin and Walther Ritz (separately) to treat variational problems similar to (3.4) [56][57][58]. In fact, Galerkin attempted to solve a restricted version of (3.4) as described by

$$\text{Find } u \in V \text{ such that } \int u'v'dx = \int fvdx \qquad \forall v \in V \ . \tag{3.5}$$

The constraints of the solution u to the same space of the test function (V) is very convenient, as it will be shown in the end of Section 3.1.5, but the central question right now is, if the solution u of (3.5) still satisfies the original PDE, (3.1). In order to prove that it does, a good strategy is to derive (3.1) from (3.5). Hence, let u be the solution of (3.5), then it follows that (3.6) must also be satisfied

$$\int_0^1 u'v'dx - \int_0^1 fvdx = 0 \qquad \forall v \in V \qquad \text{and} \qquad u \in V \ . \tag{3.6}$$

In addition to the restrictions imposed on u, consider that u'' exists and is continuous. Integrating the first term by parts and using the boundary conditions ($\mathrm{v}(0) = \mathrm{v}(1) = 0$) the following relation holds

$$-\int_0^1 (u'' + f)vdx = 0 \qquad \forall v \in V \ . \tag{3.7}$$

Since $u'' + f$ is continuous, (3.7) can only stand, if the following relation is true [56]

$$(u'' + f)(x) = 0, x \in [0,1] \ . \tag{3.8}$$

Consequently, u satisfies the original BVP (3.1). However, it was necessary to assume u as a well behaved function (second differentiable continuous). This restriction should satisfy most physical problems, but attention must be paid for careless application of Galerkin's method.

So far only the equivalence of the solution between Galerkin's problem and (3.1) was discussed, but not the method itself. Galerkin's method is developed upon the discretization of (3.6) based on the discretization of the space V as presented in the next section.

3.1.3. Discretization

The basics of Galerkin's method consist of a clever discretization of the infinite linear space V in the problem (3.5). The purpose of such a process is to create a controlled sub-space inside V, which can be designed to approximate the solution of (3.6) with arbitrary precision.

Consider the finite sub-space V_h of V with dimension N. Consider also the functions $\phi_{j=1\ldots N}$ as an orthogonal basis of V_h. Hence, every function v in V_h can be written as linear combination of the basis as in

$$v = \sum_{j=1}^{N} C_j \phi_j, v \in V_h \subset V \ . \tag{3.9}$$

The discrete formulation of the variational problem (3.5) can be written as

$$\text{Find } u_h \in V_h \text{ such that } \int u_h' v' dx = \int f v dx \qquad \forall v \in V_h \ . \tag{3.10}$$

Actually, the formulation (3.10) can be simplified. It can be proven that if u_h satisfies (3.10) only for the basis function of V_h, it satisfies it for every element in V_h. To show this, replace v in (3.10) by the basis projection (3.9) as in

$$\begin{aligned} \int u_h' v' dx &= \int f v dx \ , \\ \int u_h' (\sum_{j=1}^{N} C_j \phi_j)' dx &= \int f \sum_{j=1}^{N} C_j \phi_j dx \ , \\ \sum_{j=1}^{N} C_j \int u_h' \phi_j' dx &= \sum_{j=1}^{N} C_j \int f \phi_j dx \ . \end{aligned} \tag{3.11}$$

On the assumption $\int u_h' \phi_j' = \int f \phi_j$ for j = 1..N, the equality (3.11) holds and u_h satisfies (3.10) for every element of V_h. Consequently, the simplified version of (3.10) can be summarized by:

$$\text{find } u_h \in V_h \text{ such that } \int u_h' \phi_j' dx = \int f \phi_j dx, j = 1..N \ . \tag{3.12}$$

The formulation (3.12) is well suitable for the construction of a numerical scheme, because it restricts the search for the solution u_h to the computation of a finite number of equations (N). Hence, the problem shifts to a more concrete perspective, and a method is required to compute u_h from those N equations. For that purpose, consider the expansion of u_h in the basis of V_h, in the same way as was done before for v_h (3.9). By substituting v_h appropriately in (3.10) the obtained function is

$$\begin{aligned} \int u_h' \phi_j' dx &= \int f \phi_j dx, j = 1..N \ , \\ \int (\sum_{i=1}^{N} C_i \phi_i)' \phi_j' dx &= \int f \phi_j dx, j = 1..N \ , \\ \sum_{i=1}^{N} C_i \int \phi_i' \phi_j' dx &= \int f \phi_j dx, j = 1..N \ . \end{aligned} \tag{3.13}$$

In fact, the substitution of u_h expansion in (3.12) leads to the transformation of the discrete problem in a linear system $Ax = b$ with N equations, where A, x and b are given by

$$A = \begin{bmatrix} \int \phi_1 \phi_1 dx & \cdots & \int \phi_1 \phi_N dx \\ \vdots & \ddots & \vdots \\ \int \phi_N \phi_1 dx & \cdots & \int \phi_N \phi_N dx \end{bmatrix}, \ x = \begin{bmatrix} C_1 \\ \vdots \\ C_N \end{bmatrix}, \ b = \begin{bmatrix} \int f \phi_1 dx \\ \vdots \\ \int f \phi_N dx \end{bmatrix} \ . \tag{3.14}$$

3.1.4. Basis Functions and Domain Partitioning

In principle, there are no restrictions to choose the basis functions of the space V_h. Nevertheless, the complexity of the linear system (3.14) is defined by them. The quality of the approximated solution u_h is expected to increase with the increased dimension of V_h [59]. Thus, good approximations lead to big matrices (A) and consequently to the increase in the computational costs of solving (3.14). From a pragmatic point of view, a sparse matrix A would diminish the computational burden of a high-dimensional V_h space. An ingenious choice of basis function should create sparse matrices while keeping the requirements for a good approximation.

Polynomial piecewise functions are the most traditional choice for basis functions in FEM [56][57]. They are defined in a particular way such that the domain needs to be partitioned as in Fig. 3.3. Each partition is known as a finite element (the origin of the method name). In each element, a set of basis function is defined according to the following criteria [57]:

- It assumes a non-zero value at a node i. In all other nodes the function is zero. Therefore, one function per node.
- It vanishes over all the elements which contain the node i, following the established polynomial rule.
- It must be an element of V_h, therefore it must be continuous and must have the first derivative be piecewise continuous.

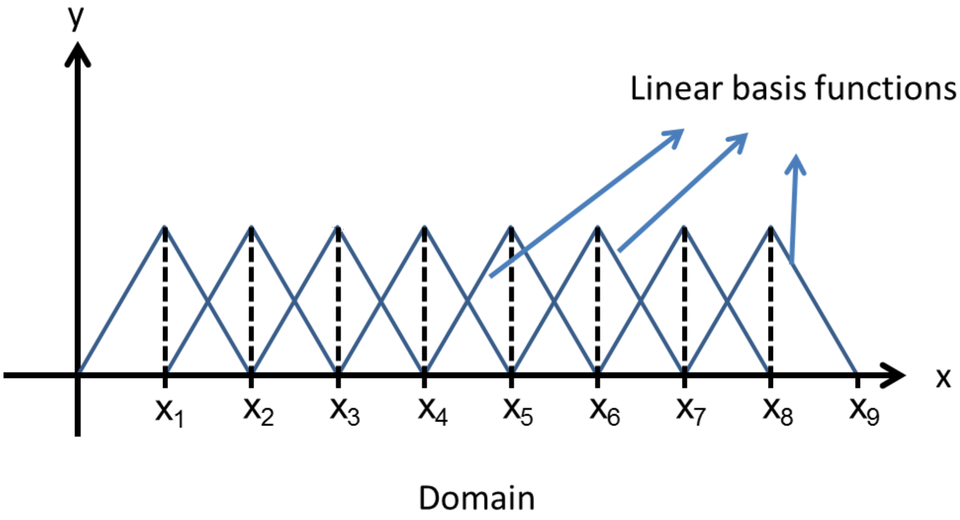

Figure 3.1.: A set of linear basis functions of V_h. As the number of partitions increases, the amount of functions which are possible to represent the solution (V_h dimension) also increases. As consequence, the quality of the approximation is enhanced.

This guidance enables the creation of sparse matrices and simplifies the post-processing of the solution. In Fig. 3.2 a linear piecewise basis function is depicted, which was constructed following the aforementioned criteria.

The construction of basis functions has been a process developed and refined along the years to minimize the computational costs of FEM [57]. It is clear from the criteria that the pattern of the basis function will repeat along the elements. The polynomial in Fig. 3.3 can be generated by linear basis functions as in Fig. 3.2.

Usually, nodes are defined by the boundaries of the element, but some basis functions may require additional nodes. Those points do not define the boundaries, instead they are used as control points. Higher degree polynomials basis functions are created in this fashion, while they also must follow the criteria. In Fig. 3.4, basis functions with quadratic and cubic polynomials are exemplified.

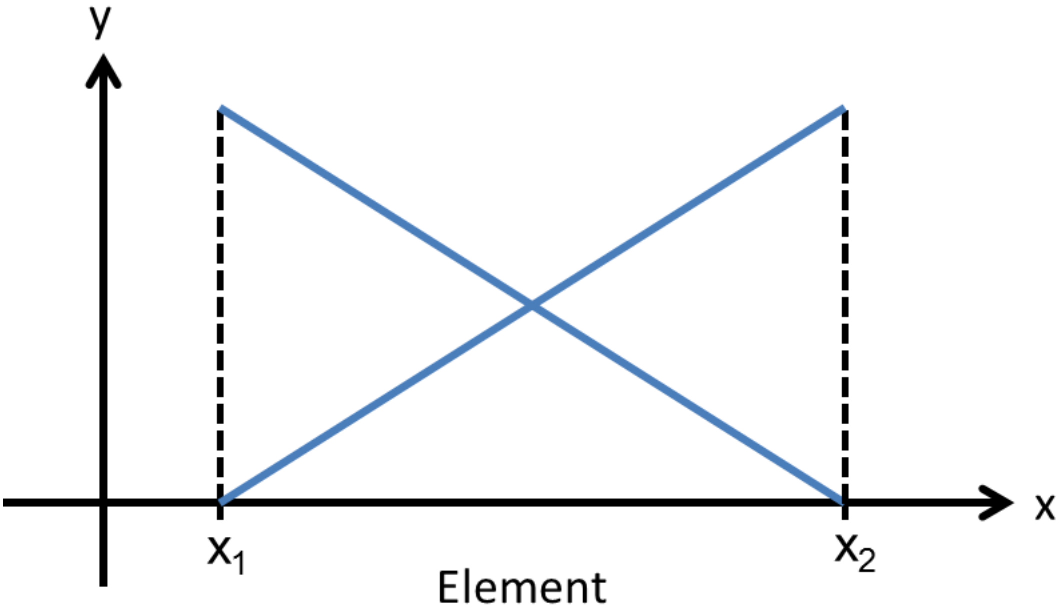

Figure 3.2.: Linear basis function constructed according to the presented criteria.

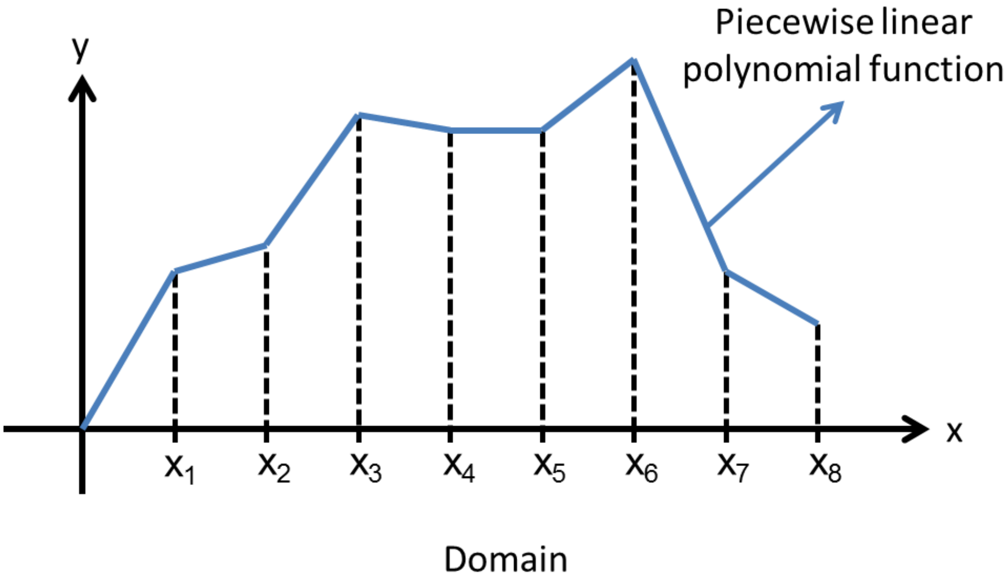

Figure 3.3.: An example of a piecewise linear polynomial function. For each partition a linear function is defined.

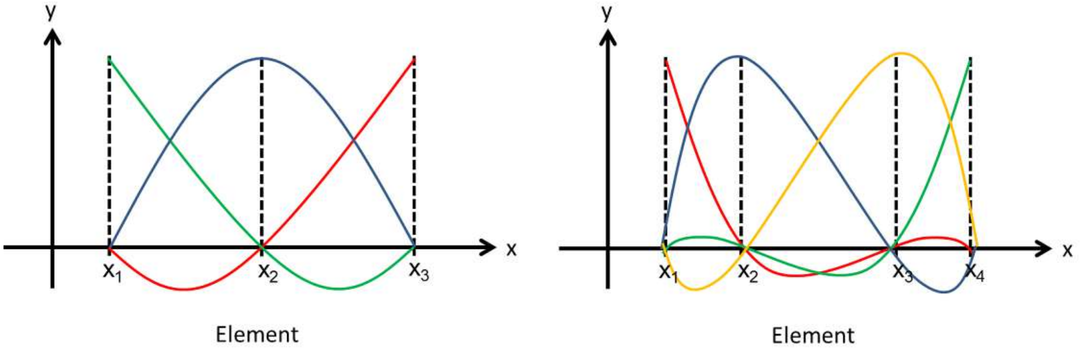

Figure 3.4.: Quadratic (left) and cubic (right) basis function.

As sample application, consider the partition of the BVP problem (3.1) discussed so far. Let linear piecewise polynomials be the basis functions as in Fig. 3.1. Analytically, the linear piecewise basis function can be defined by

$$\phi_j = \begin{cases} 1/h_j & [x_{j-1}, x_j] \\ -1/h_{j+1} & [x_j, x_{j+1}] \\ 0 & (x < x_{j-1}) \cup (x > x_{j+1}) \end{cases} , \tag{3.15}$$

where h_j is the size of the element as described in Fig. 3.2. As seen before, the discrete variational formulation of the BVP problem leads to the linear system (3.14). In order to solve the system, a computation of $\int \phi_i' \phi_j' dx$ is required. For the basis functions employed here this task is straightforward. If $|i-j| > 1$ then $\int \phi_i' \phi_j' dx = 0$, since whenever $|i-j| > 1$ or $\phi_x(x)$ or $\phi_j(x)$ the solution is zero. In the cases of $|i-j| < 1$ the integration result for $i = j$ is given by

$$\int \phi_j \phi_j dx = \int_{x_{j-1}}^{x_j} 1/h_j^2 dx + \int_{x_j}^{x_j+1} 1/h_{j+1}^2 dx = 1/h_j + 1/h_{j+1} , \tag{3.16}$$

while the result for $i = j-1$ and $i = j+1$ is given by

$$\int \phi_j \phi_j + 1dx = \int \phi_j \phi_j - 1dx = -\int_{x_{j-1}}^{x_j} 1/h_j^2 dx = -1/h_j . \tag{3.17}$$

Assuming a homogeneous partition of the domain ($1/h_j = 1/h_{j-1}$) (3.14) can be rewritten as

$$\begin{bmatrix} 2 & -1 & 0 & \cdots & \cdots & 0 \\ -1 & 2 & -1 & 0 & \cdots & 0 \\ 0 & \ddots & \ddots & \ddots & \ddots & \vdots \\ \vdots & \ddots & \ddots & \ddots & \ddots & \vdots \\ \vdots & \ddots & \ddots & \ddots & \ddots & -1 \\ 0 & \cdots & \cdots & 0 & -1 & 2 \end{bmatrix} \begin{bmatrix} C_1 \\ \vdots \\ \vdots \\ \vdots \\ \vdots \\ C_N \end{bmatrix} = \begin{bmatrix} \int f\phi_1 dx \\ \vdots \\ \vdots \\ \vdots \\ \vdots \\ \int f\phi_N dx \end{bmatrix} . \tag{3.18}$$

The linear system (3.18) is the final discretized form of the original BVP problem (3.1). The matrix is sparse due to the choice of the basis functions, and it is also symmetric, which is a great advantage for computing the solution of the system. Symmetry is a desirable property which is very dependent on the problem, but the right choice of the basis functions can ensure it for the linear system.

The development made so far is only suitable for differential equations in the same form as described in (3.1), including the boundary conditions. The problem (3.1) is rather common in nature. Heat transfer, elasticity, and electrostatics are examples of phenomena described by it. The choice here was motivated by the use of (3.1) for different fields and the importance to the models used in this work. Naturally, another differential equation will lead to another variational form. However, the idea remains the same: to multiply it by a function of the space V, to integrate it over the domain, to discretize it by V_h, to partition the domain, to choose the basis functions, and finally to solve the system, summarizing the steps for finding a solution using the Finite Element Method.

Considerations for 2D and 3D Cases

For 2D and 3D problems the procedure is the same, while the mathematical semantics and operations (derivatives and integrations) must be adapted for the proper dimension. The main difference lies in the partitioning of the domain, which can be split in different ways. The creation procedure of a partition is called meshing and the resultant domain division is a mesh. There are several algorithms available for meshing, however, the vast majority of them creates triangular or quadrilateral meshes for 2D domains and tetrahedral and quadrilaterally-faced hexahedral meshes for 3D domains [60].

Regarding the basis functions, the concept for creation persists. The criteria for construction should still be satisfied and they should be polynomials, but for this case in 2D and 3D dimensions. The basis functions construction for 2D and 3D domains is rather lengthy and cumbersome, however, well treated in a variety of textbooks [56][57]. Examples of basis functions for 2D domains with quadratic meshes are detailed in Fig. 3.5.

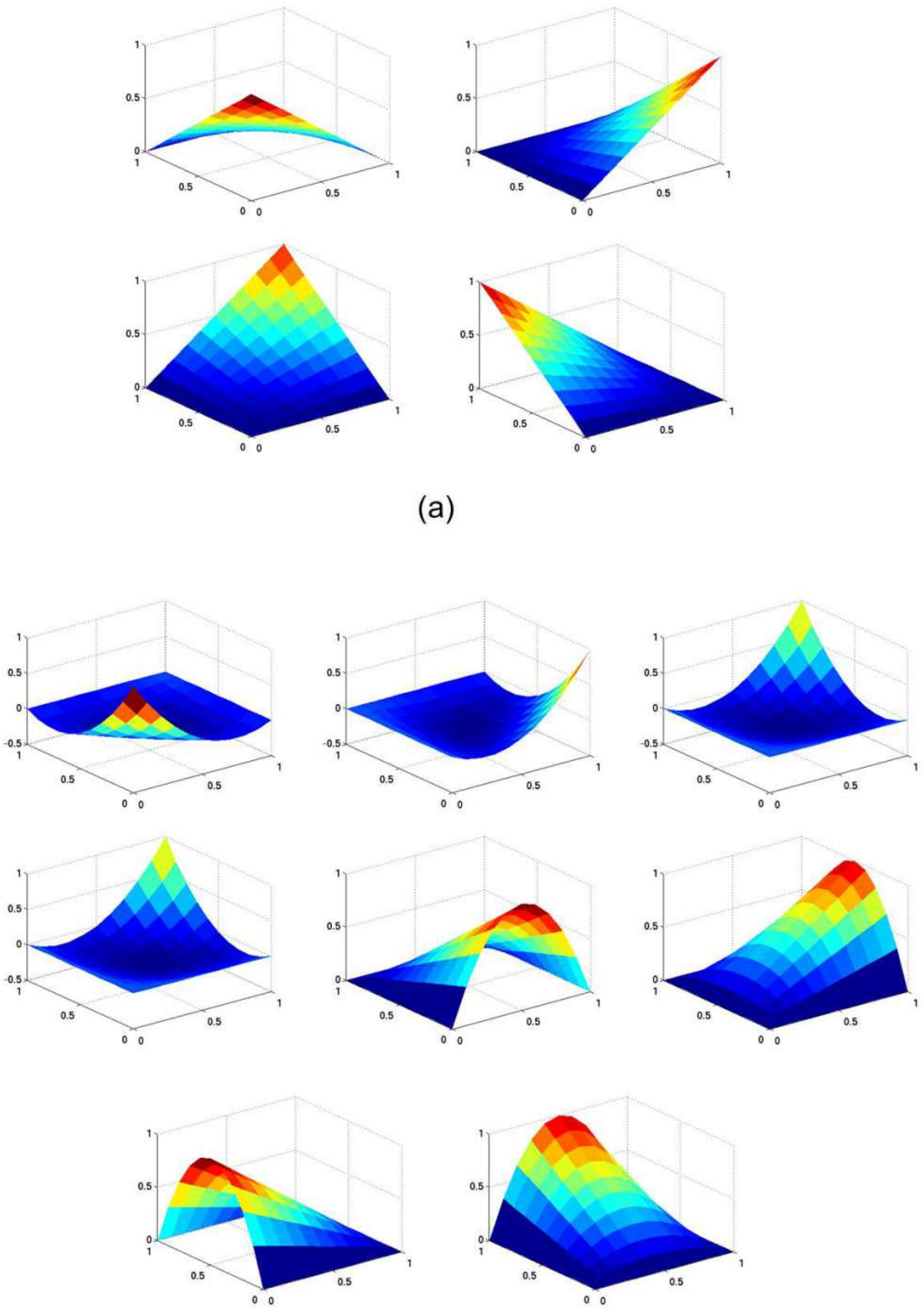

(a)

(b)

Figure 3.5.: Basis functions defined in 2D domains. Linear (a) and quadratic (b) functions in quadrilateral domains.

3.1.5. Geometrical Interpretation of FEM

The manner in which the FEM was presented in this work makes the geometrical interpretation of the method a natural consequence. In this section it will be shown that this concept is intimately connected to the error of the linear space discretization of the FEM. In order to proceed smoothly through the upcoming discussion, consider that the linear space V is endowed with inner products for real functions defined by

$$< f, g >= \int f' g' dx \ . \tag{3.19}$$

Furthermore, consider the norm induced by the inner product (3.19) as

$$\| f \| = \int f^2 dx \ . \tag{3.20}$$

Consequently, the variational form (3.5) and the discrete variational form (3.10) can be rewritten as

$$< u, v >= \int f v dx \qquad \forall v \in V \tag{3.21}$$

and

$$< u_h, v >= \int f v dx \qquad \forall v \in V_h \ . \tag{3.22}$$

The discrete problem solution (u_h) is computed by FEM as seen in the previous sections, but the exact solution of the BVP problem is given by solving the continuous variational form. Therefore, it is natural to ask how distant u_h is from u. The answer of this question leads to a geometrical view of the FEM.

Consider $v \in V_h$. The function v also belongs to V since $V_h \subset V$. Therefore, for every $v \in V_h$ (3.22) can be subtracted from (3.21), given by

$$< u_h - u, v >= 0 \qquad \forall v \in V_h \ . \tag{3.23}$$

As an inner product, (3.19) must hold the orthogonality property ($< f, g >= 0 \Leftrightarrow f \perp g$). This means that the discretization error $(u_h - u)$ is orthogonal to the space V_h. As a consequence, the solution u_h is the orthogonal projection of the exact solution u in V_h. Fig. 3.6 illustrates this principle.

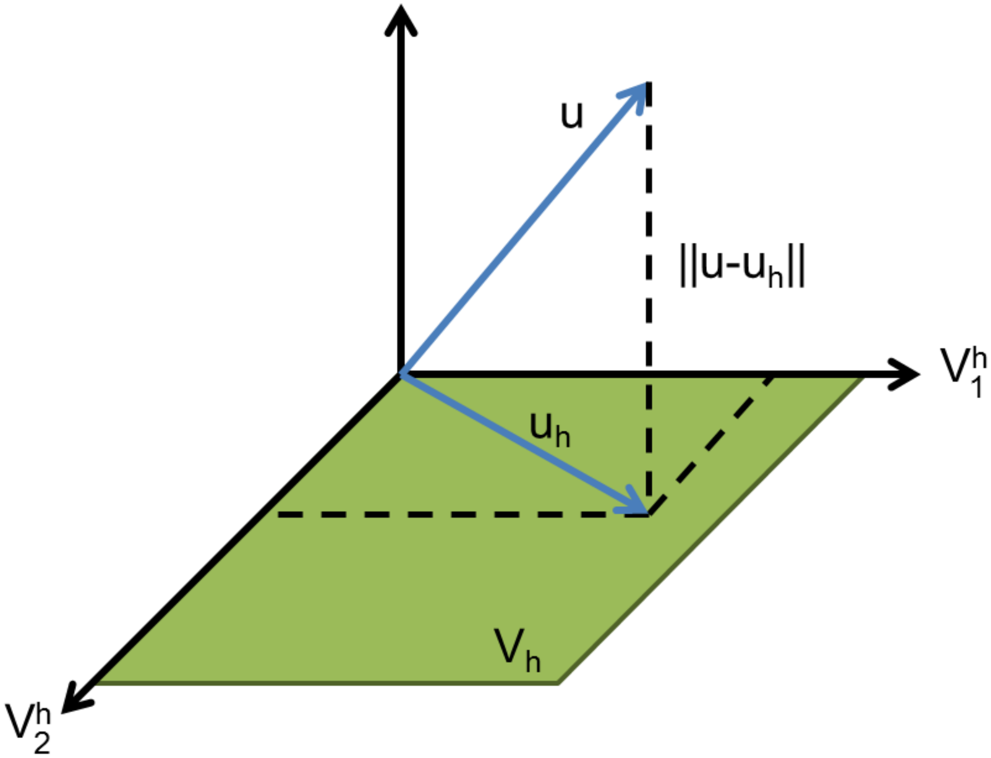

Figure 3.6.: Geometrical interpretation of Galerkin's method. The solution (u) of the original problem is projected (u_h) in the space defined by the basis of V_h. Galerkin's method can be understood as the procedure to find this projection.

As a result of the orthogonal projection, the element u_h is the closest function to u in comparison to all elements of V_h. Hence, the error of discretization is bounded according to [56]

$$\|u - u_h\| = \|u - v\| \qquad \forall v \in V_h \ . \tag{3.24}$$

The relation (3.24) will not be proved here, but it is intuitively clear when orthogonal projections are kept in mind. In conclusion, FEM provides the best approximation of the exact solution u in the discretized space V_h, when the norm (3.20) is considered.

At this point, the advantage of the original Galerkin's imposition for the solution u and the test function v becomes evident – u_h and v_h, respectively, for the discrete formulation – to reside in the same linear space. The formulation gains some formal support, especially regarding the discretization error, since it is guaranteed that the FEM solution is the best choice in a particular space.

3.1.6. Final Remarks on FEM

The Finite Element Method is a vast and still very active subject of research. This text is not intended to discuss it exhaustively, but to give a first intuitive approach and still formal enough to understand this work. However, some points are still open, for instance, an understanding of the conditions under which the FEM converges is still needed. As mentioned previously, one expects that the discretized solution (u_h) converges to the exact solution (u) by increasing the V_h space dimension – in other words, increasing the number of mesh points. Actually, this discussion leads to restrictions of the basis functions to ensure FEM convergence (and also stability) [56][59]. An in-depth treatment about this topic can be found in specific functional analysis texts, as well as in FEM books [56][57][59].

Another point of contention is the boundary conditions. In the previous sections, only specific Dirichlet boundary conditions [61] were discussed. Indeed, for general Dirichlet conditions all the previous results remain unchanged, less a constant, but for Neumann boundary conditions [61] a new development is needed, especially for the equivalence between the BVP problem and the variational formulation. The procedure for deriving FEM is still the same, as well as the conclusions, but the arguments must be modified to include this kind of situation. A self-contained text about this subject can be found in traditional FEM references [56]; in addition, an example with a Neumann boundary condition will be provided in the next section.

3.2. Elasticity with FEM

Static equilibrium is the most common situation for mechanical problems in semiconductor devices. In equilibrium, the sum of forces (and momentum) in a body must be zero, including those produced by stress. In order to derive the equilibrium equations consider an infinitesimally small solid and the stress distribution on its faces, as depicted in Fig. 3.7.

Each stress component is assumed to be a continuous differentiable function of x, y, and z. Hence, they can be expanded by Taylor series and the stress on the faces of the infinitesimal cube can be arranged as

$$\sigma_{ij}(x+\Delta x, y, z) = \sigma_{ij}(x,y,z) + \frac{\partial \sigma_{ij}}{\partial x} + O(h^2), \qquad i,j \in \{x,y,z\}\ , \tag{3.25}$$

$$\sigma_{ij}(x, y+\Delta y, z) = \sigma_{ij}(x,y,z) + \frac{\partial \sigma_{ij}}{\partial y} + O(h^2), \qquad i,j \in \{x,y,z\}\ , \tag{3.26}$$

$$\sigma_{ij}(x, y, z+\Delta z) = \sigma_{ij}(x,y,z) + \frac{\partial \sigma_{ij}}{\partial z} + O(h^2), \qquad i,j \in \{x,y,z\}\ . \tag{3.27}$$

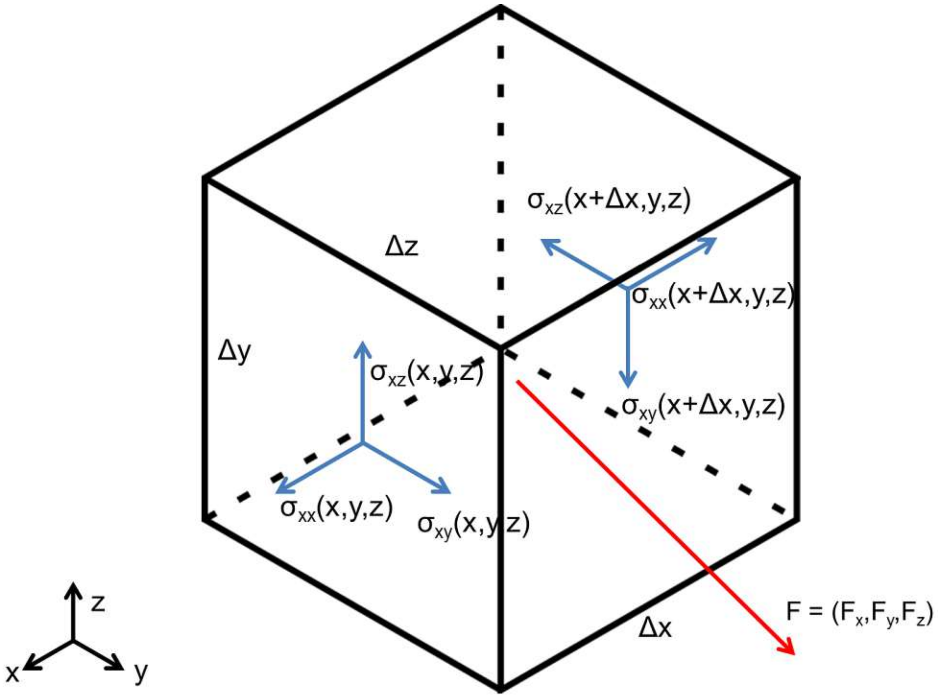

Figure 3.7.: Inifinitesimally small stress cube. The stress is defined in the face of the cube, however only σ_{xx} is explicitly shown. The others are omitted for the sake of clarity in the picture.

The body can be under the influence of an external disturbance (e.g. gravity), which must be considered in the equilibrium equations. In Fig. 3.7 the sum of all external forces is represented by the vector F. The equilibrium of forces in the x-direction can be obtained by

$$\begin{aligned}
&\left(\sigma_{xx} + \frac{\partial \sigma_{xx}}{\partial x}\Delta_x\right)\Delta_y\Delta_z - \sigma_{xx}\Delta_y\Delta_z + \\
&\left(\sigma_{yx} + \frac{\partial \sigma_{yx}}{\partial x}\Delta_x\right)\Delta_y\Delta_z - \sigma_{yx}\Delta_y\Delta_z + \\
&\left(\sigma_{zx} + \frac{\partial \sigma_{zx}}{\partial x}\Delta_x\right)\Delta_y\Delta_z - \sigma_{zx}\Delta_y\Delta_z + f_x = 0 \; , \\
&\frac{\partial \sigma_{xx}}{\partial x} + \frac{\partial \sigma_{yx}}{\partial x} + \frac{\partial \sigma_{zx}}{\partial x} + \frac{f_x}{\Delta_y\Delta_z} = 0 \; , \qquad (3.28)
\end{aligned}$$

where f_x is an external force in the x-direction. A similar treatment can be applied in the y-direction and the z-direction. Thus, the equilibrium equations can be summarized by

$$\begin{cases} \dfrac{\partial \sigma_{xx}}{\partial x} + \dfrac{\partial \sigma_{yx}}{\partial y} + \dfrac{\partial \sigma_{zx}}{\partial z} + \dfrac{F_x}{\Delta_y \Delta_z} = 0 \\ \dfrac{\partial \sigma_{yy}}{\partial x} + \dfrac{\partial \sigma_{yx}}{\partial y} + \dfrac{\partial \sigma_{yz}}{\partial z} + \dfrac{F_y}{\Delta_x \Delta_z} = 0 \\ \dfrac{\partial \sigma_{zz}}{\partial x} + \dfrac{\partial \sigma_{xz}}{\partial y} + \dfrac{\partial \sigma_{yz}}{\partial z} + \dfrac{F_z}{\Delta_x \Delta_y} = 0 \end{cases} , \tag{3.29}$$

where F_x, F_y and F_z are the external forces per unit area in the corresponding Cartesian direction.

A great deal of mechanical analysis in microelectronics relies on the elastic theory. However, solving its fundamental equation is challenging. The solution is usually unknown for varying geometries and conditions faced by the engineering design. The few known solutions are only available to simple geometries (e.g. circle, square) and restricted conditions, which can lead to an oversimplification of the analysis. In order to enhance the mechanical analysis, FEM can be used to compute the elastic equations on general geometries and conditions. It provides means to simulate elastic problems by discretizing its fundamental equations.

To a generalized treatment of elastic problem by FEM, consider the problem depicted in Fig. 3.8. The presented problem is rather general concerning geometry and conditions. Dirichlet and Neumann boundary conditions are presented ($u = 0$ on $\partial\Omega_2$ and $\bar{\bar{\sigma}}.\boldsymbol{n} = \boldsymbol{g}$ on $\partial\Omega_1$, respectively). Additionally, the shape is amorphous, meaning no preferred geometry.

Within this section, a tensorial treatment will be used for the sake of notation simplicity. A table with tensorial definitions, properties and operations is available in the appendix.

The body is assumed to be in static equilibrium; therefore (3.29) must be satisfied. The system (3.29) can be rewritten in its tensorial form for convenience together with its boundary conditions by

$$\begin{gathered} -\nabla.\bar{\bar{\sigma}} = \boldsymbol{F} \\ u = 0 \text{ on } \partial\Omega_2 \qquad \bar{\bar{\sigma}}.\boldsymbol{n} = \boldsymbol{g} \text{ on } \partial\Omega_1 \ . \end{gathered} \tag{3.30}$$

Following the same procedure to derive the FEM in the last session, (3.30) is multiplied by a function v. However, this time $v \in (V \times V \times V = V^3)$ is a vectorial function. Since the static equilibrium problem is three-dimensional, a test function is needed for each dimension. The multiplication result is described by

$$-\int_\Omega (\nabla.\bar{\bar{\sigma}}).\boldsymbol{v} = \int_\Omega \boldsymbol{F}.\boldsymbol{v} \ . \tag{3.31}$$

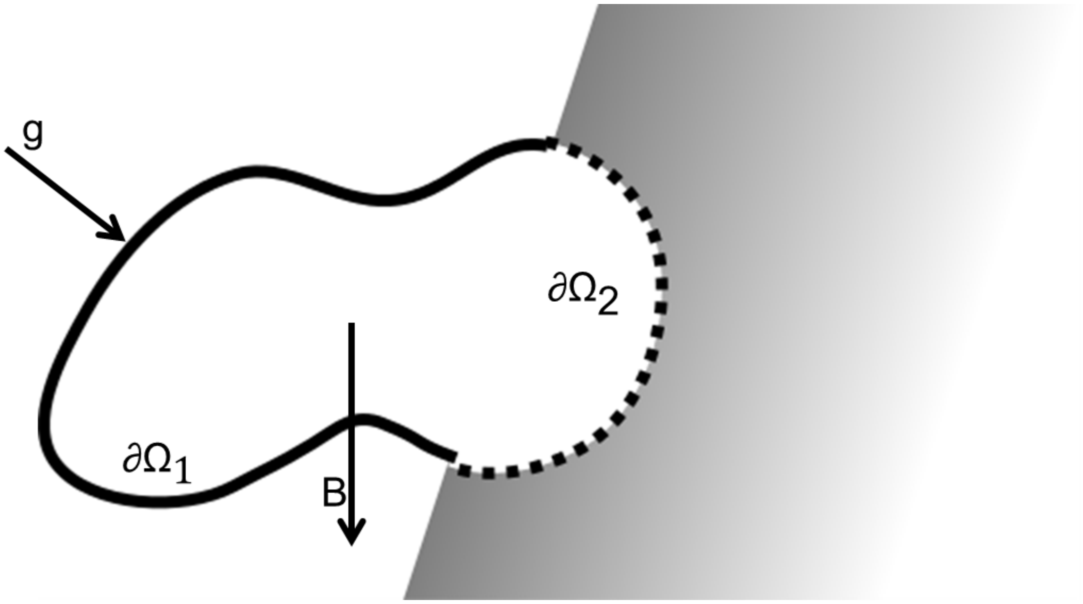

Figure 3.8.: General elastic problem. B is the body force and g an external load. The surface $\partial\Omega_1$ is free to move, while $\partial\Omega_2$ is constrained.

The next step is the simplification of (3.31). In the last section the integration by parts was used. For the current case, the first Green identity as described in [62] is applied

$$\int_{\Omega} (\nabla . \bar{\bar{\Gamma}}) . \boldsymbol{w} + \bar{\bar{\Gamma}} : (\nabla \boldsymbol{w}) = \int_{\partial\Omega} (\bar{\bar{\Gamma}} . \boldsymbol{w}) \boldsymbol{n} \ , \tag{3.32}$$

where $\bar{\bar{\Gamma}}$ is a second order tensor and $\boldsymbol{w}$ is a vector. An intriguing fact is that (3.32) is the equivalent of the integral by parts in higher dimensions. Proceeding with the proper substitution of (3.32) in (3.31) and some rearrangement, (3.31) can be rewritten as

$$\int_{\Omega} \bar{\bar{\sigma}} : (\nabla \boldsymbol{v}) = \int_{\Omega} \boldsymbol{F} . \boldsymbol{v} + \int_{\partial\Omega} (\bar{\bar{\sigma}} . \boldsymbol{v}) \boldsymbol{n} \ . \tag{3.33}$$

So far, the equilibrium equations were stated in terms of the stress tensor, but the real unknown is the displacement. As seen previously (Section 2.2.1) stress and strain can be derived from displacement but the opposite is not as straightforward. Furthermore, the description by means of stress challenges the imposition of boundary conditions on the displacement field. Hence, a tensorial description of stress and strain is considered using

$$\bar{\bar{\sigma}} = \left[\frac{E\nu}{(1+\nu)(1-2\nu)}\nabla.\boldsymbol{u}\right]\bar{\bar{I}} + \frac{E}{1+\nu}\bar{\bar{\epsilon}}(\boldsymbol{u}) \tag{3.34}$$

and

$$\bar{\bar{\epsilon}} = \frac{1}{2}\left[(\nabla\boldsymbol{u})^T + \nabla\boldsymbol{u}\right] \ , \tag{3.35}$$

respectively. Consistently, the definitions (3.34) and (3.35) are equivalent to (2.22) and (2.10), but in Section 2.2.1 the physical meaning of the equations was preferred over simplicity.

Finally, substituting (3.34) and (3.35) in (3.33) the variational formulation of (3.30) is obtained as

$$\text{Find } \boldsymbol{u} \in (V^3) \text{ such that} \qquad \forall v \in (V^3)$$

$$\int_\Omega \left[\frac{E\nu}{(1+\nu)(1-2\nu)}(\nabla.\boldsymbol{u})(\nabla.\boldsymbol{v})\right] + \frac{G}{2}\left[(\nabla\boldsymbol{u})^T + \nabla\boldsymbol{u}\right] : \nabla\boldsymbol{v} = \int_\Omega \boldsymbol{F}.\boldsymbol{v} + \int_{\partial\Omega} \boldsymbol{g}.\boldsymbol{v} \ . \tag{3.36}$$

From this point the same development of the previous section can be implemented. Therefore, the coordinate space V^3 is dicretized (a basis set for each dimension), the basis functions are chosen following the pre-established criteria and the linear system is built. Recall the previous discussion regarding 2D and 3D problems, which fit to this analysis.

For this specific problem, those aspects will not be discussed here, but they are available in several textbooks about the FEM in mechanical problems [57]. Furthermore, they are not essentially different from the 1D problem presented in the previous section. The dimensional generality of FEM is an asset of the technique.

3.3. Time Dependent Problems

Time dependence analysis is not particularly interesting for elastic deformations, since the material recovers entirely after load removal. However, for plastic deformations, the duration of a force application defines the amount of permanent deformation within the body. Actually, plasticity has an elegant treatment with the FEM, which has been developed along the years [40]. Although plastic deformation is studied in this work, the classical approach of plasticity is not used. Instead, a specific model based on ordinary differential equations (ODE) is employed as will be discussed in Chapter 5.

This section intends to provide the background for the treatment of these kinds of equations. Time dependent problems can be presented in the general form by [63]

$$\frac{df}{dt} = g(t, f(t)), \qquad f(t_0) = f_0 \; . \tag{3.37}$$

These types of equations, where the solution to the first step ($f(t_0) = f_0$) is known, are defined as initial value problems (IVP). High order ODEs can always be converted to a system of N first order equations in the same form as (3.37) by substitution. For example, the ODE $f'' = x$ can be rewritten as $f' = u$ and $u' = x$.

In general, the strategy for solving (3.37) numerically consists of the division of the domain into small time steps; and for each step the solution is computed as shown in Fig. 3.9.

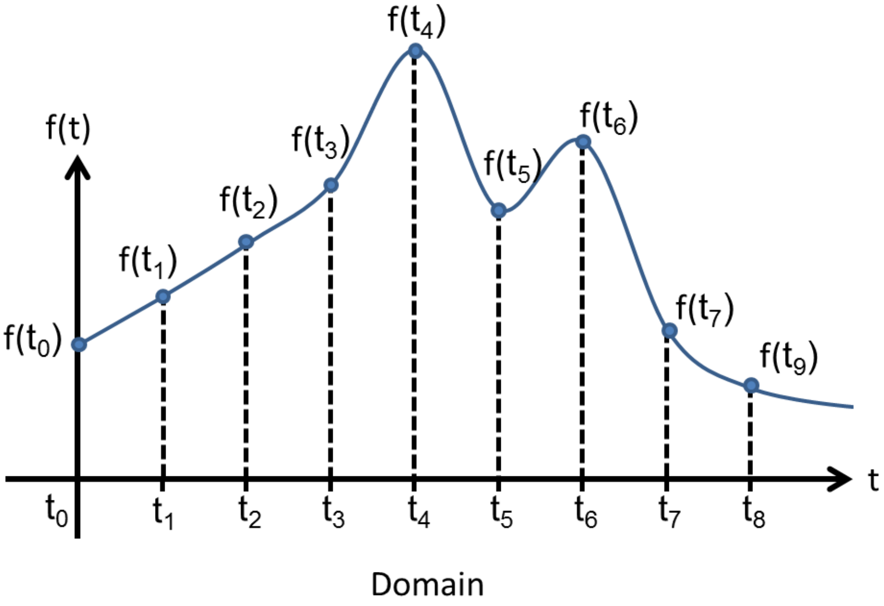

Figure 3.9.: Partioning of the domain in time steps. The solution is computed at each time step.

Numerical methods for ODEs can be divided between explicit and implicit methods. The former handles (3.37) by computing the next state of the system based solely on the current state ($f(t + \Delta t = Y(f(t))$), while implicit methods require also the future state ($f(t + \Delta t) = H(f(t), f(t + \Delta t))$). The formulation of implicit methods seems rather paradoxical, but in practice only an estimation of the future state is used to compute H. Explicit methods are more intuitive and easy to implement, but they require an unreasonable number of steps to properly approximate problems with fast variations, the so called stiff problems, for which implicit methods are more suitable.

In order to exemplify both categories, consider the approximations for the derivatives

$$\frac{df}{dt}(t) \approx \frac{f(t+\Delta t) - f(t)}{\Delta t} \tag{3.38}$$

and

$$\frac{df}{dt}(t) \approx \frac{f(t) - f(t-\Delta h)}{\Delta t} \; . \tag{3.39}$$

Substituting (3.38) and (3.39) in (3.37) the relations hold

$$f(t+\Delta t) \approx f(t) + \Delta t g(t, f(t)) \; , \tag{3.40}$$

$$f(t) \approx f(t-\Delta t) + \Delta t g(t, f(t)) \; . \tag{3.41}$$

One can notice the particular difference between the representation of (3.40) and (3.41). For the first case the unknown variable ($f(t+\Delta t)$) is defined explicitly by the terms on the right hand side. In the second case the unknown ($f(t)$) is needed in order to compute the function g, which leads to an implicit definition of $f(t)$. Each equation defines a method for the solution of (3.37), where (3.40) is known as the Euler method and (3.41) as backward Euler method.

In the scope of this work, implicit methods are more relevant, mainly because of exponential variations in the models for describing plasticity in Chapter 5. The so called Back Differentiation Formula (BDF) is the employed method for ODEs. The BDF method approximates the function f by a Lagrangian polynomial as defined by [64]

$$f(t) \approx P_{s-1}(t) = \sum_{m=0}^{s-1} p_m(t) f(t_{n+m}) \; , \tag{3.42}$$

$$\textit{where} \qquad p_m(t) = \prod_{j=0; j\neq m}^{s-1} \frac{t + t_{n+l}}{t_{n+m} - t_{n+l}}, \qquad m = 0, 1, ..., s-1 \; .$$

The meaning of s will become clear soon, but right now $(s-1)$ can be understood as the degree of the Lagrange polynomial. From the polynomial definition (3.42) the BDF method can be built. The derivative of $f(t)$ is approximated by the derivative of the Lagrangian polynomial as described by

$$f(t) \approx P_{s-1} = g(t_n, t_{n-1}, ..., t_{n-s}, f_n, f_{n-1}, ..., f_{n-s}) \; . \tag{3.43}$$

From (3.43) one can see that s defines the number of past states, which is used to calculate the current state of the system. As s increases the local error of the method reduces, but for $s > 6$ the BDF is no longer convergent. Naturally, higher values of s imply higher computational demands; hence a compromise between speed and accuracy must be met. Table 3.1 represents the BDF method after expansion of the Lagrangian polynomial for $1 < s < 5$.

Table 3.1.: Expansion of the Lagrangian polynomial for $1 < s < 5$.

Order	Expression
BDF 1	$y_{n+1} - y_n = hf(t_{n+1}, y_{n+1})$
BDF 2	$y_{n+2} - \frac{4}{3}y_{n+1} + \frac{1}{3}y_n = \frac{2}{3}hf(t_{n+2}, y_{n+2})$
BDF 3	$y_{n+3} - \frac{18}{11}y_{n+2} + \frac{9}{11}y_{n+1} - \frac{2}{11}y_n = \frac{6}{11}hf(t_{n+3}, y_{n+3})$
BDF 4	$y_{n+4} - \frac{48}{25}y_{n+3} + \frac{36}{25}y_{n+2} - \frac{16}{25}y_{n+1} + \frac{3}{25}y_n = \frac{12}{25}hf(t_{n+4}, y_{n+4})$
BDF 5	$y_{n+5} - \frac{300}{137}y_{n+4} + \frac{300}{137}y_{n+3} - \frac{200}{137}y_{n+2} + \frac{75}{137}y_{n+1} - \frac{12}{137}y_n = \frac{60}{137}hf(t_{n+5}, y_{n+5})$

In practice, the computation for each time step requires the solution of a non-linear equation. Newton's method is the most common choice for solving the non-linear problem, but other methods can be more suitable, depending on the form of g. As an initial guess, an explicit method (such as the Euler method) can be used to provide a reasonable choice for $f(t_n)$.

Naturally, the effort to compute the solution at each time step is bigger for BDF methods than for explicit methods, but the argument for their utilization lies on the stability. Implicit methods are more stable than explicit methods, an important feature for the numerical solution of stiff ODEs. Such problems are by definition numerically unstable, which means that small deviations of the solution in a particular step lead to a large error in the subsequent steps. In fact, it can be proved that for $s = 1$, the BDF is A-stable [64]. This means that for an ODE in the form $y' = ky$, the exact solution ($y = e^{kx}$) and the BDF solution are asymptotically equivalent for $k < 0$. Such a condition is only valid in the Euler method for very small time steps [64]. Evidently, $y' = ky$ is not a general case, but it is commonly used as a test problem to evaluate the stability of numerical methods for ODEs.

4. Mechanical Impact of TSVs in Silicon

This chapter initiates a discussion about the mechanical aspects of TSVs. The main goal here is to provide a framework to assess the mechanical impact of the TSVs in their surroundings. First, the materials employed in TSVs and how their properties influence a via's design is discussed. Afterward, the discussion proceeds with the mechanical impact of a via on its surroundings, especially during thermal variations. Finally, strategies for TSV placement are presented as well as methods for calculating the keep away zone.

4.1. Properties of Interconnect Materials

The full functionality of an IC cannot be reached with the use of a single isolated device. It requires an engineered interconnected network, which enables the proper communication between the different components (e.g. resistors, capacitors, diodes, transistors, and more). The interconnections should behave akin to an ideal wire and minimize the disruption of the signal flux inside the circuit.

Interconnections may be composed by conductive lines, vias, wires, pads, and joints [65]. Each of these components can be formed by different materials. Metals and theirs alloys are usually the best choice for building interconnections, due to their high electrical conductivity. In the very beginning of the semiconductor industry aluminum and copper were the most common metals, but with the increasing demand for performance, integration, and reliability a wider variety started to be employed, such as tin, tungsten, zinc, gold, and nickel [66].

The introduction of metal structures inside semiconductor devices creates several problems. For instance, metals have a large CTE when compared to silicon, therefore during thermal variation, stresses arise due to the thermal mismatch between the materials. Furthermore, the manufacturing process is also very challenging. Metals are usually deposited by employing various methods, such as Chemical Vapor Deposition (CVD), Physical Vapor Deposition (PVD), and their variations [38][66]. Each method has its particularities regarding material quality, adhesion, and mechanical properties, which also must be considered when attempting to generate reliable devices[38].

To overcome all the challenges of an interconnection fabrication, the implemented materials and their interactions with the silicon must be understood. Each part of an interconnection demands a specific approach. In this work the focus stays with vias and the materials most frequently found in a via structure.

Vias are the elements responsible for the vertical connections in a device. They make the bridge between the different metal lines and, in the case of TSVs, between dies. Aluminium, copper, and tungsten are the most common conduction metals, but there is a large assortment of other materials required to support via fabrication. Some of these materials and their purpose are present in Table 4.1.

Table 4.1.: Melting point and electrical resistivity of common interconnection materials. The materials are grouped by their function within an interconnect structure.

Function	**Material**	**Melt. point (°C)**	**Electr. resist.** ($\mu\Omega$/cm)	**Ref.**
Metal	Al	1084	1.70	[67]
	Cu	660	2.70	[44]
	W	3410	5.65	[43]
Silicides	PtSi	1229	25-35	[68]
	$TiSi_2$	1540	13-16	[69]
	WSi_2	2165	50	[70]
	$CoSi_2$	1326	18-20	[70][71]
	NiSi	992	14-20	[70][72]
Barriers, glues and passivations	TiN	2950	25	[47]
	Ti_xW_{1-x}	220	NA	
	N+ polysilicon	1410	NA	[73]

The function of each type of material can be summarized in the following:

- Silicides are used as a conductive material only in local regions of the structure, which have to be exposed to high temperatures or oxidizing environment.
- Barriers are applied to prevent diffusion of metal atoms toward silicon, minimizing the risk of contamination and current leakage.
- Glues are needed to improve the adhesion of metal films in the silicon surface, avoiding delamination problems which could lead to a via failure.
- Passivation materials are protective coating against the hazards of the ambient.

As seen in Table 4.1, copper is the most suitable material regarding electrical conductivity, but it was not used in large scale production as the conductive material in a via until 1997. Several challenges were present which limited copper deposition, such as patterning difficulties and silicon contamination. Volatile copper compounds were unknown and the technology at the time required such compounds for metal deposition [74]. The problem was overcome through the invention of the dual damascene process which patterns the silicon itself by etching and filling the created trenches and vias with copper [74][75][76].

Silicon contamination was solved by the application of barriers metals (e.g. Ta, TaN), which must prevent copper diffusion without drastically reducing the conductivity, otherwise there is no benefit for copper utilization[75][76][77].

Before 1997, tungsten (vias) and aluminium (lines) were the dominant interconnection materials [66]. The processing of Al-W interconnections is easier in comparison to the processes required to generate copper based vias [66]. They do not face the severe problems of silicon contamination and volatile compounds are known and available. Moreover, aluminium and tungsten mechanical properties are more compatible with silicon, i.e., aluminium and tungsten enjoy a lower CTE mismatch and higher melting point than copper.

The effort required to incorporate high conductivity metals is justified only for some industrial applications. The high conductivity metal allows for the creation of smaller and more energy efficient devices, a very important feature in general purpose processors.

The idea behind a TSV is not different from the traditional via. Both are vertical connections, but the dimension of the TSVs are much larger in comparison to the metal line vias. Therefore, mechanical properties become much more relevant than before. The manufacturing of TSVs demand a more careful design to manage the increasing mechanical instability of the structure.

4.2. Design of TSVs

Through Silicon Vias are large structures in comparison to the components inside the device. The TSVs radius can span from 5μm up to 300μm and the height usually follows aspect ratios from 1:1 up to 1:10 in relation to the radius [29][78]. Therefore, if CMOS 90nm technology is considered, a TSV would solely occupy the area of, at least, several thousands of transistors. Such a large metal structure in the middle of the device generates considerable stress, which can lead to device malfunction and cracks in the silicon.

Thermal and residual stresses account for several reliability issues in TSVs. Consequently, they have become a major concern in mechanical stability designs [79][80][81]. The thermo-mechanical stress arises from the difference between the coefficient of thermal expansion (CTE) of silicon – which surrounds the via – and the interconnection metal. Meanwhile, the residual stress results from different physical mechanisms which take place during metal deposition.

The impact of each stress component can be controlled by the choice of materials and the geometry forming the TSV. A good design should manage the mechanical issues while not compromising the electrical properties of the device. One of the most common and well documented layouts is the cylindrical copper TSV. The good electrical properties of copper and the ease of fabrication are an advantage of this technology. However, the difference of more than one order of magnitude between silicon CTE and copper CTE compromises its mechanical reliability.

CTE mismatch can be compensated with various strategies, for instance by the use of polymer liners around the TSV [82]. The liners work as a barrier which absorbs the stress and hinder its propagation towards the silicon. Another approach is the use of an open (unfilled) TSV instead of a filled via [82][83]. This scheme reduces the amount of material in the structure and provides room for the metal to expand freely towards the axis of the via, leading to an overall stress reduction (depending on the metal properties as will be discussed in the next section). Additionally, the stress induced by the TSVs in the silicon can be attenuated by their particular placement [83]. A device usually has several vias close to each other, which can be arranged in such a way that the stress is mutually cancelled or reduced between them.

Circular shaped TSVs are preferred over other polygonal geometries. Such designs results in stress accumulation points in the corners without bringing any particular advantage to the overall process complexity or device performance.

This work attempts to cover two of the most frequent types of TSVs, filled TSVs and unfilled (open) TSVs. However, special attention is given to the open TSVs due to a lack of documentation and available information in the literature. Although the TSVs can generally be classified in two types, each TSV technology has minor modifications to handle local stress problems or even to treat processing challenges such as layer delamination, material diffusion or to improve layer adhesion. In order to establish a common ground for discussion, during this work two standard TSVs are considered, as shown in Fig. 4.1: one for filled vias and another for unfilled vias. Any deviation from the standard discussion of TSV performance and reliability will be properly addressed and explained in the text. The design is based on a previous TSV technology [8][29], for which experimental data were available.

4.3. Evaluating TSVs' Mechanical Impact

During operation, the device is expected to work properly in the temperature range of -40°C to 125°C. The goal here is to assess the mechanical response of the structure in this scenario considering a stress free temperature of 25°C, although, the existence of residual stress in the metal layer of the TSV is known [85]. Pre-stress in elastic simulations would only bias the final stress without major modifications to the general behavior. Furthermore, residual stress has a much more local effect as will be described in Chapter 5. Plasticity was also neglected, because its effects are destructive for the devices in silicon. Therefore, any TSV design should keep the stress in the silicon below the plastic threshold.

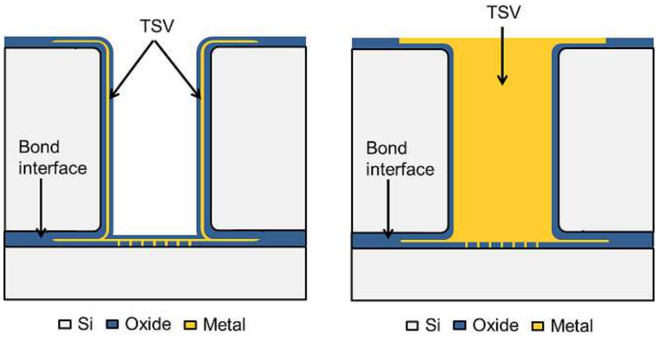

(a) (b)

Figure 4.1.: Schematic of the standard TSVs considered in this work for unfilled (a) and filled (b) technology. The vias have a 100μm diameter and 250μm height. Filled TSVs are usually smaller than the one presented here, however, the dimensions were chosen in order to allow for a fair comparison between both technologies.

4.3.1. Thermo-mechanical Simulation of TSVs

FEM simulations were carried out to understand the stress behavior in the TSV structure under the aforementioned conditions. For unfilled vias the meshing process is a challenging task. The thin layers of metal and oxide require a very fine mesh, in order to have a good approximation of the solution in those layers and in the regions surrounding them. Additionally, the cylindrical symmetry of the structure can be used to reduce the size of the problem, speed up the meshing process, and the simulation. In spite of that, one-quarter of the structure is employed in this section. The purpose of this increase in computational burden was to prepare the setup for the cases where the geometry symmetry can not be exploited, as will be seen in section 5.3.1.

Quadratic basis functions were used for the solution approximation and the BicGStab method for the linear solver [64]. Pre-conditioning is needed in order to obtain reliable results, especially in the case of the unfilled TSV, since the difference between the thin layers and the rest of the structure leads to scaling issues in the linear system. It is also possible to approach this problem by reducing the local meshing growth rate, but this would increase the size of the linear system and slow down the simulation.

Von Mises stress plots are shown in Fig. 4.2 and Fig. 4.3 for the unfilled and the filled geometry, respectively. During thermal cycling, geometrical features influence the distribution of mechanical stress, especially on the top and the bottom of the via. One can see that the highest stress occurs in the metal layer at the bottom and near the top of the structures. In those regions the structures are under the influence of two factors: the thermal mismatch between the metal and the surrounding layers and the geometry. High mechanical stress in connection with microstructural properties, which weaken the stability of the crystal (dislocations, grain boundaries), can cause a fracture in the metal layers resulting in a complete failure of the TSV.

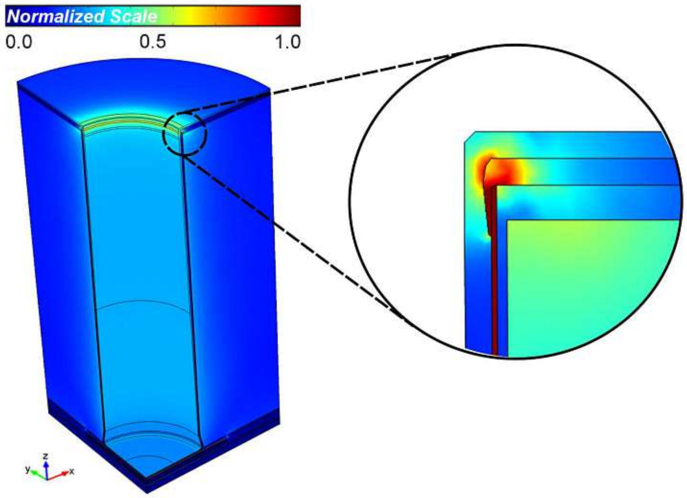

Figure 4.2.: Von Mises stress in the unfilled TSV. As depicted in the inset the top corner of the via is a point of high stress, especially in the oxide. Naturally, the metal sustains the highest stress in the structure. However, oxides are usually not as resistant to mechanical stress as copper or tungsten. The scale is normalized to the maximum stress obtained for this setup.

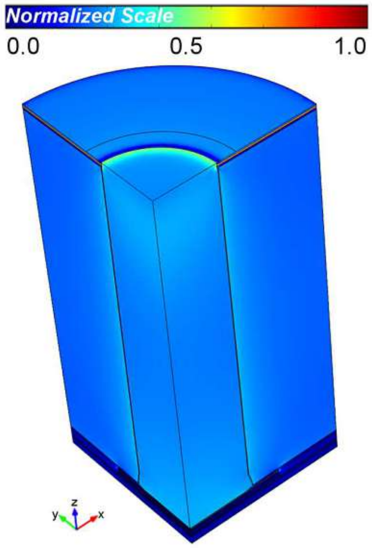

Figure 4.3.: Von Mises stress in the filled TSV. The stress pattern is similar to the unfilled TSV (including the high stress spot at the top). However, the overall stress in the silicon is higher than the stress in the unfilled TSV. The scale is normalized to the maximum stress obtained for this setup.

A two-dimensional cross section through the middle of the TSV provides a better view of the stress development through the silicon, as shown in Fig. 4.4. The stress distribution in the two designs are very similar in shape but not in magnitude.

For both geometries the stress decays very quickly towards the silicon, but the mechanical advantage of one TSV over the other is highly dependent on the choice of metal present in the via. To clarify this argument, Fig. 4.5 shows the von Mises stress in the silicon along the radial direction, when copper or tungsten are considered as conductive metals.

For unfilled TSVs the stress in the silicon is practically independent of the employed metal, due to the freedom of expansion toward the via's middle axis. Actually, the stress induced by thermal variations on the surface of the open TSVs wall is essentially zero. In filled TSVs the situation is very different. The metal is constrained by the silicon and there is no freedom of expansion. Hence, a CTE mismatch between

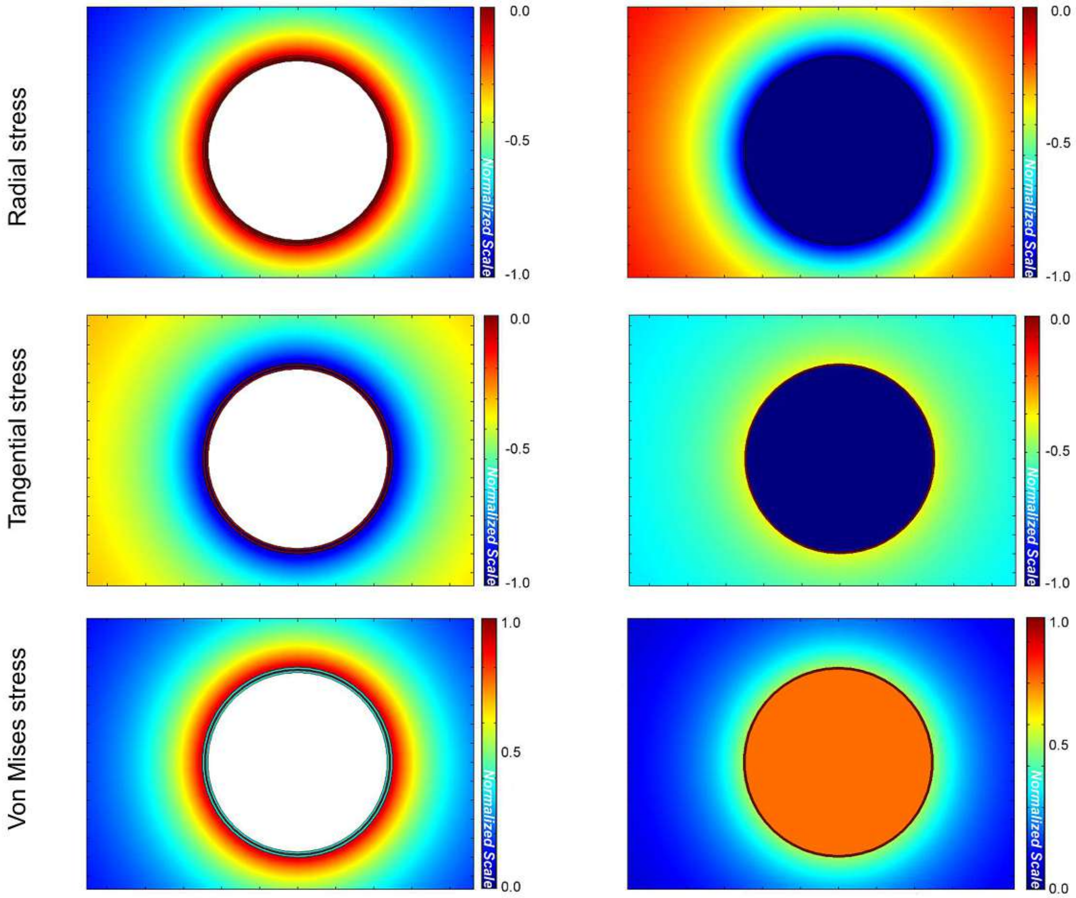

Figure 4.4.: Stress fields in the unfilled TSV (left) and filled TSV (right). Cylindrical coordinates are used to simplify the analysis.

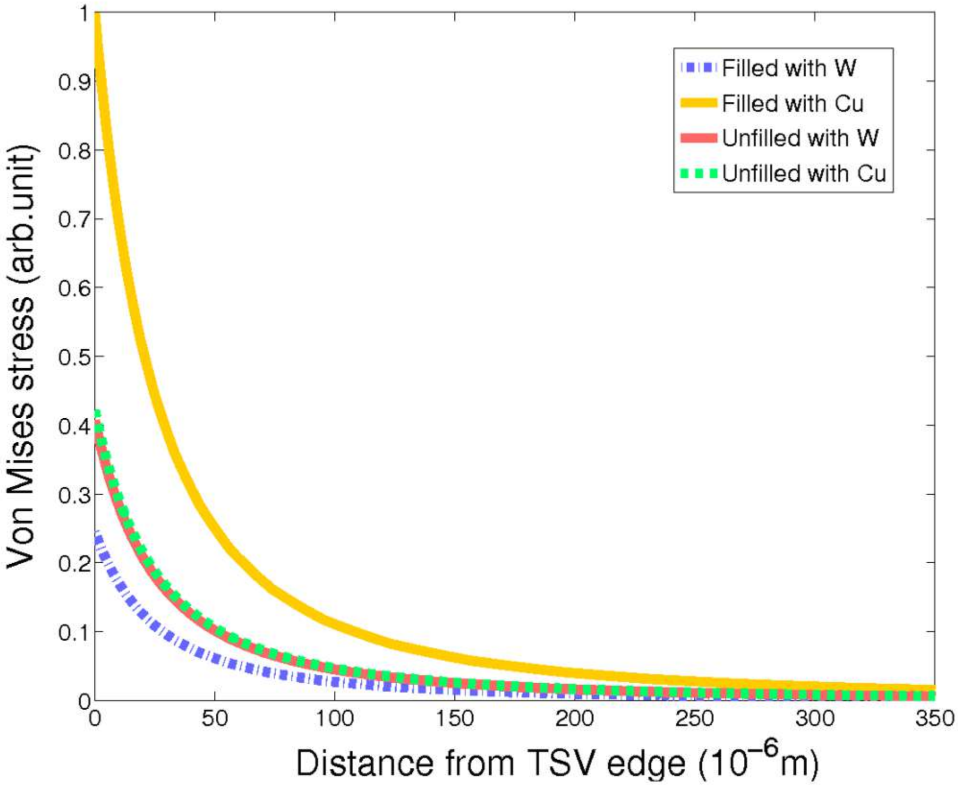

Figure 4.5.: Von Mises stress through the silicon layer along the radial direction through the middle of the TSV height. For the unfilled TSV the choice of material is negligible for the stress level in the silicon. Most of the stress is produced by the geometry itself. In the filled TSV the metal plays a significant role. A large difference between the CTE of silicon and the metal creates high levels of stress, as shown by the Cu filled TSV.

the silicon and metal defines the stress behavior. Copper has a CTE almost ten times larger than silicon, therefore during thermal variation it will apply significant pressure to the silicon in order to expand, leading to higher stress in comparison to the unfilled TSVs. Alternatively, tungsten is very thermally compatible with silicon (low CTE mismatch), diminishing the TSVs' mechanical influence on the surroundings. In summary, the stress induced in silicon by unfilled TSVs is mainly determined by the geometry of the hole, while for filled TSVs the mechanical properties of the metal also play a considerable role in determining the stress levels.

4.3.2. Analytic Solution for the Stress Around One TSV

A previous work [82] from Lu et al. has developed an analytical solution for the curve sketched in Fig. 4.5 for filled TSVs. Unfortunately, their solution and solving strategy cannot be applied to unfilled vias. The exact solution for such cases will be developed in this section.

Consider the equilibrium equation (3.29) in cylindrical coordinates as

$$\frac{\sigma_{rr}}{dr} + \frac{1}{r}(\sigma_{rr} - \sigma_{\phi\phi}) = -F \;, \tag{4.1}$$

and Hooke's Law with a thermal expansion (2.24) also adapted for cylindrical coordinates in axis-symmetric geometries as stated in [39]

$$\begin{bmatrix} \sigma_{rr} \\ \sigma_{\phi\phi} \\ \sigma_{zz} \\ \sigma_{r\phi} \\ \sigma_{rz} \\ \sigma_{\phi z} \end{bmatrix} = K \begin{bmatrix} 1-\nu & \nu & \nu & 0 & 0 & 0 \\ \nu & 1-\nu & \nu & 0 & 0 & 0 \\ \nu & \nu & 1-\nu & 0 & 0 & 0 \\ 0 & 0 & 0 & \nu & 0 & 0 \\ 0 & 0 & 0 & 0 & \nu & 0 \\ 0 & 0 & 0 & 0 & 0 & \nu \end{bmatrix} \begin{bmatrix} du_r/dr \\ u/r \\ du_z/dz \\ 0 \\ du_z/dz + du_r/dr \\ 0 \end{bmatrix} - \sigma_T \begin{bmatrix} 1 \\ 1 \\ 1 \end{bmatrix} \;, \tag{4.2}$$

$$K = \frac{E}{(1+\nu)(1-2\nu)}; \qquad \sigma_T = \frac{E\alpha\Delta T}{(1-\nu)} \;.$$

The problem domain is assumed to be a plate of a single material with an unconstrained hole in the middle and constrained borders as depicted in Fig. 4.6.

The plane strain approximation is imposed, thus the normal strain in z-direction vanishes and Hooke's law in (4.2) is simplified as

$$\begin{bmatrix} \sigma_{rr} \\ \sigma_{\phi\phi} \end{bmatrix} = K \begin{bmatrix} 1-\nu & \nu \\ \nu & 1-\nu \end{bmatrix} \begin{bmatrix} du_r/dr \\ u/r \end{bmatrix} - \sigma_T \begin{bmatrix} 1 \\ 1 \\ 1 \end{bmatrix} \;. \tag{4.3}$$

No body force is present in the structure, hence (4.2) becomes a homogeneous PDE with the solution in the displacement field given by

$$u(r) = Ar + \frac{B}{r} \;, \tag{4.4}$$

where A and B are integration constants. The unfilled via cross section is composed of more materials layers (two oxide layers and one metal layer), therefore Fig. 4.6 does not describe fully the original problem. However, the general solution is still useful.

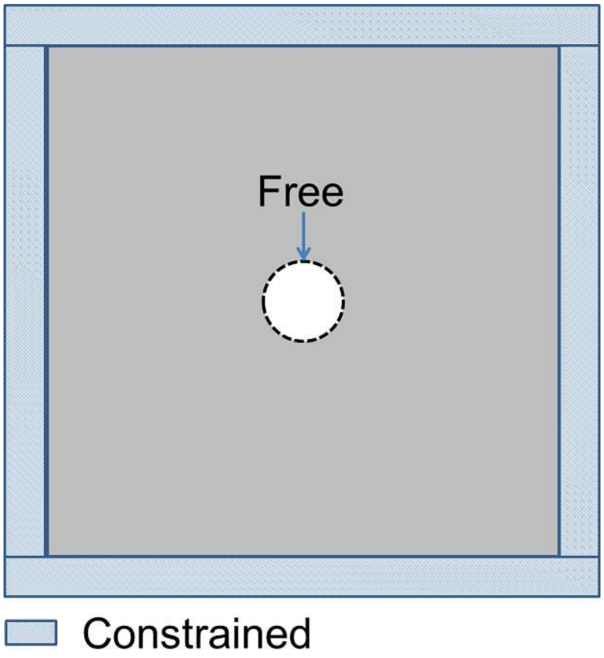

Figure 4.6.: Problem description of the stress created by unfilled TSVs due to thermal expansion.

The material properties manifest themselves only in the integration constants. Hence, the solution differs solely by constants among the materials as shown in Fig. 4.7.

The different constants can be obtained by ensuring stress and displacement continuity in the interfaces and, of course, by applying the boundary conditions of the problem as in (4.5), (4.6), and (4.7).

Displacement continuity

$$\begin{aligned} C_1 R_1 + \frac{C_2}{R_1} &= C_3 R_1 + \frac{C_4}{R_1}\,, \\ C_3 R_2 + \frac{C_4}{R_2} &= C_5 R_2 + \frac{C_6}{R_2}\,, \\ C_5 R_3 + \frac{C_6}{R_3} &= C_7 R_3 + \frac{C_8}{R_3}\,. \end{aligned} \tag{4.5}$$

Stress continuity

$$\begin{aligned} K_{oxide}\left[C_1+\frac{(2\nu-1)C_2}{R_1^2}\right] &= K_W\left[C_3+\frac{(2\nu-1)C_4}{R_1^2}\right] \ , \\ K_W\left[C_3+\frac{(2\nu-1)C_4}{R_2^2}\right] &= K_{oxide}\left[C_5+\frac{(2\nu-1)C_6}{R_2^2}\right] \ , \\ K_{oxide}\left[C_5+\frac{(2\nu-1)C_6}{R_3^2}\right] &= K_{Si}\left[C_7+\frac{(2\nu-1)C_8}{R_3^2}\right] \ . \end{aligned} \tag{4.6}$$

Boundary conditions

$$\begin{aligned} \sigma_{rr}(R_0) = K_{oxide}\left[C_1+\frac{(2\nu-1)C_2}{R_0^2}\right] &= 0 \ , \\ u(R_4) = C_7R_4+\frac{C_8}{R_4} &= 0 \ . \end{aligned} \tag{4.7}$$

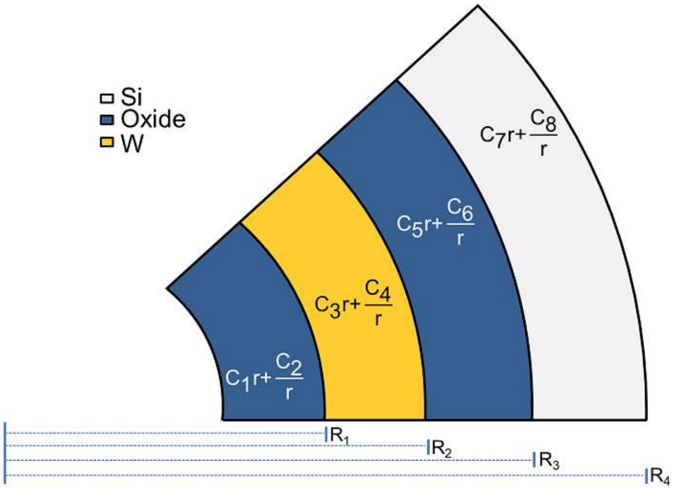

Figure 4.7.: Solution of the different materials. The solution form is kept, since the equilibrium equation must be satisfied in every material. The constants are solely determined by the material parameters and via geometry. They can be computed by imposing boundary conditions and interface conditions (continuous displacement and radial stress between the interfaces).

Although the full development of the analytical solution is feasible, it is very lengthy. A faster approach is to compute the constants directly with a linear solver or with the transfer matrix method.

An additional consideration can be included to simplify the solution. Since the domain dimensions are far larger than the stress spread zone, it is possible to consider the exact solution under the infinite plane approximation. In that situation the constant value C7 vanishes and one can calculate the displacement and stress in silicon for the standard unfilled TSV by

$$u_{Si} = \frac{-1.7759}{r} \,, \tag{4.8}$$

$$\sigma_{rr}^{Si} = \left[\left(\frac{E_{Si}(1-\nu)}{(1+\nu_{Si})(1-2\nu)} \right) \left(\frac{-1.7759}{r^2} \right) \right] - \frac{1.7759 E_{Si} \nu_{Si}}{r(1+\nu_{Si})(1-2\nu)} + \sigma_T \ , \ \textit{and} \tag{4.9}$$

$$\sigma_{\phi\phi}^{Si} = \left[\left(\frac{E_{Si} \nu_{Si}}{(1+\nu_{Si})(1-2\nu)} \right) \left(\frac{-1.7759}{r^2} \right) \right] - \frac{1.7759 E_{Si}(1-\nu)}{r(1+\nu_{Si})(1-2\nu)} + \sigma_T \ . \tag{4.10}$$

In Fig. 4.8 the displacement evolution in silicon along the radius of the TSV is shown in comparison with the exact solution given by (4.8) . One can notice that this approach also allows for the calculation of the exact solution for filled TSVs.

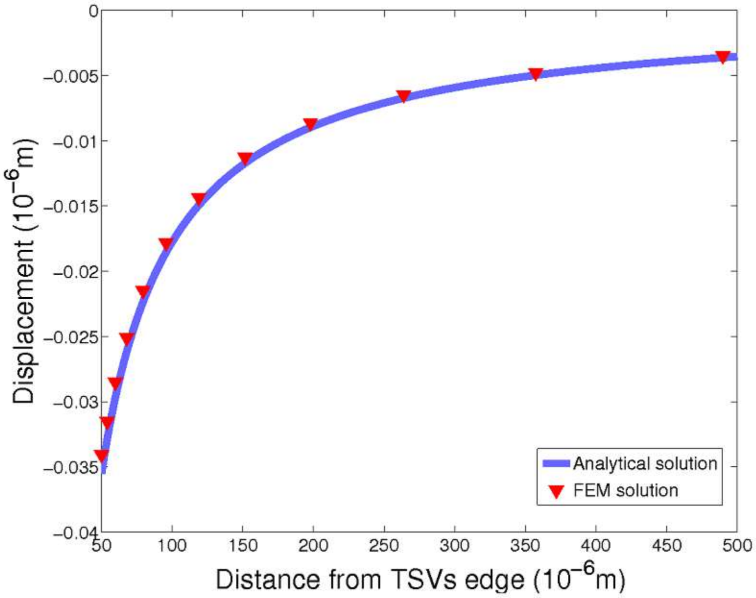

Figure 4.8.: Comparison between the FEM solution and the analytical solution described in this section.

4.3.3. Stress in a Group of TSVs

Although one isolated TSV is not very common in real devices, its analysis is extremely useful. The vias are usually arranged following a particular pattern, which causes an interaction between the stress fields around the TSVs. As an example consider an arrangement of TSVs as shown in Fig. 4.9. It is irrelevant if the via is filled or unfilled, since the stress around the TSV in both cases follows the same decaying law (proportional to the inverse of the distance), as was derived in (4.9) and is shown in Lu's solution [82].

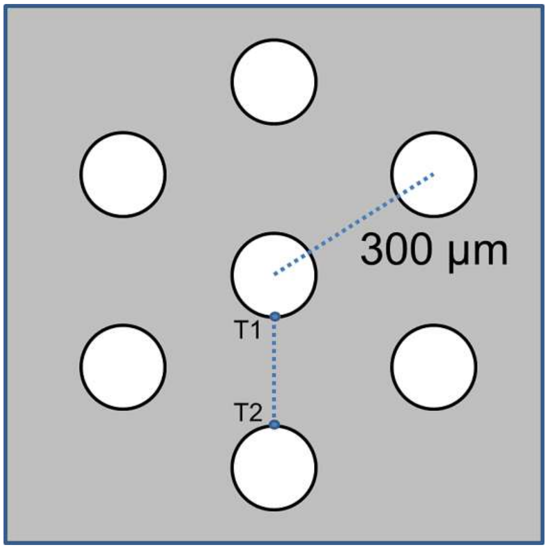

Figure 4.9.: A particular arrangement of 7 TSVs. The vias are equidistant (300μm) from each other.

2D simulations of the 7 TSVs were performed. The result enables the analysis of the stress field interaction between the TSVs as depicted in the von Mises plot of Fig. 4.10. One can note a peculiar pattern formed. Superposition of the individual stress fields of the TSVs leads to stress free regions in between them. Fig. 4.11 details the stress between the two TSVs along the line T1-T2 from Fig. 4.9 and it shows the superposition of the stress field of the two vias as described by (4.9).

Actually, it is possible to use the stress solution for one TSV and the superposition principle to determine the localization of the stress-free zones. Consider the triangle ABC of Fig. 4.10, where the stress inside this triangle is determined only by the TSVs at each of its vertices. The influence of the other TSVs in the arrangement is negligible because of the large distance to the triangle zone. Therefore the localization of the stress minimum value is given by the solution of the problem posed by

$$\min_{r \in \Delta ABC} = \sigma^{A}_{Mises} + \sigma^{B}_{Mises} + \sigma^{C}_{Mises} \ . \tag{4.11}$$

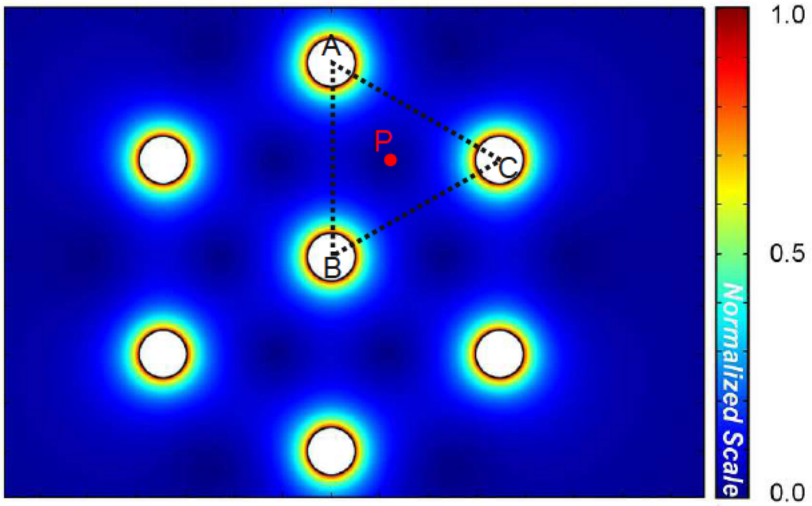

Figure 4.10.: Von Mises stress of the 7 TSVs pattern. The stress superposition between the TSVs creates stress-free spots. The TSVs' placement can be chosen to minimize the stress impact in silicon.

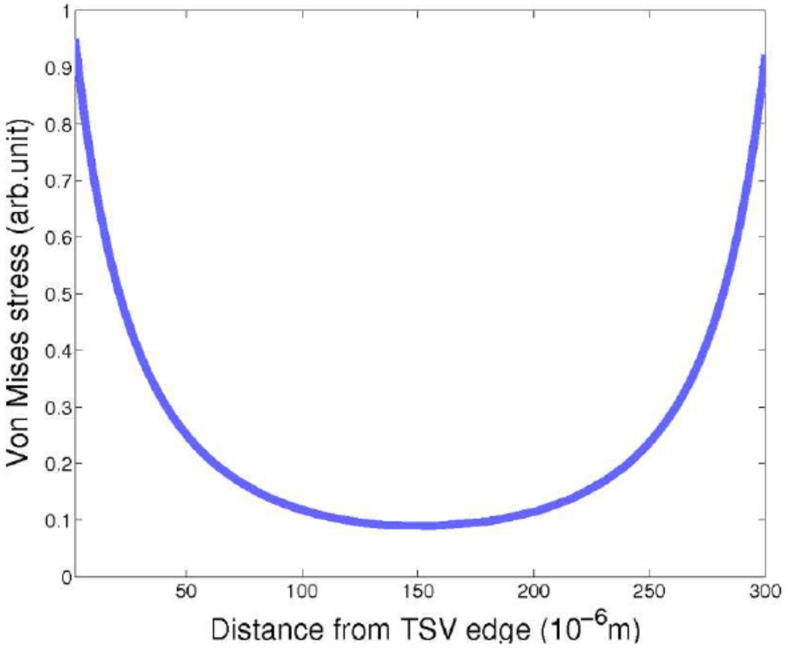

Figure 4.11.: Von Mises stress between two TSVs. The characteristic stress curve of each TSV is superimposed to its neighbor, creating this particular pattern.

The superscripts A, B, and C refer to the TSVs on the triangle vertices of Fig. 4.10. In this situation, σ_{rr} and $\sigma_{\phi\phi}$ of each TSV is given by (4.9) and (4.10) translated according to the origin of the coordinate system used for the minimization problem in the triangle. The point obtained for this particular arrangement is indicated in Fig. 4.10. It is located 85μm in the x-direction and 150μm in the y-direction away from the center of the TSV centered in Vertex B.

In fact, this point is the geometric center of the triangle ABC, which in an equilateral triangle is equally far from each vertex. Therefore, it is the point inside the triangle least influenced by the stress field of the three TSVs. This means that it is possible to determine the localization of each minimum in this arrangement of TSVs just by determining the geometric center of each triangle. For any other arrangement a new minimization problem must be formulated as was done in (4.11).

The TSVs arrangement can be used to control the stress around the vias. It can be applied to maximize the area available for devices as well as to increase the mechanical stability of the entire structure. The solution (4.8) is, in principle, only valid to calculate the stress around the middle of the via, however it can also be used as an estimate of the stress in the top and bottom of the TSV structure, as depicted in Fig. 4.12. Therefore, the procedure described here can be easily applied to the placement of TSVs, with the advantage that the development of the analytic solution gives speed and simplicity to the process.

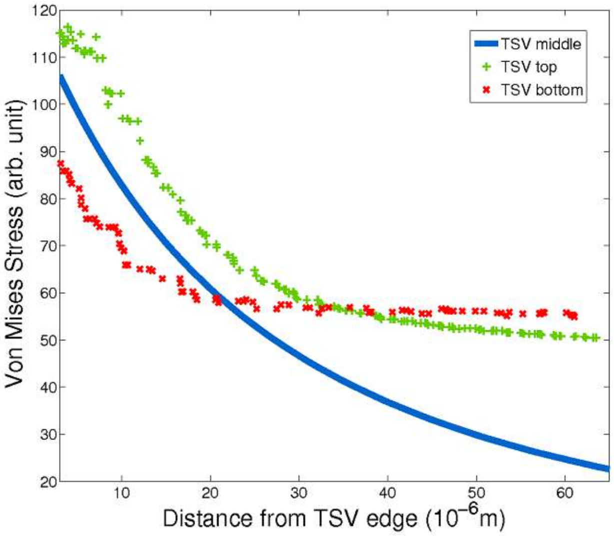

Figure 4.12.: Comparison between the stress along the radial direction at the top and bottom of the TSV with the stress in the middle (analytical solution). For points close to the TSV edges, the analytical solution provides a fair approximation. For points further from the TSV edge (20um), it can still be used as a lower bound estimate for the stress.

4.3.4. Summary and Conclusion

Within this section, FEM elastic thermal-mechanical simulations were performed with the purpose of analysing the stress behavior along the via and in the surrounding silicon. Critical stress points on the metal layer at the top and bottom of the TSV were identified by means of FEM simulations. It was also shown how the stress develops in the bulk Si, and it was demonstrated that the stress drops in proportion to the squared distance from the via border. A method for calculating the exact stress in the middle region of an unfilled TSV was also presented. The results were successfully used to predict the points of minimal stress in the arrangement of TSVs, explaining how the spacing and the pattern in which the TSVs are laid out support high mechanical stability and reliability of the entire structure. The same procedure can be used for other via geometries and via placements in order to study the mechanical stability.

5. Stress Inside TSVs

The structure of the TSV itself is exposed to instability caused by stress. Within this chapter the situations which arise from processing or device operation and which can be dangerous for the TSV are discussed. Local features' effects, such as Bosch scallops, are investigated as well as mechanical effects during wafer handling. Particular attention is paid to thin films, especially because of the lack of available information for such systems. A deep look into the stress relaxation of metal films is presented and a scheme to couple FEM simulation with relaxation models is provided.

5.1. Stress in Thin Films of TSVs

Solid thin films are widely used in semiconductor technology as metal lines, barriers, glues, passivation layers as well as active materials for microelectromechanical systems (MEMS) [38]. TSVs have thin films implemented along the entire structure. In fact, in unfilled TSVs the via is made uniquely of very thin layers of multiple materials.

Thin films are usually defined as material layers with a thickness ranging from fractions of nanometers up to hundreds of micrometers. The small thickness gives the material a different behavior in comparison to its properties in bulk dimensions, especially regarding mechanical characteristics. Thin layers respond differently to stress and their fabrication generates internal forces which are high enough to potentially damage the TSV structure.

In semiconductor technology a film is usually attached to a substrate which can be hundreds of times thicker than the film itself, thereby limiting its deformation. In such a system (substrate-film) stress can generate due to various phenomena. In 1988, Doerner and Nix reviewed the main mechanisms for stress formation in thin films [86]. Freund summarized them in a comprehensive list [38], displayed in Table 5.1.

Growth stress (residual stress) is understood by Freund as the stress which arises during film fabrication, and external stress (extrinsic stress) is any stress which is generated due to a force which originates after film deposition.

The list of stress sources is quite vast and it is impossible to include a comprehensive study of each item in this work. In addition, they are not all pertinent to the TSV technology. Hence, this work presents three different studies of relevant stress issues in TSVs related to thin films. The first is discussed in the following section and describes

Table 5.1.: Stress sources identified by Doener and Nix.

Growth stress	**Extrinsic stress**
Surface and/or interface stress	Temperature change
Cluster coalescence	Piezoelectric or electrostrictive response
Grain growth	Electrostatic forces
Vacancy annihilation	Gravitational or inertial forces
Grain boundary relaxation	Compositional segregation
Shrinkage of grain boundary voids	Electromigration
Incorporation of impurities	Chemical reactions
Phase transformations and precipitation	Stress induced phase transformations
Moisture adsorption or desorption	Plastic or creep deformation
Epitaxy	
Structural damage (deposition process)	

the manner in which the final build-up of intrinsic stress in the metal layer affects the mechanics of the TSV structure. The second topic is also discussed in this chapter and details how some external stress sources, such as thermal variation and wafer handling, can be dangerous for the vias. The last study demands a microstructural view of the thin film materials and must be handled differently; therefore it is left to the next chapter.

5.2. Influence of Stress in Metal Layers on TSVs

In this section only the standard unfilled TSV is considered, as defined in Chapter 4, since there is no relevant thin metal film in filled TSVs. The point of interest is the conduction layer along the wall of the unfilled TSV. Any mechanical instability in this layer can lead to cracks which, after some time, could cause a complete failure of the TSV.

Krauss et al. [85] performed X-Ray Diffraction (XRD) stress measurements on the wall of a standard open TSV structure, but the specific via's geometry permitted only a measurement of the top 10μm. A full plate sample with an identical layer profile is then used to support stress characterization depicted in Fig. 5.1. The purpose of the full plate is to ease the measurement process and to improve its precision. Additionally, it represents the best estimate for the stress in the middle of the via, since it is not feasible to measure the stress at the full depth of the TSV.

However, the stress on the TSV tungsten film was found to be smaller than on the full-plate samples. At the TSV's wall scallops were observed, which were caused by the Bosch process, as depicted in Fig. 5.2. The presence of scallops along the TSV walls and the lack of them in the full-plate sample suggests that they might be the reason behind the observed stress reduction.

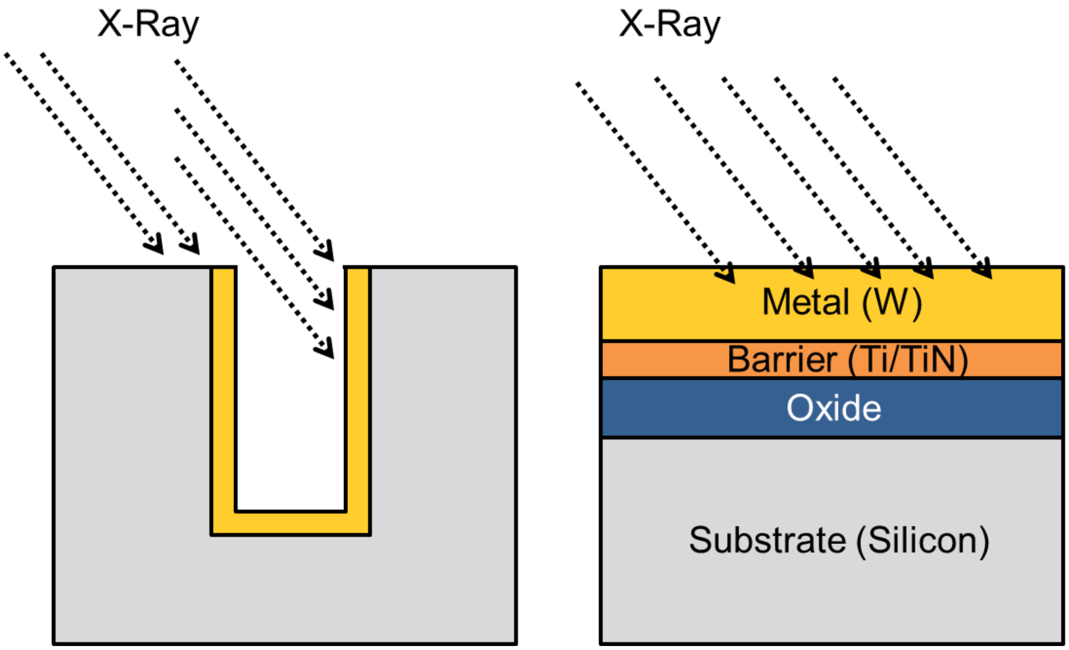

Figure 5.1.: A TSV (left) and a full-plate (right) sample during X-Ray measurements. The TSV geometry hinders the X-Ray reach, while a full-plate sample with the same layer profile is used to evaluate the stress in the metal.

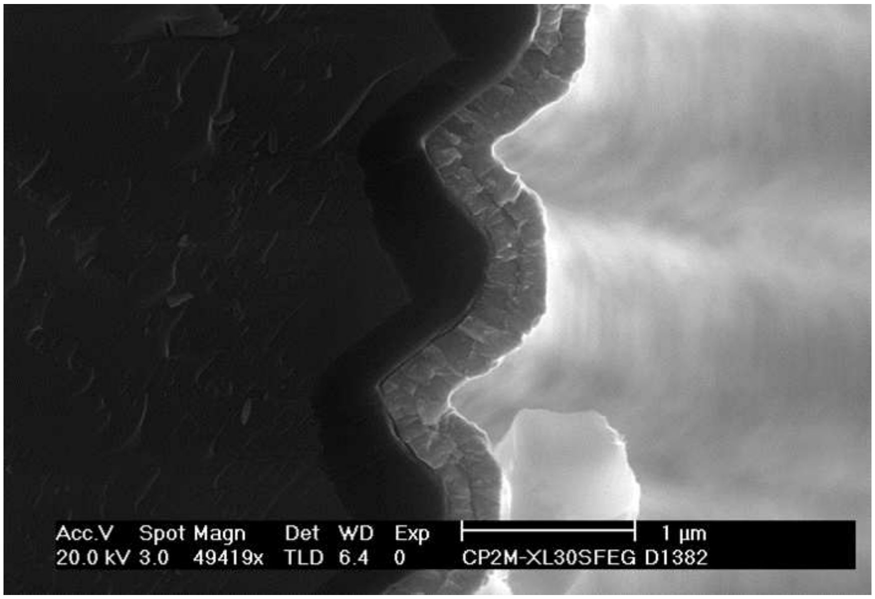

Figure 5.2.: Two-dimensional cross section of the TSV. The Bosch scallops are shown in detail.

To explain the stress difference in the samples, the effects of the sidewall scallops on the vias were studied. It is hypothesized that the scallops' geometry causes the stress reduction. This same interpretation was also mentioned by Krauss et al. Furthermore, a possible weak adhesion of the scallops' bottom due to shadowing effects was likewise investigated. This phenomenon can lead to stress relaxation and can also further explain the difference between the measurements.

A second structure with a double stack layer of W/TiN is considered in Krauss's work. It is probably employed in order to increase the TSV's electrical conductivity without any degradation of stress stability. This double stack structure is also considered here, particularly due to the availability of experimental data for comparison.

To evaluate both hypotheses, mechanical simulations were performed on two structures as depicted in Fig. 5.3.

For the simulation, an initial tensile residual stress was assumed on the tungsten layers, as measured on the full-plate samples [85]. The material interfaces of the scallops' bottom were treated as a contact surface, thus the weak adhesion was properly considered. The solution of the resulting surface problem is computed by a combination of the Lagrange and the penalty method as described by Faraji [87].

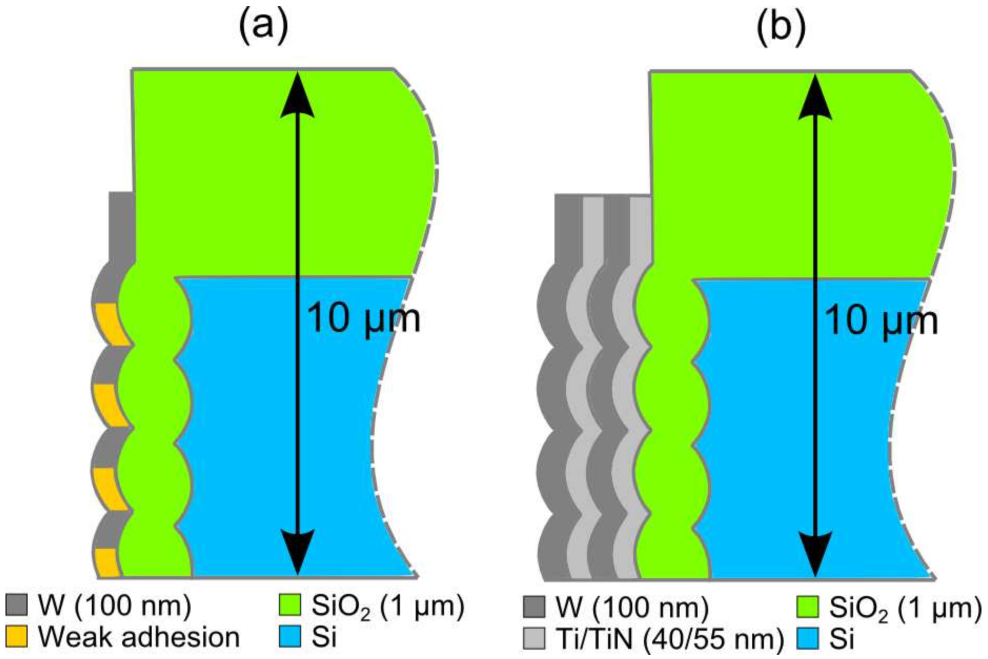

Figure 5.3.: Schematic of the single (a) and double (b) stack structures considered for the simulation.

5.2.1. Scallop Geometry

An accurate evaluation of the hypothesis relies on a good description of the scallop's geometric shape. A parabolic-like shape is suggested, as depicted on the previous cross sectional TSV images in Fig. 5.2. The height and width of each scallop is estimated to be 2μm and 0.5μm respectively.

The scallops' geometry can be obtained using level set based Bosch process simulations. However, to understand their influence on the TSV, different combinations of height and width were studied. In order to study various scallop shapes, level set simulations are an unfeasible approach, because the simulations can take a considerable amount of time and the simulation results are not easily adaptable to the finite element tools used in this work. Thus, an alternative solution was applied. A single Bosch simulation was carried out, as shown in Fig. 5.4, and based on it an entire set of structures was manually constructed for several dimensional combinations. The scallop shape is then fitted to rational quadratic Bézier curves [88], for which the general form is given by

$$B(t) = \frac{(1-t)^2 P_1 W_1 + 2t(1-t) P_2 W_2 + t^2 P_3 W_3}{(1-t)^2 W_1 + 2t(1-t) W_2 + t^2 W_3}\,, \tag{5.1}$$

where P1, P2, and P3 are control points as depicted in Fig. 5.5. W1, W2, and W3 are weights used for curvature control corresponding to each point of the curve (P1, P2, and P3, respectively), and t is the curvature parameter which varies between 0 and 1. Fig. 5.4 depicts a visual comparison between the Bézier curve description of the scallop, the Bosch simulation, and the observed scallop along a processed TSV sidewall.

Two Bézier curves were used to form a scallop, as depicted in Fig. 5.5. For each scallop, the curvature, size, and width were controlled by an appropriate choice of weights and points in relation to both curves, following the rules below:

- P1 and P6 must be on the intended TSV wall (without scallops) and the distance between them defines a scallop's width.
- The distance between P1 and P2 defines the maximum scallop's height which is reached at the middle of the scallop's width.
- P1 and P2 are placed on the same side of the scallop while P5 and P6 are placed on the opposite side of the scallop.
- The weights W1, W3, W4, and W6 are given the value 1. The weights W2 and W5 have the same value (which controls the scallop's curvature), W2=W5=W. It was chosen W=1/3.

Although this approach describes the scallops' parabolic shape, the junction between them is smoother than the Bézier curve can represent. This could lead to singularities during simulation, resulting in high stress at the points where two scallops meet.

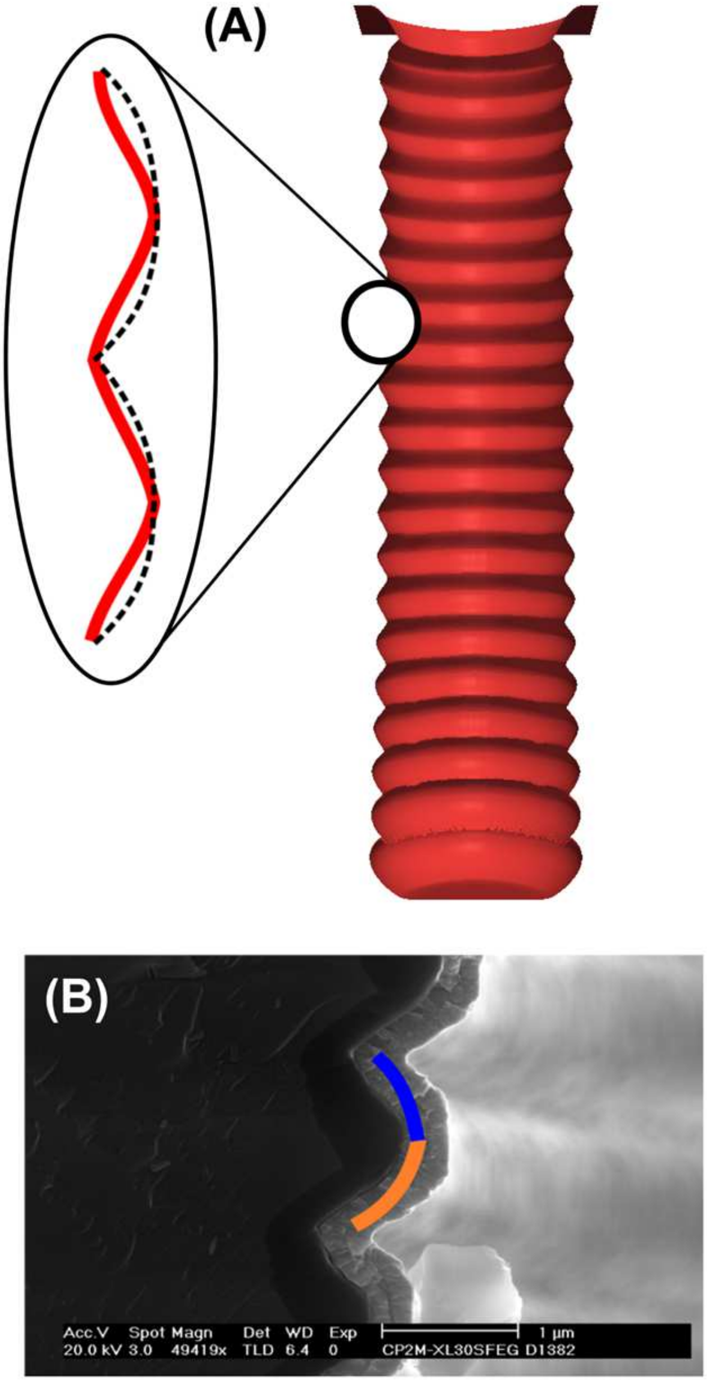

Figure 5.4.: Comparison between the Bézier curve description of the scallops to the Bosch process simulation (a) and the fabricated scallop (b). Bézier curves create sharp points between the scallops, which could lead to unrealistic stress build-up at these meeting points during simulation.

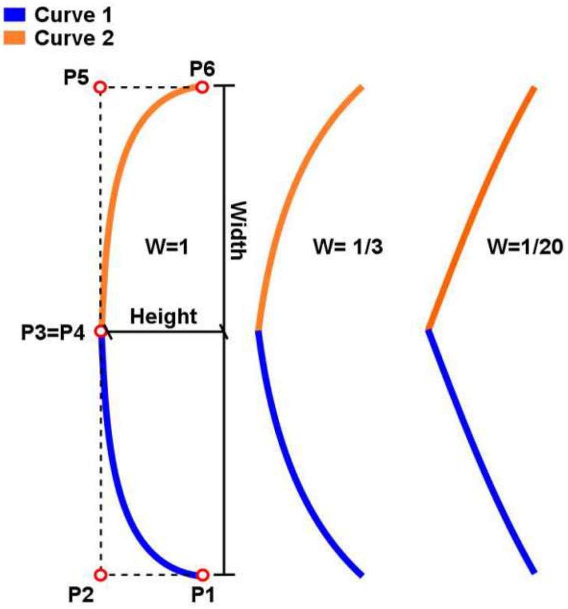

Figure 5.5.: Scallop shape approximation by two Bézier curves. The curvature, height, and width are controlled by the weights.

5.2.2. Meshing and Boundary Conditions

The simulation of the entire structure, as depicted in Fig. 4.1, is computationally unfeasible in the presence of a large number of scallops and contact surfaces. Consequently, the simulation domain is reduced by taking into consideration the aforementioned experimental constraint (10μm from the top of the TSV).

As boundary conditions, it was assumed that the extreme right side of the structure is fixed, while the TSV's inner side is free to move as well as the top. The bottom boundary has a more complicated scenario, because a proper condition is unknown in the adapted domain from Fig. 5.3. To handle this situation a symmetric boundary condition was employed. Although this is not true, when the entire structure is considered, it is a good approximation for the geometry in the vicinity of the simulation domain. Additionally, it reduces any possible boundary effect which could impact the solution. The simulation was performed assuming symmetry around the central TSV axis in order to capture the cylindrical shape of the TSV.

The scallop shape and the contact surfaces demand a fine mesh to prevent numerical convergence issues, as depicted in Fig. 5.6. As a result the mesh is rather dense near the scallops, leading to many mesh points and elements for a relatively small structure. Triangular elements were used, because they showed a better adaptability in this structure, when compared to quadrilateral elements. The mesh of the single stack structure has 12466 points and 24635 triangles, while the double stack structure has 17945 points and 35461 triangles.

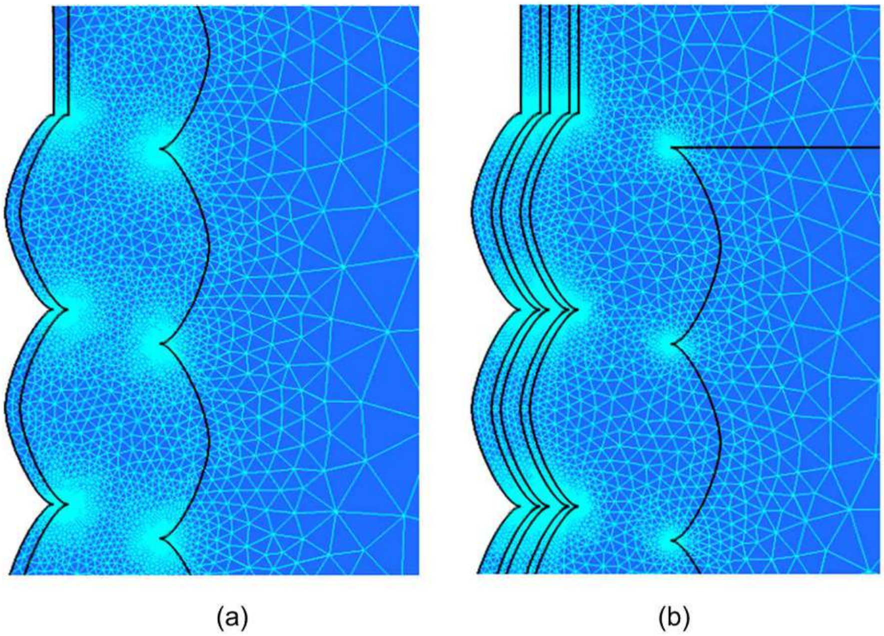

Figure 5.6.: Mesh details around the scallops for the single (a) and double (b) stack structure.

5.2.3. Simulation Results

The first goal of this study was to understand the reasons for the stress discrepancy between the TSV and the full-plate samples. Therefore, the following configurations were considered for simulation: TSV without scallops, TSV with scallops, and TSV with weak adhesion. The first case was performed to control the hypothesis, whereas the other two cases were used for an evaluation of each particular feature on stress. The geometry of the scallops has been identified as the main cause for stress reduction inside the tungsten layer, as shown in Fig. 5.7. Although the weak adhesion has introduced some relaxation (∼17%), it superimposes to a stress state already reduced by the geometry. Moreover, the in-plane stress on tungsten is not equal in every direction in the presence of scallops. Krauss et al. were unaware of this fact during their measurements and assumed an in-plane equibiaxial condition for the stress [85]. Nevertheless, this possibility is discussed in their work. Consequently, the reported stress by Krauss et al. does not fully characterize the state in the tungsten layer, but rather the average normal stress in the vertical direction, according to their described experimental setup.

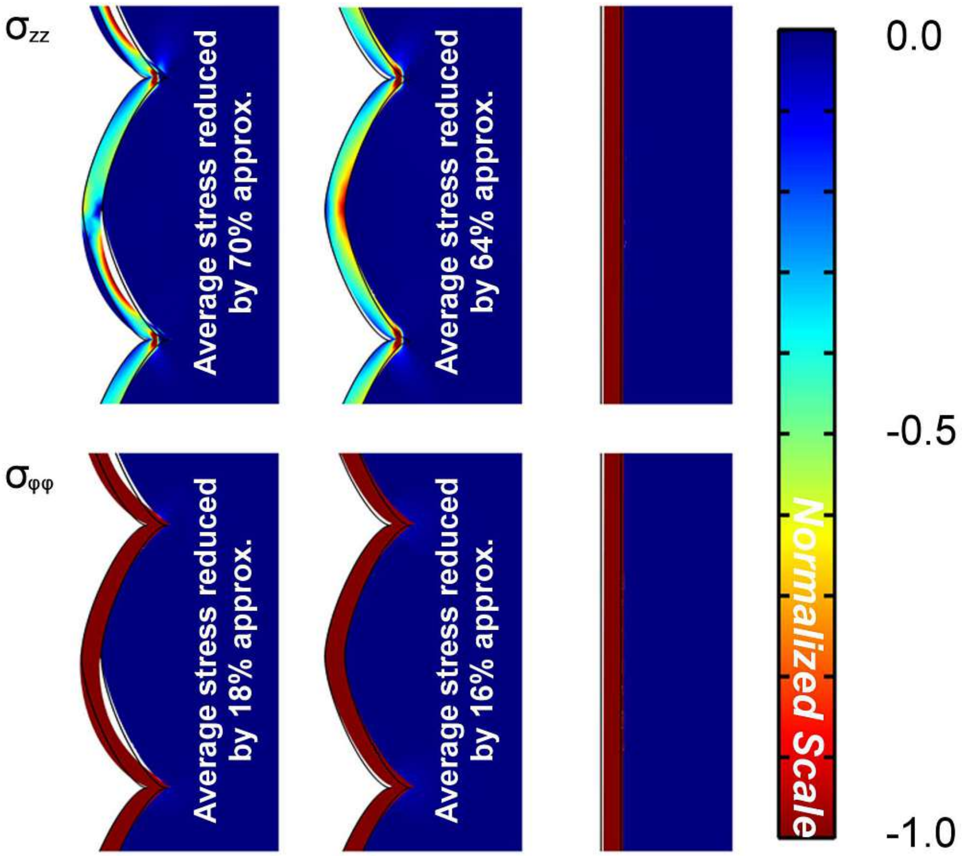

Figure 5.7.: Stress distribution along the TSV in the vertical (top) and tangential direction (bottom) considering vias with weak adhesion (left), no weak adhession (middle) and without scallops (right). The stress is strongly reduced in the vertical direction, mainly due to the scalloped geometry. The weak adhesion induces a small reduction, but it is not the main mechanism. Along the tangential direction, the scalloped geometry is not so evident, hence the stress reduction is very small.

The double stack structure was simulated under the same conditions as the single stack, except that the weak adhesion case was not considered, as shown in Fig. 5.8. Since the equibiaxial stress assumption is not valid in the presence of scallops, the simulated and experimental stress results have not been compared. Instead, the strain was compared, which is a direct measure and free of any assumptions.

The average simulated strain of 0.00169 in the vertical direction was in reasonable agreement with the measured strain of 0.00111 [85] for the tungsten layer. The intrinsic stress on the Ti/TiN layers was ignored due to the lack of experimental data. However, simulations considering a compressive stress in the Ti/TiN layers resulted in an average strain of 0.00127 in the tungsten layer. Hence, the absence of the intrinsic stress on Ti/TiN can justify the difference between simulated and observed values.

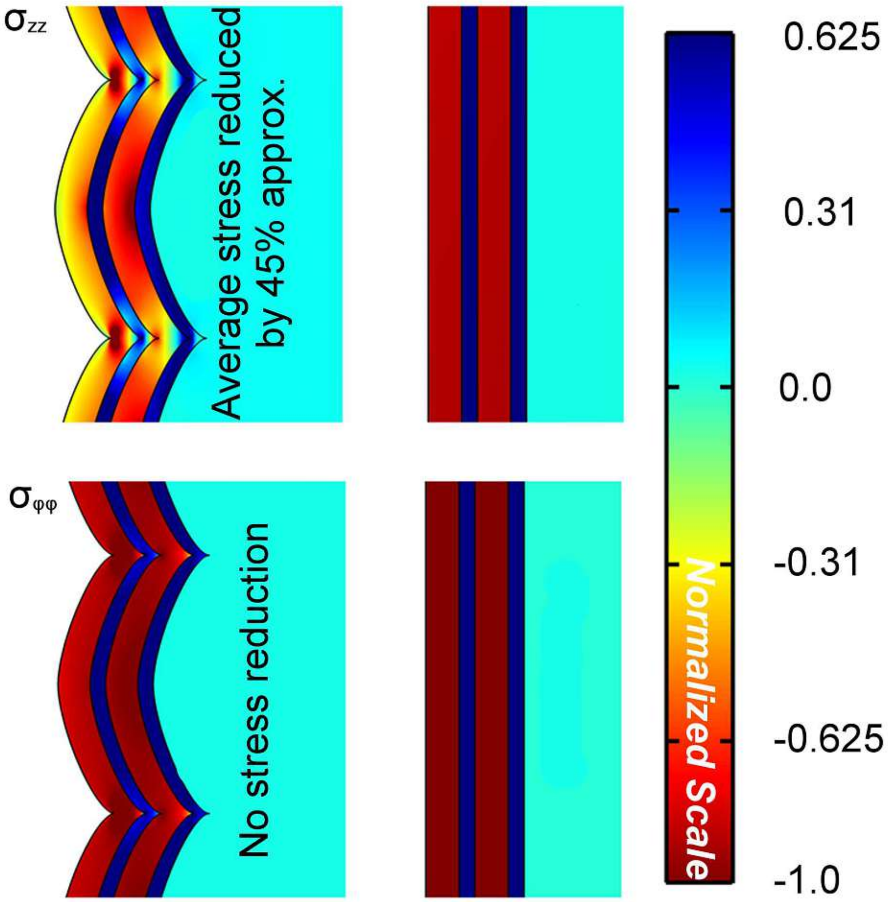

Figure 5.8.: The same behavior for the stress is found in double stack structures. However, the reduction due to the scalloped sidewall is slightly smaller when compared to single stack TSVs.

The rigidity characteristic of the scallops in the vertical direction modifies the stress distribution on TSV films. The tensile stress induces an inward movement in the region of valleys between scallops, shown in Fig. 5.9. This leads to a relief of the stress along the via, since the material finds a favorable point to stretch. Consequently, the average normal stress in the vertical direction in tungsten is reduced, causing the difference between TSV and full-plate samples. However, in the tangential direction there is almost no stress reduction. Along this axis the geometry is not modified by the scallops. Therefore, the initial load faces a similar scenario in the presence or absence of scallops.

Additional insight concerning reliability is gathered from an analysis of the von Mises stress. The mean values for structures with and without scallops are very similar and no significant difference was detected. Hence, the full-plate sample measurements

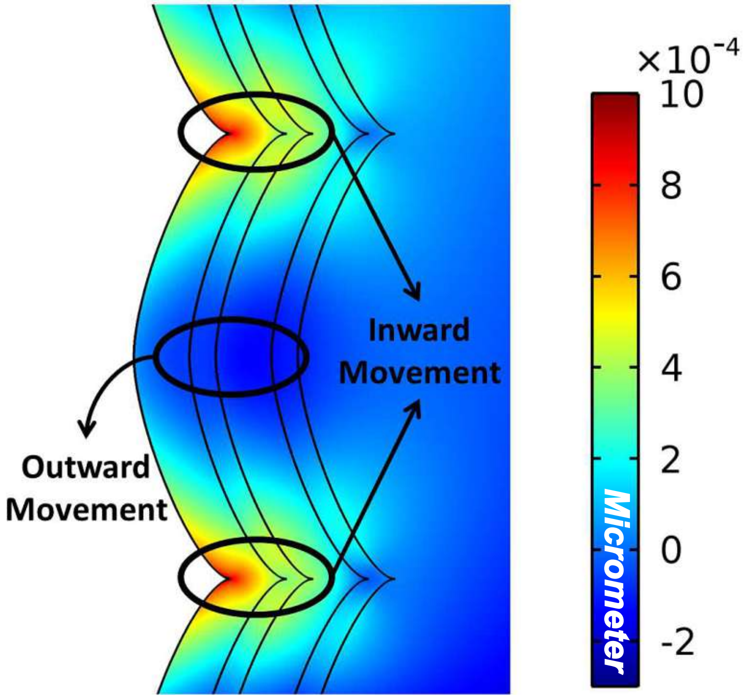

Figure 5.9.: Displacement in the radial direction. The scallop creates points which ease the movement of the metal, relaxing the overall stress in the metal layer.

could be used safely to determine the average von Mises stress. However, the mean value of the von Mises stress did not suffice when the scallops were present due to the modified stress distribution. Fig. 5.10 outlines the accumulation stress points. The von Mises stress can reach peaks of stress up to 3 times higher than those experienced on full-plate samples. However, such high values could be the result of the sharp transition between the Bézier curves used to represent the scallops (singularity points). Even if the sharp transitions, observed with Bézier curves, were removed, there is still a pinched transition region between scallops. There, points of pinch-off are a region of potential failure, as increased stress could lead to a fracture in the metal.

Regarding scallop dimensions, the stress magnitude behavior depends on the scallops height and width, as shown in Fig. 5.11. As the height increases, the stress increases very rapidly until a peak is reached, then it drops slowly toward a saturation value. For small heights most of the scallop still retains its flat geometry, impeding material expansion and leading to an increased stress. This scenario persists until the scallop reaches a height which favors the curvy geometry and material expansion (flat characteristic is no longer dominant), resulting in stress relaxation. The peak stress in Fig. 5.11 is defined by this change in the scallop geometry. As the scallops' widths are increased, the peaks broaden with a linear dependence, both in height and width directions. This peak movement is a consequence of the fact that wide scallops need higher heights to lose their flat behavior.

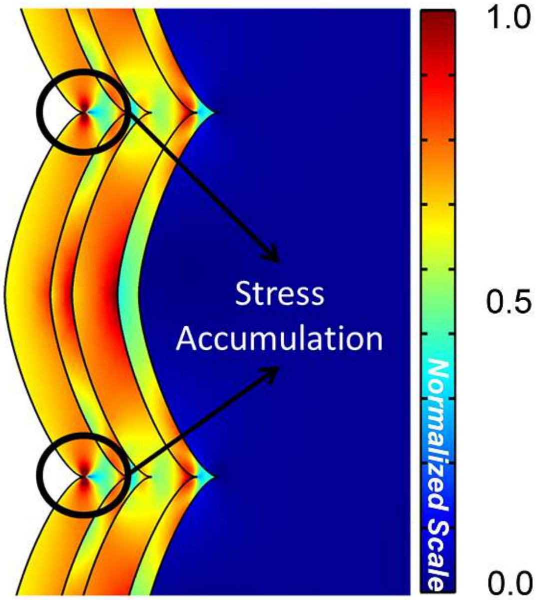

Figure 5.10.: Points of high stress in the scallops. Although there is an overall reduction of the stress in the metal layers, the scallops create points of stress accumulation, which can easily surpass the average layer stress.

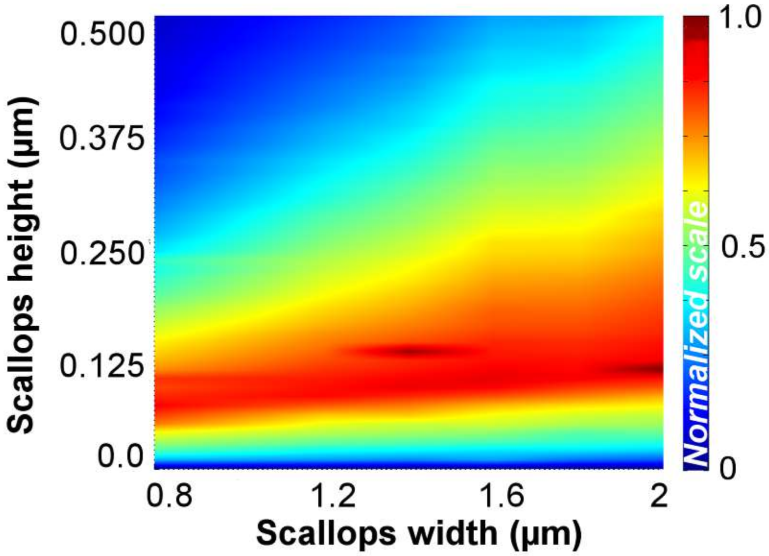

Figure 5.11.: Maximum von Mises stress variation dependence on the height and width of the TSV sidewall scallops.

5.2.4. Summary and Conclusion

Effects of Bosch scallops on stress reduction in metal layers of an open TSV technology were studied. Two possibilities were evaluated for an explanation of the phenomenon, including a weak adhesion of the scallops' bottom and the geometry of the scallops themselves. The latter causes most of the stress reduction, while weak adhesion is only a secondary mechanism. The manner in which the scallop geometry modifies the stress was described. Additionally, valleys between scallops were identified as potential failure regions due to increased stress in pinch-off sites. It was also shown that the equibiaxial stress assumption on the via walls in the presence of scallops is invalid. This information is vital for the proper evaluation of the simulation and experimental results. Finally, the simulations have shown to be consistent with experimental data, validating the setup for further studies.

5.3. Impact of Wafer Bow in TSVs

This section mainly deals with a different scenario, although the context of device processing and its influence on TSV performance is still present. The central purpose of this section is to understand how the handling of the wafer on a macroscale (millimeters) can affect the stress in the TSV. For that examination one should understand the conditions in which a wafer is found after TSV fabrication, more specifically after thin film deposition.

Film depositions usually modify the wafer shape. They are generally performed at several degrees above room temperature. At deposition temperature the material conforms to the substrate and an intrinsic stress arises as result of several processes during film formation, as described in Table 5.1.

After deposition the wafer is cooled down, but the film and the substrate contract at different speeds, due to the difference in the coefficient of thermal expansion (CTE mismatch). The variation of temperature creates stress in the materials, which increases the intrinsic stress. In order to accommodate these additional stress effects and reach a stable state, the system will bow itself up or down, depending on whether the resultant stress is positive or negative as shown in Fig. 5.12.

G.G. Stoney in 1909 developed an elegant method to determine, from the wafer curvature, the stress state of the film as in [89]

$$\sigma_f = \frac{M_s h_s^2}{6h_f}\frac{1}{R}, \tag{5.2}$$

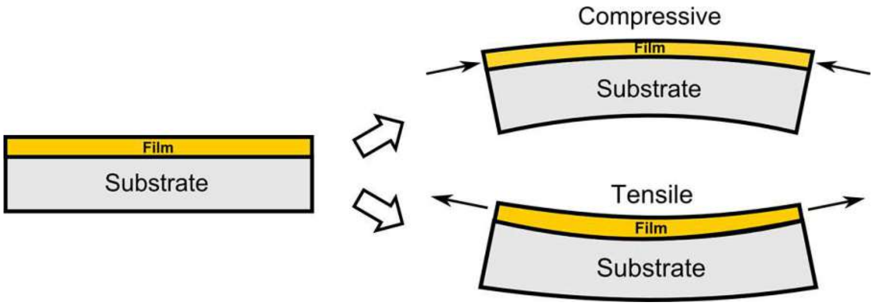

Figure 5.12.: Wafer bow due to film deposition. The curvature depends if the film stress is tensile (positive) or compressive (negative).

where σ_f is the average stress on the plane of the film, M_s is the biaxial elastic modulus of the substrate, h_s is the substrate thickness, h_f is the film thickness, and $1/R$ is the system curvature.

At the time Stoney made strict constraints which were removed, as film deposition studies progressed by several works which included more sophisticated systems and multiple layered films [89]. This work does not intend to extensively discuss such models, but instead to provide a brief explanation for wafer bowing.

5.3.1. Simulation of "Unbow" Wafer Movements

A curved wafer is a common occurrence during semiconductor processing and TSVs are susceptible to its effects, especially in cases which disturb the bowed stable state. For instance, during handling the wafer can be forced to a flat state with a machine chuck for further processing or transportation. In such scenarios a question immediately arises: would a flattening process cause mechanical instability in the TSVs? In order to find an answer, imagine that a wafer bowed 3μm negatively is forced flat by an external force, as depicted in Fig. 5.13.

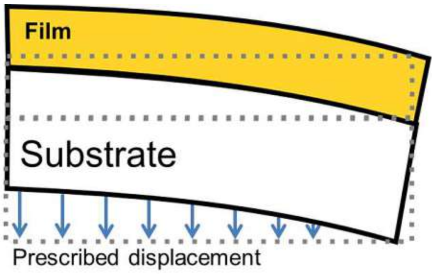

Figure 5.13.: A wafer forced to unbow during handling or processing.

To assess the impact of the flattening process, mechanical FEM simulations were performed. The simulation setup in this case is more challenging, because of the scale difference between the considered structures. A wafer has a diameter of up to 300mm while a standard TSV radius measures in the range of 100μm. The difference in length scales creates several complications for the simulation regarding meshing, numerical stability, and computing time.

A different approach is required in order to create a manageable simulation environment. The problem was treated in a hierarchical manner, where the simulation starts with a domain in a length scale comparable to the wafer diameter and is reduced, until the length scale of only one TSV is reached. A schematic of the adopted strategy is depicted in Fig. 5.14.

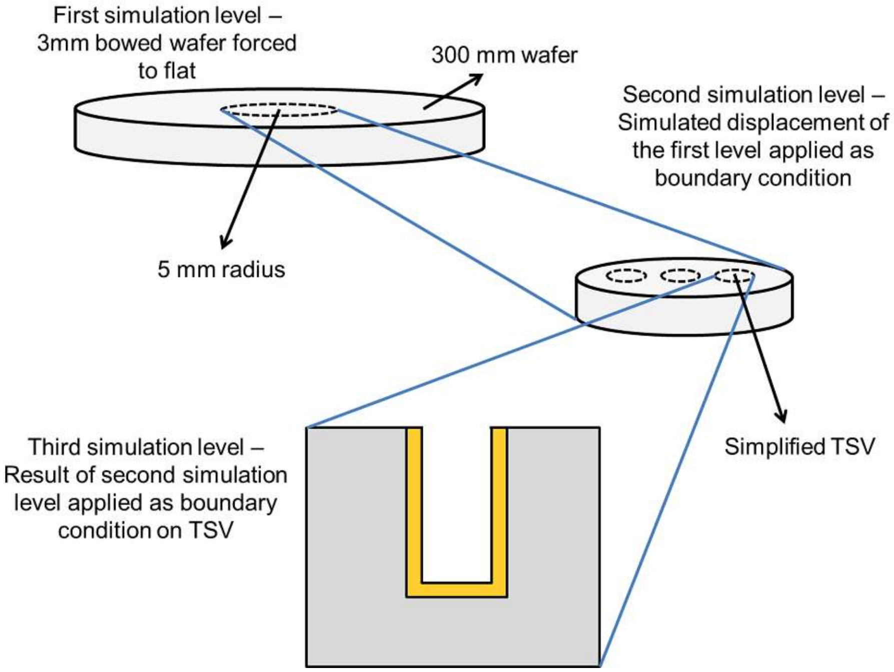

Figure 5.14.: Schematic of the multilevel approach for a simulation of large scale effects in the TSV.

At each step simulation level a simulation is required and the result is passed as a boundary condition to the next level. For example, the simulation starts with the flattening process of the entire wafer. At this point no TSVs are present in the domain, only the wafer is considered. In the next step the domain is reduced to a radius of 5mm from the wafer center. The TSVs are already present in a simplified manner, they are represented with holes in the silicon without any additional thin material layers. The computed displacement of the previous step is then applied as a boundary condition, forcing the solution to match at the domains' intersection. Finally, the domain reduction process is applied again to a single TSV. All material layers are present in this last simulation, where the boundary conditions are again computed using the displacement calculated at the previous simulation level.

This multilevel approach allows for the treatment of features on domains with very different scales. The complexity of the structures are included gradually, which reduces the computational cost of including all features at all simulation domains. The weakness of this technique lies in the boundary conditions of the lower levels, since their quality is limited by the solution of the upper levels. Therefore, a better refinement of the mesh of the domains in the respective lower levels is needed to obtain reliable results. Additionally, domain reductions of several orders of magnitude create numerical instability, because the mesh might not be fine enough to resolve very small domains. For example, a reduction from the wafer level directly to the TSV level would be a problem, since it would be necessary for a mesh element located in the region of a TSV to resolve the detailed TSV region, increasing drastically the computational requirements. The multilevel simulation strategy described here can also be seen as a special case of domain decomposition methods [90].

The result of the simulation for the last level of the filled TSV is depicted in Fig. 5.15, while the results from all simulation levels for an unfilled TSV are shown in Fig. 5.16. Measured intrinsic stress is considered on the film layers at the TSV level (last simulation). The stress at the TSV bottom of the unfilled via is very high, especially at the corners. The structure at this region acts like a lever and the stress generated by the "unbow" motion is magnified, producing potential failure spots on the TSV. Filled TSVs are better supported in this situation. The metal inside the cavity hinders the lever-like movement, increasing the mechanical stability of the structure against wafer handling situations.

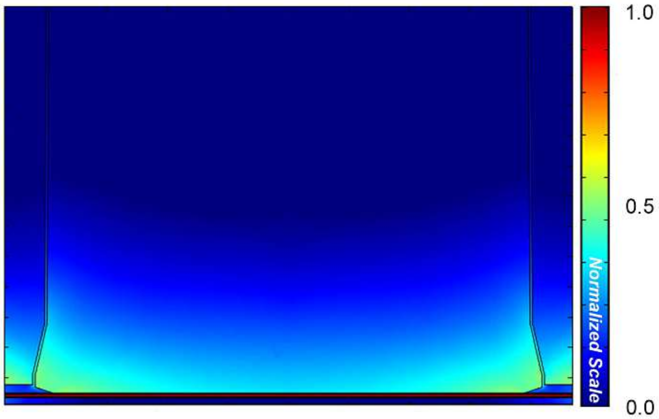

Figure 5.15.: Result of the last simulation level of a multilevel simulation of a filled TSV. The material inside the cavity provides better support against forces at the bottom of the TSV.

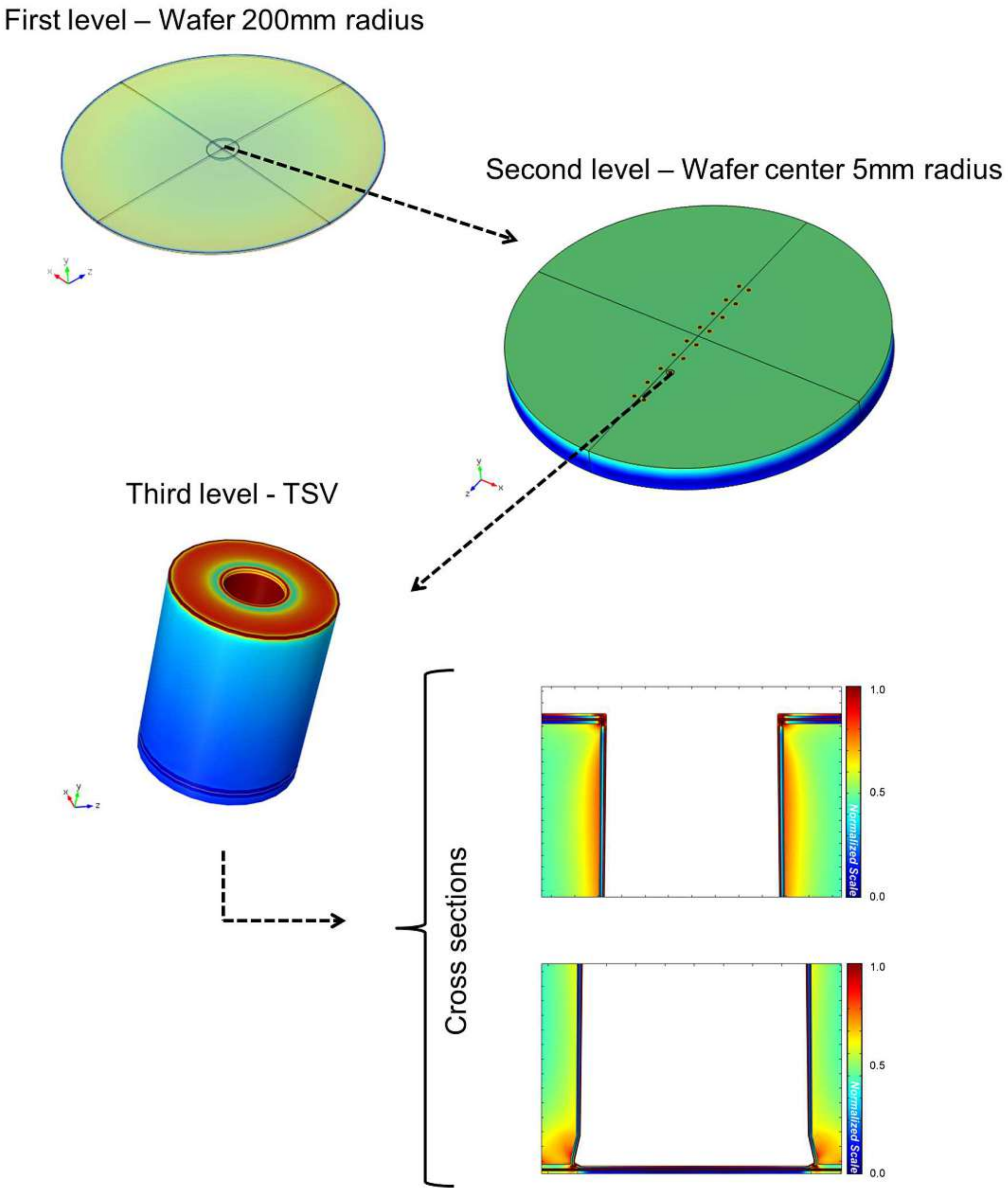

Figure 5.16.: Simulation of the effects of a forced unbow on the TSV. In the first level, no TSV is considered. For the second level the vias are treated as regular holes in the silicon. Only at the last level the TSV is considered in full detail. The unbow movement is particularly dangerous for the bottom and top corners of the via.

5.3.2. Summary and Conclusion

The impact of “unbow” movements due to handling was analyzed in this section. Such scenarios are especially dangerous for unfilled TSVs, because of the lever-like configuration at the bottom of the structure. Filled vias have a better support since there are no open surfaces. A methodology for dealing with problems at different scales was presented. It is particularly useful to study the effects on a macroscale (as wafer bow) to the TSV. It should additionally be noted that the presented method is a special case of the domain decomposition method.

5.4. Strain Relaxation

This section presents the last of the localized stress related problems discussed in this chapter. A discussion regarding the behavior and origin of the intrinsic stress is also initiated, but it will be covered in more detail in Chapter 6. In the last two sections, the impact of the intrinsic stress on the mechanical stability of the TSV became evident. The behavior and build-up of the intrinsic stress on a TSV’s metal layer during thermal cycling is investigated. The system is stressed beyond the elastic limit and a plastic model is required to describe the intrinsic stress evolution. In fact, this plastic deformation will ultimately lead to an overall strain (stress) relaxation, as will be explained later.

5.4.1. Strain Relaxation by Dislocation Glide

During film deposition, different stress sources pressure the material atoms to conform to the substrate and to their environmental conditions. Consequently, the film sustains a strained state and small deformations, also called dislocations, arise in the crystal structure of the deposited material [91]. Dislocations manifest themselves in two forms: edge dislocation and screw dislocation [91]. However, a mix of both types is the most common observation in materials.

Dislocations can propagate through the film due to the actions of an external disturbance. This movement, when sustained, relaxes the film and constitutes one of the main mechanisms of strain relaxation of materials. A fair example of such a phenomenon can be described by considering Fig. 5.17. A dislocation movement is characterized by the breaking of an atomic bond around the defect, followed by a different bond formation. For a system in equilibrium, such processes occur in a random fashion. However, when the system is disturbed by an external force, the crystal lattice deforms elastically, which favors the dislocation propagation in a preferred direction. If the force persists for sufficient time, the defect propagates to the material surface, where boundary effects take place and part of the strained energy inside the film is

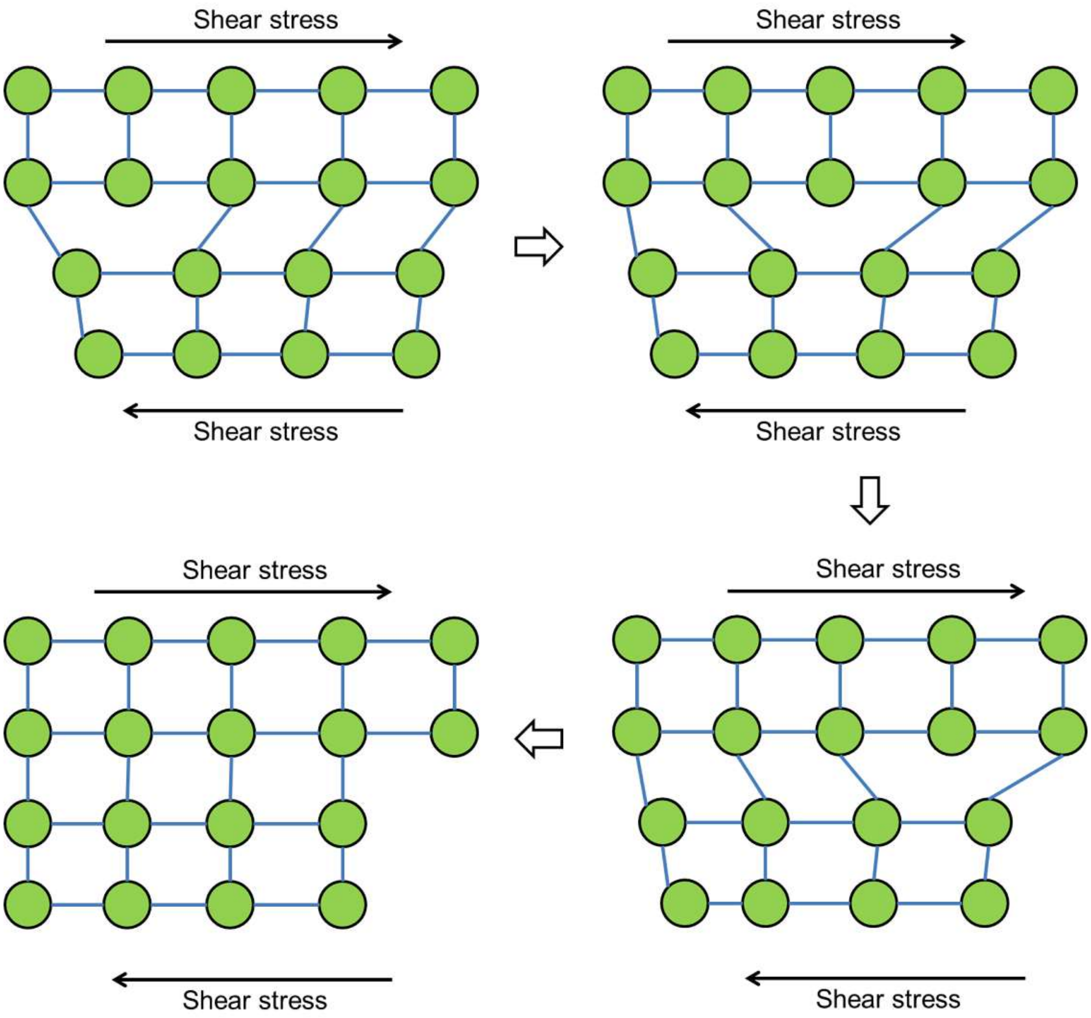

Figure 5.17.: Dislocation propagation inside a film crystal.

released. Consequently, the film experiences a reduced strained state and a reduction in the intrinsic stress.

The continuous propagation of the dislocations depends on several conditions and properties inside the material. As shown in Fig. 5.18, the dislocation moves along the indicated slip plane, following the slip direction [92]. Such slip systems are not available for every plane inside the crystal, but are instead determined by the symmetries of the lattice. Usually, slip planes are defined by the lattice with the highest atom density (closed package configuration) and the slip direction is defined by the shortest distance between atoms on the slip plane [91]. Naturally, the external force must favor the movement of a dislocation in a slip system, otherwise a continuous propagation is very unlikely.

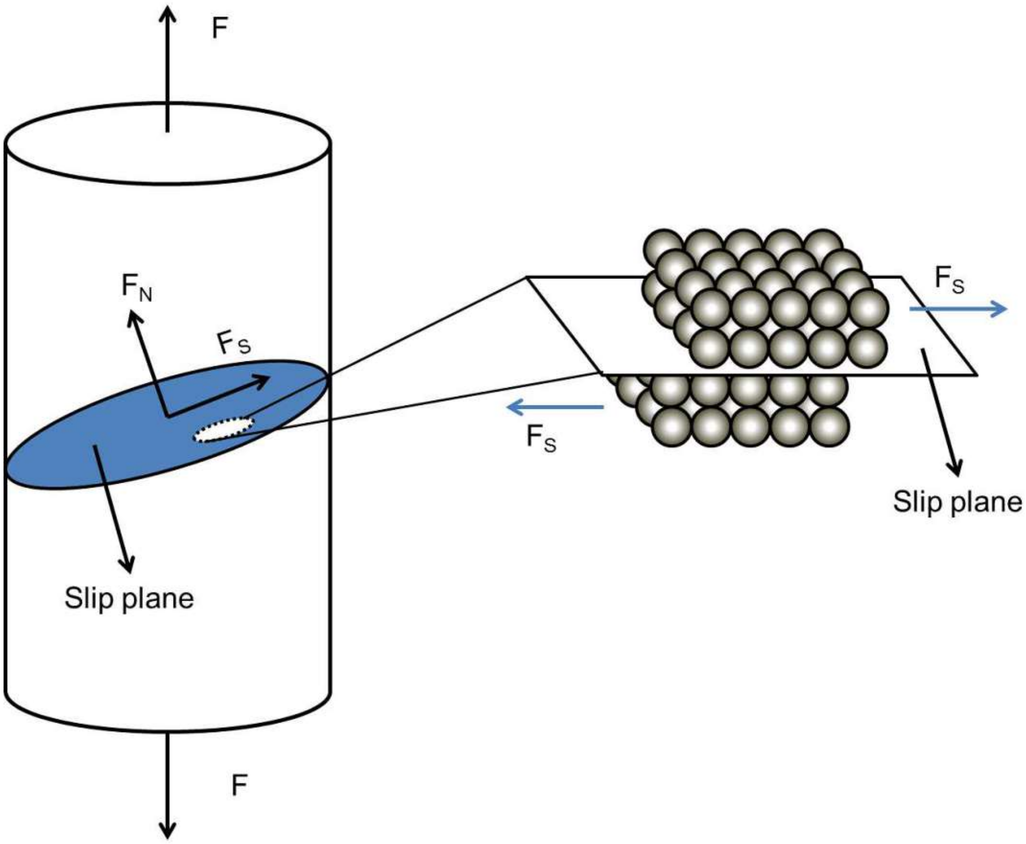

Figure 5.18.: Slip system inside a material. A force parallel to the slip plane must exist in order to activate the dislocations movement.

The dynamic of dislocation glide is not governed solely by the slip system and the external force. Dislocations interact with each other and with grain boundaries during motion. Moreover, the propagation is a kinetic process and temperature effects can not be neglected. In the case of polycrystalline materials, each grain has its own slip system which should be accounted for. All these conditions make the modeling of the dislocation glide a challenging task. Actually, there is a variety of models available, which consider dislocation propagation under different conditions [92]. In general, however, they can be divided into low and high temperature models. The concept of low temperature in this case depends on the melting point of the material. Any temperature below approximately 10% of the material's melting point is usually considered low [92]. This work is limited to the model named after Freund for low temperature dislocation glide with obstacles [92], which is usually a suitable choice for metals present in microelectronic metals' structures[93].

The dislocation movement is by definition a plastic process, since the material changes its structure permanently. As in every plastic process the amount of deformation will depend on the amount of time during which a material must withstand a stress state. Moreover, the deformation is accumulated over time, which means that in order to predict the plastic deformation of an eventual load, the previous amount of plastic deformation should be known in advance. Unfortunately, this information is rarely available. Therefore, it is more convenient to describe plastic deformations by means of their rate over time. This rate is known as strain-rate, which is defined in the model of low temperature dislocation glide with obstacles by

$$\dot{\gamma} = \gamma_0 exp\left[-\frac{\Delta F}{kT}\left(1-\frac{\sigma_s}{\hat{\tau}}\right)\right] \ , \tag{5.3}$$

where γ_0 is a pre-exponential factor assumed to be constant for high values of ΔF, k is the Boltzmann constant, T is the temperature, and σ_s is the shear stress over the material. The symbol ΔF represents the activation energy of an obstacle and it defines the energy needed for the dislocation to overcome a single obstacle without an external force. Lastly, the property $\hat{\tau}$ describes the amount of shear stress required to trigger the dislocation glide without aid from the thermal energy.

5.4.2. Strain Relaxation Driven by Temperature

Temperature variation is one the most common stress sources in metal films of semiconductor devices, especially during processing. Devices are baked several times in thermal cycles which can reach up to 500°C. In such situations, an understanding of the stress evolution in metal films is mandatory to create mechanically stable TSVs.

During thermal variation every deformation (elastic or plastic) in the film is the result of thermal expansion (or contraction) as described by

$$\epsilon_T = \Delta\alpha(T - T_0) = \epsilon_e + \epsilon_p \ , \tag{5.4}$$

where $\Delta\alpha$ stands for the CTE mismatch between the film and substrate, T is the temperature during a thermal cycle, T_0 is the initial temperature, and the indexes T, e, and p refer to thermal, elastic, and plastic strain, respectively. The stress can be related to the strain by Hooke's law as described in Section 2.2.1. However, the film is a 2D system so the relation can be simplified. Additionally, as mentioned in the scallop problem of Section 5.2, an equibiaxial assumption in thin films' analyses is quite common. Hence, the problem dimension can still be further reduced to 1D and Hooke's relation for thin films can be described by

$$\sigma_F = M_f \epsilon_e \ , \tag{5.5}$$

where σ_F is the stress in the film and M_f is known as the biaxial modulus. In order to compute the effects of thermal variation on the stress, ϵ_e in (5.5) must be replaced by (5.4) as in

$$\begin{aligned} \sigma_F &= M_f\left(\epsilon_T - \epsilon_p\right) \\ &= M_f\left[\Delta\alpha(T - T_0)\right] - \epsilon_p \ . \end{aligned} \tag{5.6}$$

For reasons stated in the previous section, it is convenient to describe plastic deformations by means of the time derivative. In principle, the same approach could be applied to (5.6), but for the particular case of thermal variation, an analysis of (5.6) by derivatives of temperature is of greater interest, as in [93]

$$\begin{aligned} \frac{d\sigma_F}{dT} &= M_f\left(\Delta\alpha - \frac{d\epsilon_p}{dT}\right) \\ &= M_f\left(\Delta\alpha - \frac{d\epsilon_p}{dt}\frac{dt}{dT}\right) \ . \end{aligned} \tag{5.7}$$

Substituting (5.3) in (5.7) one obtains the final relation:

$$\frac{d\sigma_F}{dT} = M_f\left(\Delta\alpha\right) - M_f\frac{dt}{dT}\gamma_0 exp\left[-\frac{\Delta F}{kT}\left(1 - \frac{\sigma_s}{\hat{\tau}}\right)\right] \ , \tag{5.8}$$

where the shear stress σ_s relates to the equibiaxial stress by the Schmid factor (s) as in $\sigma_s = s\sigma$.

5.5. Simulation of Stress Behavior in Thermal Cycles

Within this section, the implementation of the model (5.8) will be used to compute the stress evolution in thin films during thermal cycles. The discussion starts with a simple substrate/film system and evolves progressively towards thin films in a TSV, where the equibiaxial assumption is no longer valid.

Consider again the full-plate sample of Fig. 5.1. Krauss et al. placed this sample in a thermal cycle up to 500°C at a rate of 1°C/s and recorded the measured stress at each step. It was inferred from this data, and also from other results of thin film modeling [81][93], that the stress behavior can be explained by the dislocation glide model described in the previous section by (5.8).

5.5.1. Model Parameters

The acquisition of all necessary material parameters for the dislocation glide model is a great challenge. Most of the data available in the literature refer to bulk materials and thin film properties are usually very different. Moreover, the parameters are sensitive to the deposition methods and conditions, which hinder their general usability. Therefore, a safe approach is to obtain the parameters directly from stress measurements in a controlled thermal cycle experiment, as was performed for the presented experiment, in addition to the inclusion of previously available experimental data.

In order to obtain proper values for the material parameters, the dislocation glide model (5.8) must fit the stress measurements [85]. Since (5.8) is a differential equation, traditional fitting techniques based on gradient methods are not suitable. Therefore, a meta-heuristic optimization technique known as Genetic Algorithm (GA) was implemented [94][61]. The goal was to obtain a set of parameters (M_f, ΔF, $\hat{\tau}$, and s), which minimizes the distance between the experimental and the computed stress at various temperatures. Hence, the objective can be described mathematically by

$$\min_{M_f,\Delta F,\hat{tau},s} \sum_i \sigma_E(T_i) - \sigma(T_i) \ , \tag{5.9}$$

where $\sigma_E(T_i)$ is the experimental stress measured at temperature T_i and $\sigma(T_i)$ is the stress computed by (5.8).

One drawback to this approach is the lack of evidence of the uniqueness of the solution of (5.9). This means that there is a chance that two different sets of parameters with different physical meaning can solve (5.9). However, during this work such a situation was not encountered. The obtained parameter values are summarized in Table 5.2. The calculated stress evolution with the obtained parameters is presented in Section 5.5.2 along with a comparison with experimental data.

Table 5.2.: Parameters of the dislocation glide model obtained using a Genetic Algorithm (GA).

Parameter	Value
M_f(GPa)	555.85
ΔF(J)	2.8592×10^{-19}
s	0.2119
$\hat{\tau}$ (GPa)	1.9655

5.5.2. Coupling with FEM

In order to have a thermo-mechanical simulation of the TSV, which properly considers the dislocation glide mechanism described in Section 5.4.2, (5.8) must be included in the thermo-elastic FEM model of the structure. The coupling must consider the breaking of the equibiaxial thin film assumption in the TSV and consequently, the stress computed in Section 5.4.2 must be related to the individual stress components. The relation is given by the associated flow rule:

$$\dot{\epsilon_{ij}} = \frac{\dot{\gamma}}{\sigma}\sigma_{ij} - \frac{1}{3}\delta_{ij}\sum_{k=1..3}\sigma_{kk} \ , \tag{5.10}$$

where ϵ_{ij} are the strain rate tensor components, σ_{ij} are the stress tensor components, and σ is the thin film stress computed by (5.8). It is possible to obtain the individual components of the stress tensor by proceeding with a derivation for each component, similar to that shown for (5.8). Thus, the evolution of the film stress components is described by

$$\frac{d\sigma_{ij}}{dT} = M_{ij}\left(\Delta\alpha\right)\delta_{ij} - M_{ij}\frac{dt}{dT}\dot{\epsilon_{ij}} \ , \tag{5.11}$$

where M_{ij} is the linear constant which relates the elastic strain to the stress (Section 2.2.1). For the normal components, M_{ij} is equal to the biaxial modulus (M_f). The relation (5.11) is the generalization of (5.8) in order to include scenarios where the equibiaxial condition cannot be assured.

The framework described by (5.8), (5.10) and (5.11) summarizes the entire physics required to design a simulation scheme to couple FEM with the dislocation glide model, including the cases where the equibiaxial assumption is not valid. The coupling strategy developed in this work is accomplished with the following procedure:

- Step 1 - Perform a thermo-mechanical elastic simulation of the structure with an initial stress in the tungsten layer.
- Step 2 - Calculate the stress in the tungsten layer for the next temperature by solving (5.11). The result of Step 1 is used as the current stress tensor to obtain $\dot{\epsilon}$.
- Step 3 - Set the initial stress in the tungsten layer with the result of Step 2.
- Step 4 - If the last temperature value is not reached, return to Step 1 and repeat.

The first initial stress in the tungsten layer in Step 1 is taken from an experimental value measured at room temperature (residual stress after deposition) [85]. In Step 2, (5.11) is solved using a backward differentiation formula (BDF) method. The simulation runs through the entire temperature cycle (heating and cooling).

Thermo-mechanical FEM simulations were performed for the standard open TSV and for full-plate sample structures. For the TSVs, scallops were included in the simulation. For both, (5.8) describes only the deformation for the tungsten layer, while the remaining materials are considered to have a simple thermo-elastic behavior.

The purpose of the full-plate simulation is to validate the coupling between the plastic and thermo-elastic model, and also to validate the parameters in Table 5.2. The experience acquired through this simulation regarding assumptions, numerical issues, meshing, and physical interpretation is then applied to the TSV simulation model.

The full-plate simulation was set up with symmetric boundary conditions in order to obtain a result as close as possible to a measurement carried out in the center of the full-plate sample. The computed stress evolution follows very closely the measured values and is only slightly skewed from the GA fitted curve, as shown in Fig. 5.19. This difference can be explained by the mechanical influence of the oxide and the silicon layers. With this simulation, the applied model, the parameter values obtained from the fitting process (Table 5.2), and the coupling scheme between the plastic and the thermo-elastic models were verified. To simulate the stress behavior inside the TSV, an axisymmetric boundary condition was assumed. The analysis was split into two parts due to the particular geometry of the TSV. The first part concerns the top of the TSV and the second part the middle of the TSV.

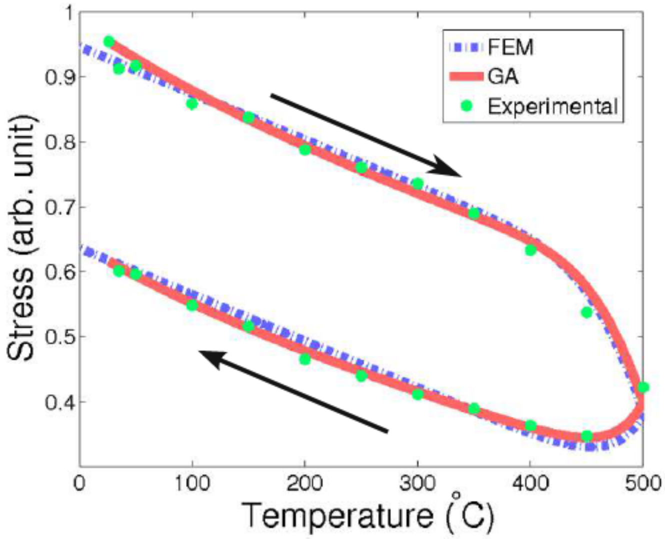

Figure 5.19.: Comparison between experimental data, FEM coupling, and GA fitting result.

TSV Top

The top is distinguished by the additional non-constrained surfaces regularly present above the structure. The stress evolution at the tungsten layer is depicted in Fig. 5.20.

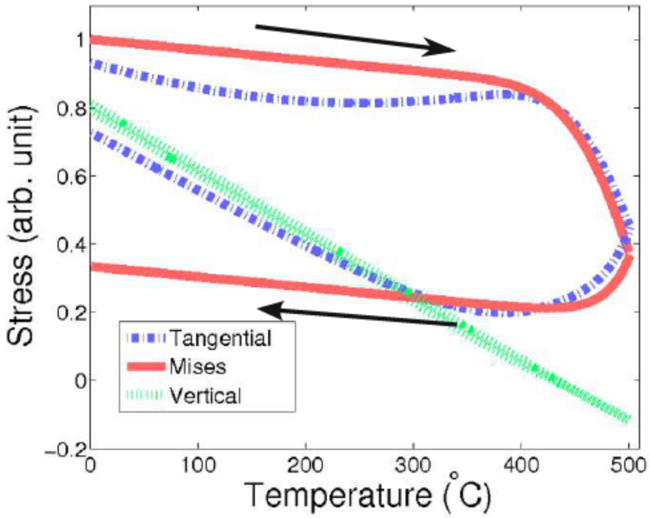

Figure 5.20.: Stress evolution at the TSV top for the metal layer. The stress in the vertical direction sustains an elastic behavior, because the stress level along the thermal cycle is not sufficient to activate the glide mechanism.

Unlike the full-plate sample, in the case of the TSV a highly anisotropic stress distribution is observed. The thermal stress in the cylindrically shaped TSV superposes the expected stress evolution, leading to a fast decline of stress in the vertical direction and a very slow growth on the tangential direction. Hence, the von Mises stress has a peculiar behavior: during heating it follows the upper branch of the stress curve, as the stress component in the vertical direction of the TSV structure, and during the cooling it follows the bottom branch of this curve, as the stress component in the tangential direction.

TSV Middle

The middle of the TSV experiences different effects at the top of the TSV structure. The only non-constrained surface is the TSV sidewall, thus the expansion of the material is more limited and the overall stress increases, as shown in Fig. 5.21. Moreover, during heating, the von Mises stress increases by approximately 10%, instead of decaying as was observed in the full-plate samples. Such an increase could be dangerous for the structure, since the residual stress in the tungsten layer is already very high and an additional tension could surpass the material's ultimate strength, leading to cracks in the metal and a complete failure of the via.

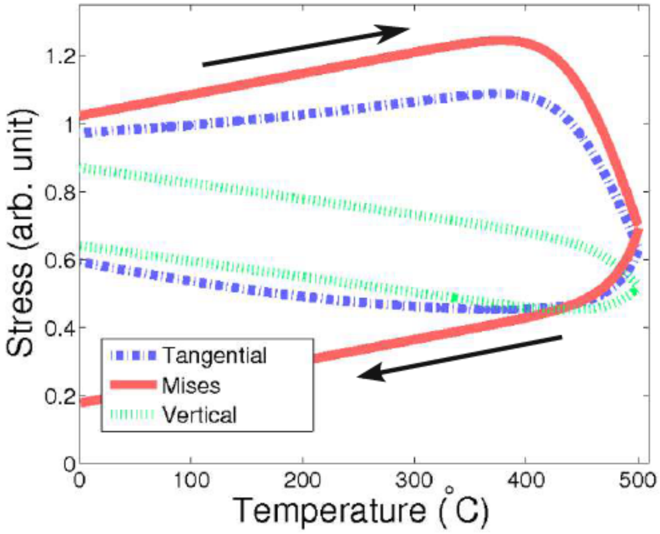

Figure 5.21.: Stress evolution at the TSV middle for the metal layer. The von Mises stress increases during heating and could damage the structure.

5.5.3. Summary and Conclusion

The stress development in the metal layers of the unfilled TSVs during the thermal processing cycle was investigated. A modeling methodology was developed to include low-temperature plastic deformation by dislocation glide in FEM simulations. Additionally, a procedure to obtain the model parameters was described and the parameters for a tungsten thin film were determined. The simulated results were verified through comparison with experiments, proving the validity of the approach. The stress inside the TSV follows a particular evolution due to the influence of geometry deformations during temperature variation. Finally, a critical scenario for the mechanical reliability of the structure was found, which is defined by the valleys between the scallops in the middle of the TSV during the structure heating.

6. Residual Stress in TSVs

In Chapter 5 the local stress of the TSV and the effects of small TSV features were discussed, but the residual stress was given a priori as an embedded property of the material. In this chapter the residual stress is investigated, the prevailing knowledge of its origin is reviewed, and models for its calculation are presented. Based on the calculations a methodology suitable for residual-stress conscious engineering design is provided.

The discussion in this chapter is focused on metal films especially concerning their importance in TSVs. With that in mind, the development of models is much more important for unfilled TSVs, where the thin metal films' behavior has a bigger impact on the overall stress. In filled TSVs, the thin film impact is eclipsed by the stress induced by CTE mismatch which plays the major role in determining the TSV stress. Therefore, the sections to follow study the residual stress due to the deposition of the thin metal films on the sidewall of the unfilled TSVs.

6.1. Growth of Metal Films

Metal films can be deposited using several methods which can be separated in two general groups: chemical vapor deposition (CVD) and physical vapor deposition (PVD) [38][95]. The former comprises the entire range of techniques which use volatile compounds to deliver the metal atoms to the substrate. The different types of CVD depositions are usually distinguished by a particular characteristic of the deposition condition (e.g. low pressure, aerosol assisted deposition, metal organic compounds as precursors, etc.) [95]. In the semiconductor industry, plasma enhanced CVD (PECVD) is widely employed. During PECVD processing, plasma discharges are applied to the film-substrate system during deposition. The high energetic electrons from the plasma enable reactions which would otherwise not be possible at low temperatures. Such features are very important during BEOL, where temperature variations are limited. Furthermore, PECVD is known for increased film adhesion, high deposition rates, and lower resulting deposited film roughness.

PVD includes any technique which utilizes a physical mechanism to transport the metal to the substrate [38]. For example, sputtering is a very popular PVD method in the semiconductor industry. It consists of the ejection of metal atoms from a material source (thin slab) by an inert gas (usually Ar). The atoms of the gas are ionized and accelerated toward the source, the impact causes the release of some metal atoms which travel to the substrate, where they are deposited. The different types of PVD are sorted accordingly to the physical mechanism implemented to release source atoms. In addition to sputtering, evaporation, and electron beam PVD are frequently employed during semiconductor fabrication.

Each deposition method has its advantages and disadvantages. CVD generally has a better step coverage and film quality, but one must deal with hazardous products contained in the chemical reactions. On the other hand, PVD is available for a wider variety of materials (no volatile compound needed) and is more environmental friendly. Ultimately, the deposition method is chosen based on the desired application and eventually financial constraints [66][95][96].

Regardless of the applied deposition technique, thin film growth is a process with at least six fundamental steps [38]:

1. The material is transported to the substrate, where physical interaction takes place and the deposited atoms become weakly attached to the surface.
2. The adatoms – it is common in the literature to refer to atoms which lie in a crystal surface as adatoms – diffuse over the substrate towards low energy sites. Depending on the affinity of the adatoms and the substrate, a chemical bond is formed between them.
3. At this point a cluster of adatoms merges at several locations in order to minimize the system energy, a process known as nucleation.
4. As these agglomerates grow bigger and approach each other, film coalescence occurs. This process takes place, when two or more droplets come in contact during growing and merge to form a continuous material.
5. The islands compete against each other for the arriving adatoms, until the entire substrate is covered. The remaining droplets delineate the grain boundaries, forming the film microstructure.
6. Finally, film deposition ceases and processes, such as grain growth and diffusion, take place, depending on the environmental conditions. The entire process is summarized in Fig. 6.1.

Depending on a material's affinity and environmental conditions, the growth process described above can be carried out in one of three different modes known as Frank-van der Merwe (FM), Volmer-Weber (VW), and Stransky-Krastanov (SK) growth[97]. In FM mode the adatoms are very compatible with the substrate and prefer to attach directly on it, hindering the formation of clusters. Therefore, the film coverage is very smooth and conformal to the substrate. In VW mode the opposite is the case. The interaction between the adatoms of the deposited material is stronger than the interactions of the adatoms and the surface. Consequently, more islands of the deposited material are formed. The SK mode is a mix of FM and VW. In this mode the growth

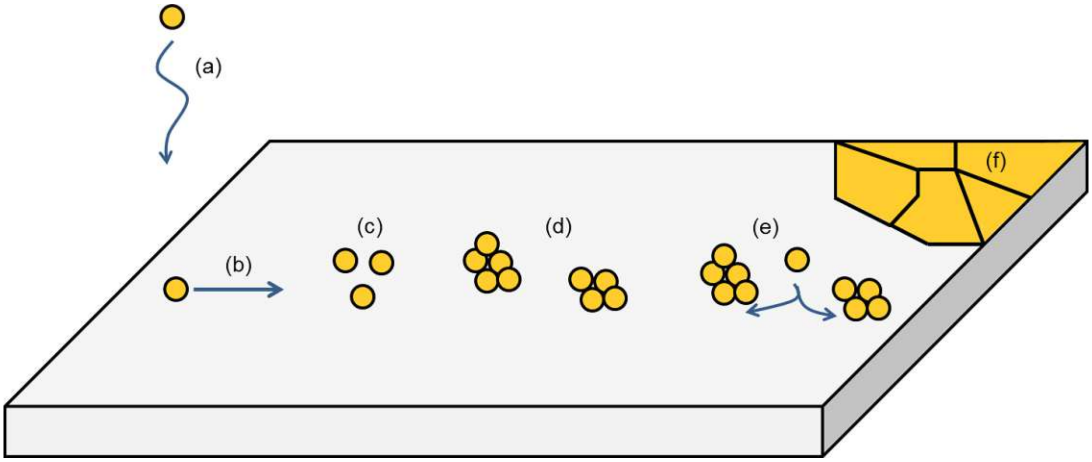

Figure 6.1.: Typical steps during the growth of a thin film. The material is transported towards the substrate (a), where it deposits. The adatoms diffuse (b) over the surface, moving towards low energy sites. As more adatoms arrive, agglomerates begin to form (c) and the first islands nucleate (d). The new arrived adatoms are incorporated into the islands (e), which grow until they reach each other and coalesce, forming the grain boundaries (f).

follows the FM pattern, until the film reaches a critical thickness. When this critical thickness is reached, VM mode takes over and the islands are created as depicted in Fig. 6.2.

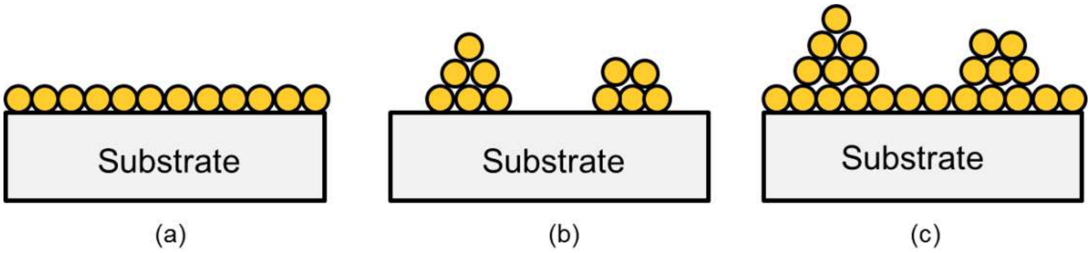

Figure 6.2.: The three modes of film growth: Frank-van der Merwe (a), Volmer-Weber (b), and Stransky-Karastanov (c).

Metals deposited on a surface of silicon dioxide usually form thin films using the Volmer-Weber growth mode [98][99]. In this chapter this will be the only mode considered, since the entire discussion revolves around the residual stress in metal layers of TSVs. For the considered TSV, the metal layer is deposited on a silicon dioxide layer, meaning that the Wolmer-Weber growth model is expected.

6.2. Residual Stress Formation

The focus of this section will remain concentrated on the metal layers used along the TSV sidewall, where high stress can lead to failure of the entire via, especially in the presence of Bosch scallops, as seen in Chapter 5. During metal deposition, stress arises as a result of physical mechanisms which take place during film growth. Those stresses are strongly related to the fabrication process and are known as intrinsic stress or residual stress [98][99][100][101][102][103].

The residual stress can arise from various sources, as suggested in Table 5.1. A misfit between lattice parameters, microstructural modifications (e.g. grain growth, coalescence) and deposition method are examples of the most common residual stress sources [101]. In Volmer-Weber mode, the residual stress builds up since the initial stages of nucleation. The lack of affinity between metal and substrate atoms leads to the retraction of the atoms in the droplets. Therefore, the island becomes compressed and stress is generated from it. The compressive stress increases continually with island growth until coalescence, where the merging process (also known as zipping) joins them and a tensile force arises. As more droplets come together the tensile stress increases very fast, suppressing the compressive component and leaving the film in a high tensile state. At this point the material can have two different behaviors, depending on the adatom mobility. If the material has high adatom mobility (e.g. Cu, Al, Ag), the new adatoms will move towards the grain boundaries, increasing the grain sizes. This grain growth leads to a compressive pressure in the film and counterbalances the coalescence tensile stress. For materials with low mobility, the new adatoms do not move so easily, which diminishes the compressive force triggered by the adatoms movement. A summary of the microstructure evolution is depicted in Fig. 6.3 and the stress evolution along the growth is shown in Fig. 6.4.

6.3. Residual Stress Calculation of a Single Droplet

As described in the previous section there are three stages for stress generation during film growth, but a careful analysis leads to some simplifications. The compressive stress created by nucleation can be neglected for engineering purposes, because of its small contribution to the eventual state of the thin film. Therefore, coalescence and grain growth define the residual stress of the film. For low adatom mobility metals, the effects of grain growth on the stress can also be ignored and the final state is solely determined by the stress developed during coalescence.

The importance of coalescence stress is reflected in the variety of models in the literature, which attempt to explain it [101]. Three models are broadly known in the scientific community either by their precision or by their physical meaning. Each model will be explicitly presented in the following sections.

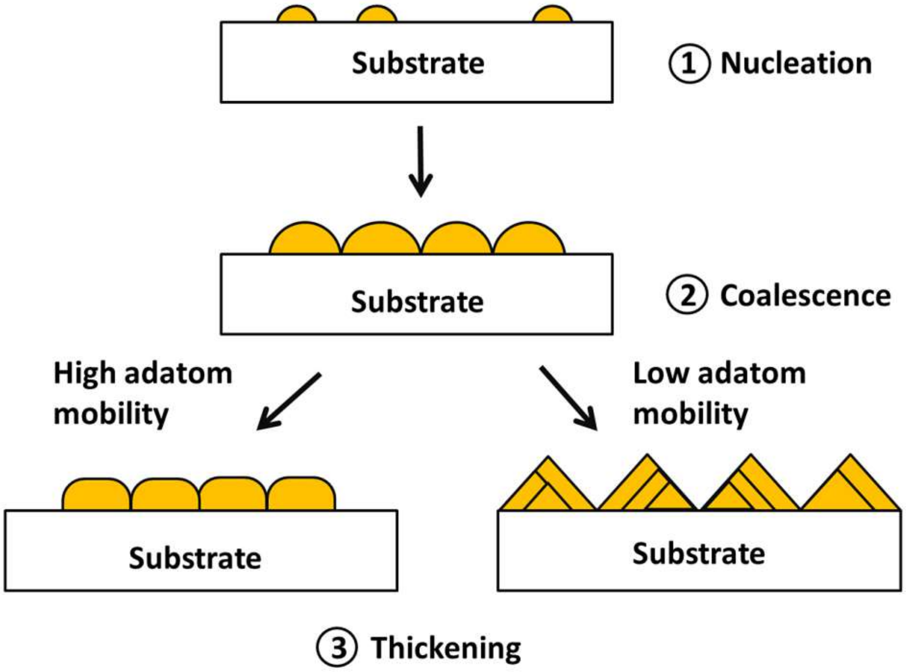

Figure 6.3.: Metal film growth process. The final film structure depends on the adatom mobility of the depositing metal.

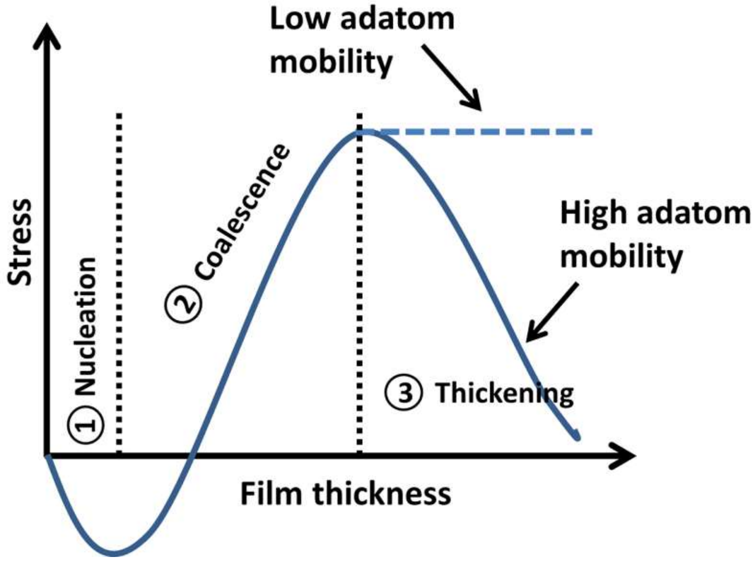

Figure 6.4.: Stress behavior during the film growth process.

6.3.1. Hoffman's Model

Hoffman was the first to acknowledge the energy balance of the coalescence stress formation [104]. He realized that adjacent islands snap together, in order to minimize the free surface energy at the cost of an increased elastic energy. He claimed that the zipping process (islands merging) takes place, when the distance between the islands reach a critical distance (Δ). Nix reviewed Hoffman's work and added a simplified geometry model as depicted in Fig. 6.5.

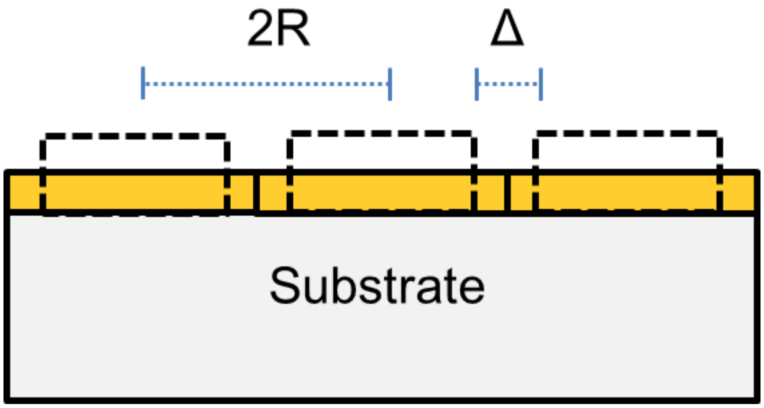

Figure 6.5.: Hoffman model.

Nix restated Hoffman's theory by looking into the energy balance of two islands before and after impingement [105]. Before impingement, the system free energy is given by

$$E_1 = E_0 - 2\gamma_{sv} \ , \tag{6.1}$$

where E_0 is the free surface energy per unit area of the top surface of the film and the substrate/film interface, and γ_{sv} is the free surface energy per unit area of the islands' lateral surfaces. After islands merge the system free energy is given by

$$E_2 = E_0 + \gamma_{gb} + M_f \left(\frac{\Delta}{2R} \right)^2 \ . \tag{6.2}$$

Before island impingement there are two independent surfaces, one for each island, with an amount of energy per surface area of γ_{sv}. After impingement part of the surfaces energy ($2\gamma_{sv}$) is exerted for the formation of the interface between them (grain boundary). This energy amount per unit area is represented by γ_{gb}. The remainder of the surface free energy is converted by the islands' stretching with elastic energy, which is represented by the second term of (6.2). Actually, this is just the conservation of the free energy ($E_2 - E_1 = 0$), which can be used to calculate Δ. The resulting Δ is

$$\Delta = \left[4R \left(2\gamma_{sv} - \gamma_{gb} \right) \frac{1-\nu}{E} \right]^{1/2} . \tag{6.3}$$

The coalescence stress can then be computed from Hooke's law using Δ as in

$$\sigma = M_f \left(\frac{\Delta}{2R} \right) = \left[M_f \frac{2\gamma_{sv} - \gamma_{gb}}{2R} \right]^{1/2} . \tag{6.4}$$

Hoffman's model overestimates the coalescence stress in the film, mainly because of the simple geometry assumed for the islands. However, it is a reasonable approach for low adatom materials. Moreover, it is a simple model when compared to the alternatives and it can be useful as a quick estimate of the upper bound of the coalescence stress.

6.3.2. Nix-Clemens Model

Nix and Clemens employed a different geometry for describing the droplets [105]. They considered islands with an elliptical shape which coalesces to form a cycloid shape surface as depicted in Fig. 6.6.

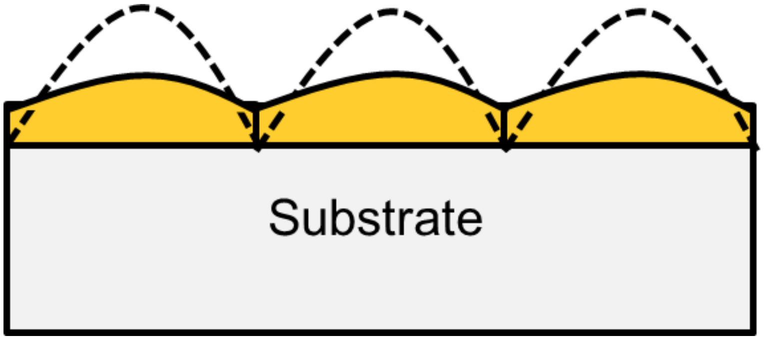

Figure 6.6.: Nix-clemens model.

Instead of a critical distance (Δ), there is a critical height (z_0) in Nix's and Clemens' approach. It defines the extension of the interface between the two islands.

In addition to the island shape, Nix and Clemens adopted a different view of the problem. They treated each cusp of the cycloid surface as a crack and developed their model based on this assumption. Their main argument was that the amount of the energy which must be supplied to grow the crack further (strain energy release rate) must be equal to the amount of energy left after boundary formation $(2\gamma_{sv} - \gamma_{gb})$. Their idea can be neatly summarized by

$$G_R = (1-\nu)^2 \frac{K_f^2}{E} = (2\gamma_{sv} - \gamma_{gb}) \ , \tag{6.5}$$

where G_R is the strain energy release rate and K_f is the stress intensity factor which is used as a parameter to estimate the stress around a cracked tip. Nix and Clemens used $K_f = \frac{1}{1+\nu}\sigma\sqrt{2R}$ from the results of Cheng-Hsin's and Huajian's work regarding cycloid surfaces [106]. Hence, (6.5) can be further developed and the average film stress is given by

$$\sigma = \left[\frac{1+\nu}{1-\nu} E \frac{2\gamma_{sv} - \gamma_{gb}}{2R}\right]^{1/2} \ . \tag{6.6}$$

The Nix-Clemens model also overestimates the stress, but it is based on a more realistic geometry. The criticism of Nix-Clemens' model lies in the loose description of the zipping process. It was assumed by Nix and Clemens that the average stress is linearly dependent on the average strain. However, island coalescence is not an instantaneous process and the problem configuration, as well as the average stress, changes during the zipping process. In such cases the assumptions made by Nix and Clemens would be invalid.

6.3.3. Freund-Chason Model

Freund and Chason took a completely different approach for the islands' encounter [107]. They treated the problem using the Hertzian contact theory with cohesive attraction [108], in an attempt to overcome the deficiencies in the description of the zipping process by Nix and Clemens. The geometry of the problem was also changed; in fact, they claim that the conditions in the Nix-Clemens model are suitable in the case of a fully covered substrate while the depositing material is only filling gaps. Therefore, Freund and Chason proposed a change in the perspective of the problem. Instead of using a transversal cross section, they decided to analyze the process using a top view of the structure, as shown in Fig. 6.7.

In fact, the Freund-Chason model expands the dimensionality of the problem and a 3D description of the geometry is also possible. The stress estimation using the Freund-Chason model is given by

$$\frac{\sigma}{E} = A_N \left(\frac{2\gamma_{sv} - \gamma_{gb}}{Ea}\right)^{c_N} , \qquad N = 1, 2, 3 \ , \tag{6.7}$$

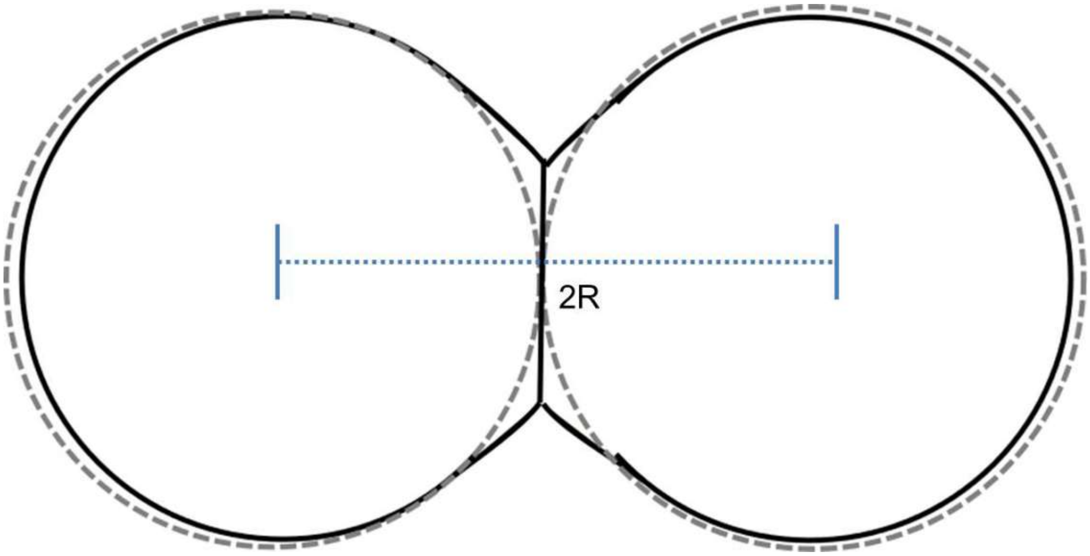

Figure 6.7.: Freund-chason model.

where N is the problem dimensionality. A_N and c_N are parameters which depend on the stated problem dimension with values $A_1 = 0.82$, $A_2 = 0.44$, $A_3 = 4$, and $c_1 = 1/2$, $c_2 = 2/3$, $c_3 = 1$. The Freund-Chason model is more in line with experimental measurements, especially for materials with high adatom mobility.

6.4. FEM Calculations of Residual Stress in Single Droplets

Seel developed a FEM approach for the encounter of two islands discussed in the previous section [98][99]. He posed the problem in the same manner as Nix and Clemens and from his simulations he calculated a height Z_0, which minimizes the coalescence energy. By doing so, he imposed a series of displacements in both droplets' surfaces toward the center and computed the coalescence height which minimizes the energy per unit length of the island surfaces. A sketch is shown in Fig. 6.8.

A semi-analytical solution for Z_0 was also developed in Seel's work. He took an approach similar to Hoffman, but instead of assuming free energy conservation, he considered the total energy per unit length of the island interfaces, which is given by

$$E_{total} = \frac{1}{2}EY_0 - (2\gamma_s v - \gamma_g b)Z_0 \ , \tag{6.8}$$

where $Z_0 = [(r/sin\theta)^2 - (r - Y_0)^2]^{(1/2)}$. The first term is the elastic energy which Seel obtained by fitting the FEM results in different contact angles. As in the Hoffman

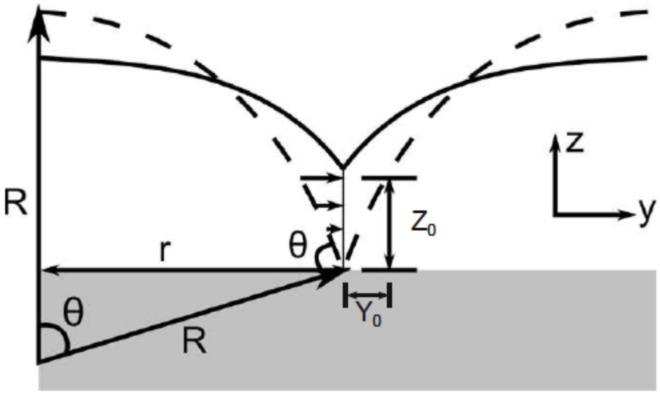

Figure 6.8.: Structure considered for coalescence simulations. The droplets come in contact at a height Z_0 and the surface is displaced at most by Y_0. The angle formed between the droplet and the deposition substrate is identified by θ. Image based on [98].

model, the second term represents the available energy after the creation of grain boundaries. In contrast to Hoffman's model, Seel's analysis does not require energy conservation, because the analysis is restricted to the interface of the islands. However, if the entire system is considered, the energy must be obviously conserved.

The minimum energy point defines the coalescence height Z_0. Although it is possible to obtain an analytical solution for Z_0 from (6.8) ($dE_{total}/dZ_0 = 0$), it is very cumbersome and a numerical treatment is preferable. Seel's approach is very flexible, presents results similar to the Freund-Chason model with a slight tendency for underestimation, and is very suitable for engineering purposes.

6.5. Residual Stress Estimation

The stress in a single droplet does not characterize the stress of the entire film. Each droplet coalesces with a different size along the metal, which leads to different stress magnitudes in each droplet. In this work a statistical approach is presented to obtain the average stress along the film. Furthermore, the impact of process parameters is included in the final estimation.

6.5.1. One-Dimensional Volmer-Weber Growth Simulation

The estimation procedure developed here begins with a 1D simulation of the Volmer-Weber growth process for the TSV metal [99][109]. The purpose is to identify the island size distribution for a given set of growth parameters. The droplets are placed randomly over a substrate following a pre-established nucleation distribution which defines the amount of droplets per unit length. All droplets are considered to appear instantaneously at the beginning of the growth process. It is not an optimal assumption, but further improvements are left for future work. The island growth with time is given by

$$\frac{dR}{dt} = \frac{\sin\theta^3}{(1-\cos\theta)^2(2+\cos\theta)} D_R \ , \tag{6.9}$$

where R is the island radius, θ is the contact angle, and D_R is the deposition rate in units of length per time. Here, a constant deposition rate was employed in the range between 1nm/s and 3nm/s, thus the island radius in each instant can be obtained by a simple multiplication of the right hand side of (6.9) by the time. A nucleation rate of 0.01 nuclei per nanometer is assumed. In Fig. 6.9 a snapshot of the simulation evolution at one instant in time is shown.

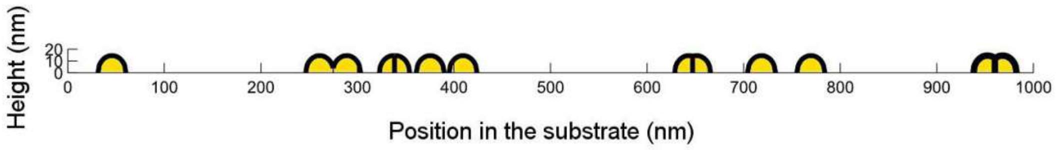

Figure 6.9.: Snapshot of the VW simulation used in this section. The grains will grow until the entire substrate is covered.

During the VW growth simulation each island's encounter characterizes an event. At every time step the simulation algorithm looks for an event occurrence. When one is found, the islands' sizes are stored and the islands are marked as merged. In future time steps, the intersection points of the merged islands are computed and a boundary is defined at the line between the intersection point and the substrate, as depicted in Fig. 6.8.

The simulation is terminated, when every droplet has at least one encounter and the entire substrate is covered. At this point the histogram of the island size at first encounter is calculated and a distribution curve can be fitted. It follows an exponential decay as expected. A histogram, resulting from a sample simulation, is sketched in Fig. 6.10.

6.5.2. Coalescence Simulation

After a VW growth simulation, a sample is taken from the droplet size distribution and a FEM simulation is performed in order to compute the stress. The setup follows Seel's scheme, but Z_0 is not computed from the FEM simulations; instead the numerical minimization of (6.8) regarding Z_0 is used. This approach is faster, because it avoids extra FEM simulations in the search for Z_0. A FEM simulation example of a grain encounter is shown in Fig. 6.11.

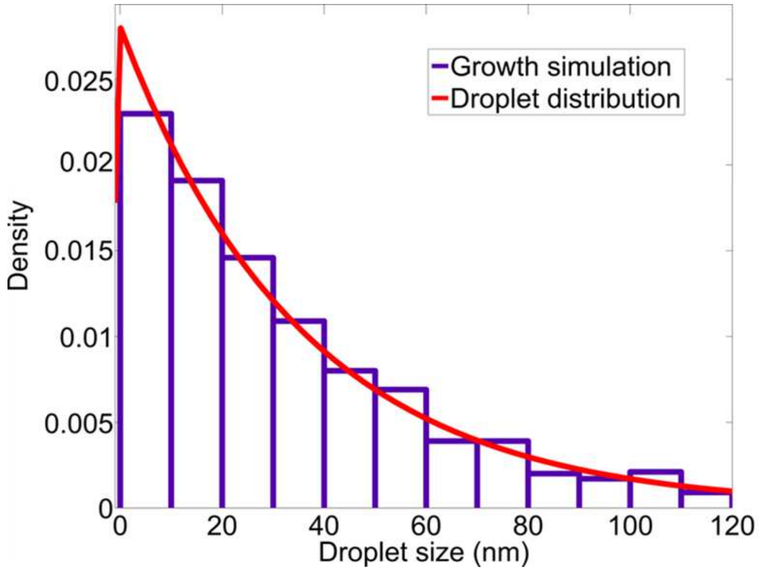

Figure 6.10.: Droplet size distribution during coalescence for the growth parameters considered in this work. The droplets' sizes follow an exponential distribution.

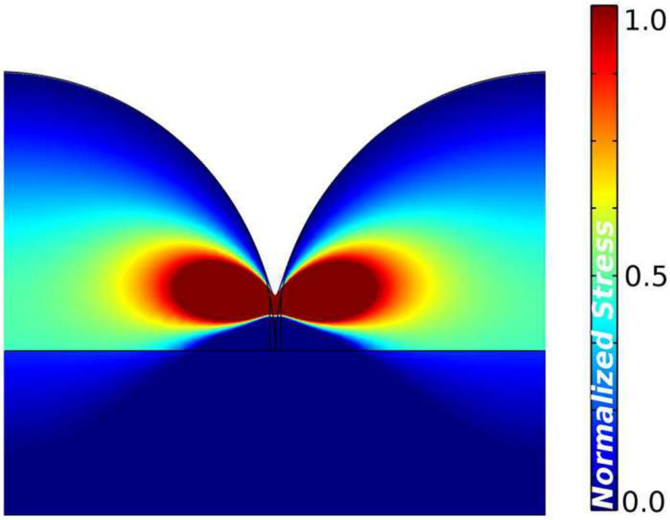

Figure 6.11.: FEM simulation of a single encounter between two droplets. Symmetry conditions are employed from both sides. A prescribed displacement is applied at the surface of both grains up to a critical height Z_0.

The calculated stresses are then averaged and the entire process is repeated for a new sample from the droplets' size distribution, until it reaches statistical significance (usually in the order of several thousand simulations). Finally, an estimate for the average stress in the film can be calculated together with the confidence interval. The method is summarized in Fig. 6.12.

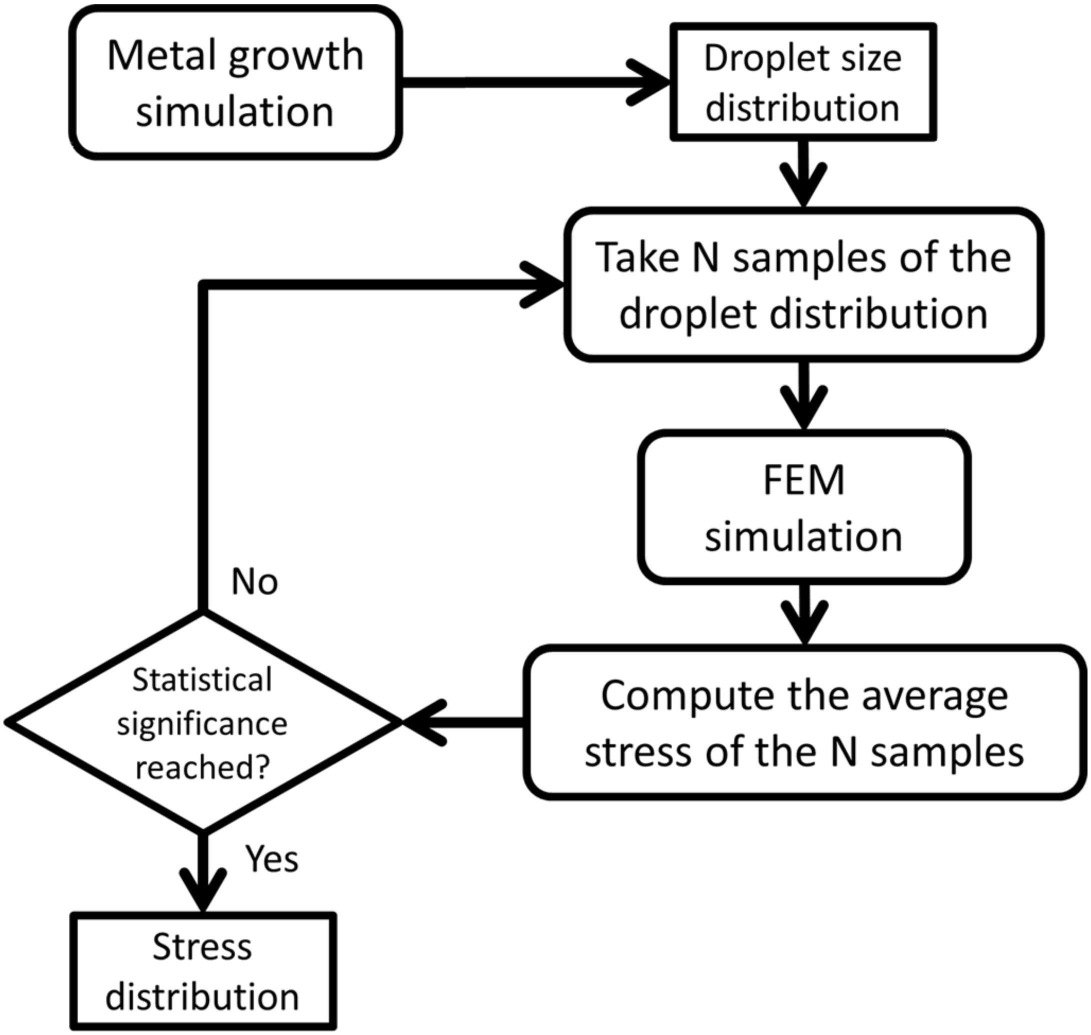

Figure 6.12.: Method to estimate the average residual stress.

6.5.3. Stress Estimate

The grain size determines the final intrinsic stress magnitude (in materials with low adatom mobility) as can be seen from Fig. 6.4. Bigger grains lead to smaller stress generation and smaller grains lead to higher stress generation [99]. The resulting grain size and distribution is affected by several processing and material parameters. However, a process engineer can control – to some extent – the grain size distribution only by the growth rate and the nucleation distribution (rate). Thus, the intrinsic stress can be engineered, in principle, solely by those two parameters. All processing steps after deposition have been neglected for this study, which may also alter the microstructure of the material (e.g. annealing). A summary of the models which discuss those processes can be found in a previous work [99].

The results obtained from the simulation were compared to the stress measurements of tungsten films (low adatom mobility material)[85] as depicted in Fig. 6.13. The mean of the distribution is the estimate for the residual stress and the distribution spreading is the expected deviation of the estimate.

There is a tendency for the experimental data to lie above the estimated average stress. This fact can be explained by a possibly undervalued nucleation distribution of the tungsten, which could lead to overestimated averages. Nevertheless, more measurements are needed to confirm this tendency. In summary, given a set of growth parameters, the presented methodology provides the most probable interval, where the average residual stress due to coalescence can lie, and the most likely value for the residual stress in low adatom mobility metal thin films. In the case of high mobility materials the compressive component after coalescence must be introduced, but the procedure remains unchanged.

The problem of residual stress estimation requires a statistical approach due to the random character of the coalescence process. Additionally, the obtained confidence interval provides to the engineer a safeguard for the design of the TSVs. Naturally, further improvements are needed such as 3D simulations (VW growth and FEM), non-instantaneous island nucleation, and variable deposition rate.

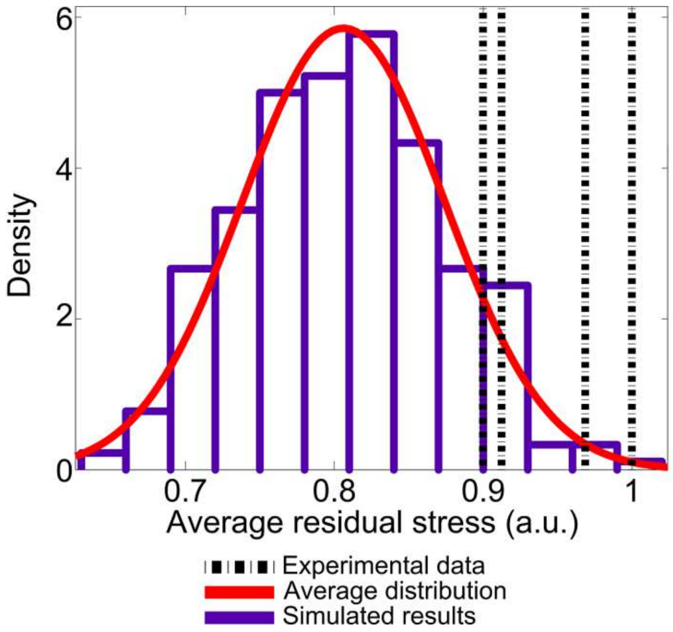

Figure 6.13.: Residual stress estimation. The simulated results follow a normal distribution. The mean is the residual stress estimate and the distribution spreading is the expected deviation from the estimate.

6.5.4. Summary and Conclusion

A methodology to estimate the residual stress of a metal film with low adatom mobility was presented. The problem requires a statistical approach due to the random characteristic of the coalescence process. A 1D simulation of the Volmer-Weber growth process is performed and a droplets' size distribution is generated from this simulation. The distribution is then used as an input of an iterative process including finite element simulations, in order to obtain an average stress in the film considering different droplet sizes. The estimate was compared to previous experimental work. The simulated results suggest a tendency for underestimation, although it cannot be entirely confirmed due to the small number of experimental data available.

7. Summary and Outlook

Three-dimensional integration is a very likely alternative to proceed with more-than-Moore device integration. The variety of advantages granted by the technology works as a stimulus for the industry to move in this direction. Furthermore, the technology is rather compatible with current processing techniques, reducing the cost for initial production. However, the implementation of 3D technology is not straightforward, especially for the manufacture of reliable devices.

Mass production of highly integrated devices is not yet a reality, but for some market niches 3D integration with through silicon vias is already in production. A great deal of effort has been placed on the further development of this technology. However, several different aspects must be properly addressed, such as yield, thermal management, mechanical stability, testing, and design, before mass production becomes a reality.

This work provides a theoretical contribution to surpass the mechanical challenges of fabrication and operation of TSVs. The stress in TSVs was investigated in depth under different scenarios. It is not always possible to understand experimentally the mechanical behavior of TSVs. Therefore, simulation and analysis techniques must be used in parallel to support and explain the observed behavior. The simulations were kept as close as possible to realistic conditions, and experimental data was used extensively when available. A high degree of caution must be followed, in spite of the past successes of various simulation techniques, because it is not uncommon for some detail to be overlooked during modeling.

The FEM was mainly implemented to approach the problems and develop models addressed here. Within FEM, a series of techniques were developed to enable or to improve the analysis. Initially, the stress generation for a TSV was studied and an analytic description for the stress was developed. It compares nicely to FEM results for stresses around the middle of the via. Furthermore, the analytical solution can also serve the purpose of a safe lower bound estimate for the stress in the via top and bottom. The combination of stress fields of a group of TSVs were also investigated and a methodology to improve the placement of TSVs was presented. The objective was to find the best TSV layout which will reduce the overall stress in the silicon surrounding the TSV structures.

In addition, the TSV was analyzed locally. Previous experimental data pointed out a stress reduction along the TSV's sidewall, where Bosch scallops were present. A simulation scheme was created considering an approximation for the scallop form. The geometry of the scallops were identified as the most likely cause for this stress reduction. Furthermore, the effects of the scallop geometry for the stress along the via was investigated. So far, it is well known that the stress depends on the scallops' shape, and a careful description of the scallops' geometry is needed. A better approach is to use topography simulations of the Bosch process, but simulation time is the main restriction for this approach.

Within the scope of local stress effects, the impact of wafer handling on the TSV was investigated. The forced "unbow" of wafers was simulated during a mechanical chuck down. This type of simulation has structures with a large aspect ratio and large variation in length scales. A wafer diameter is usually in the range of hundreds of millimeters, while the biggest dimension of a TSV is less than a tenth of a millimeter. To address properly such a situation, a hierarchical scheme was proposed. The results showed that unfilled TSVs are more susceptible to mechanical instability in this situation. The metal in filled TSVs provides a good protection against movements which have a direct impact at the bottom of the TSV.

In the sequence, strain relaxation in the metal layers during thermal cycling was presented as the last of the local stress investigations. Experimental measurements of stress in full-plate samples during thermal cycles were used to characterize the plastic behavior of the metal films of a TSV. The challenge here was to obtain a model which could be used to predict the stress inside the TSV. A previous model, low temperature dislocation glide, was used to explain the stress measurements. However, the model depends on parameters which are not readily available. Moreover, due to the particularities of the model, traditional fitting techniques are of no use. The problem was overcome by applying a meta-heuristic search algorithm know as Genetic Algorithm. The procedure was restrained, as much as possible, to produce physically meaningful results. A very good match with experimental data was obtained. Subsequently, a scheme to couple the thermo-elastic FEM simulations with the calibrated model was developed. Hence, a full simulation of a TSV considering the scallops could be carried out to study the stress inside the TSV. The results revealed a particular evolution for the stress inside the via. The top and the middle of the via show different behaviors, the middle being the most dangerous region. There, the stress increases during heating and can reach values up to 10% larger than the initial stress.

Finally, the discussion moved down along the length scale in order to study mechanical stress during thin film deposition. The residual stress creation was studied, considering the microstructural evolution of the metal during growth. The coalescence was assumed as the only mechanism for generating stress during growth. Several models were discussed to compute the stress which is generated by the encounter of two islands. However, the stress due to coalescence is not a product of only one island encounter, instead it is the result of the impingement of islands with different sizes. Therefore, a statistical approach was proposed, in which the size distribution of the islands in a film was taken into consideration for the final stress of the film. As a result, the methodology provided an estimate for the residual stress due to coalescence in addition to the confidence interval for the stress variation.

This work has provided an assortment of simulation techniques for analysis of the mechanical stress in TSVs. Each technique was created to address a specific circumstance during the via processing or operation. Naturally, further improvement is required and some issues are already known. The first one is the improvement of the scallop description. Some unpublished results have shown that the description of the scallops by Bézier curves is not the best approach, mainly because of the peaks created at the scallop intersections. A connection between scallops made by a soft curve could improve the results. Regarding strain relaxation, it is known that the coupled scheme does not work for nonlinear variations of temperature. Modifications in the strain relaxation model are necessary in order to consider these problems. Finally, the estimate for residual stress must include other stress sources. In fact, it is surprising that it was possible to obtain a simulated value so close to the observed values by only considering the coalescence and thermal effects. Furthermore, improvements to the VW simulation are also needed, for instance, one should consider non-instantaneous nucleation of islands. The quality of the solution produced by the simulations depends greatly on the quality of the input data. This is especially true for microstructure simulations, where the availability of material parameters is very limited.

Appendix A.

Properties and Identities of First and Second Rank Tensors

Several operations and identities of first and second order tensors are defined below for fast consulting. The same notation of the main text is used. The capitalized letters (U, S, T) refer to tensors and the amount of bars above them identifies the tensor ranking. The bold lower case letters ($\mathbf{u}$, $\mathbf{v}$) refer to vectors, while the not bold letters are real numbers, except for f which refer to a real function.

Addition

$$\bar{\bar{U}} = \bar{\bar{S}} + \bar{\bar{T}} = \bar{\bar{T}} + \bar{\bar{S}} \rightarrow U_{ij} = S_{ij} + T_{ij} \tag{A.1}$$

Product of a Tensor and a Vector

$$\mathbf{v} = \bar{\bar{\mathbf{S}}}\mathbf{u} \rightarrow \mathbf{v_i} = \mathbf{S_{ij}u_j} \tag{A.2}$$

$$\mathbf{v} = \mathbf{u}\bar{\bar{\mathbf{S}}} \rightarrow \mathbf{v_j} = \mathbf{u_j S_{ji}} \tag{A.3}$$

Product of two Tensors

$$\bar{\bar{U}} = \bar{\bar{S}} \cdot \bar{\bar{T}} \rightarrow U = S_{ik}T_{kj} \tag{A.4}$$

Transpose

$$\bar{\bar{S}}^T \equiv \begin{bmatrix} S_{11} & S_{21} & S_{31} \\ S_{12} & S_{22} & S_{32} \\ S_{13} & S_{23} & S_{33} \end{bmatrix} \tag{A.5}$$

Trace

$$trace(\bar{\bar{S}}) = S_{11} + S_{22} + S_{33} \tag{A.6}$$

Inner Product

$$\bar{\bar{S}} : \bar{\bar{T}} = \sum_{\substack{1<i<n \\ 1<j<m}} S_{ij} T_{ij} \tag{A.7}$$

Tensor Product

$$\mathbf{u} \otimes \mathbf{v} \equiv \mathbf{u}\mathbf{v}^{\mathbf{T}} = \begin{pmatrix} u_1 \\ u_2 \\ u_3 \end{pmatrix} \begin{pmatrix} v_1 & v_2 & v_3 \end{pmatrix} = \begin{pmatrix} u_1 v_1 & u_1 v_2 & u_1 v_3 \\ u_2 v_1 & u_2 v_2 & u_2 v_3 \\ u_3 v_1 & u_3 v_2 & u_3 v_3 \end{pmatrix} \tag{A.8}$$

$$\mathbf{u} \otimes \mathbf{v} = \sum_{\mathbf{i=1}}^{\mathbf{n}} \sum_{\mathbf{j=1}}^{\mathbf{m}} \mathbf{a_i b_j u_i} \otimes \mathbf{v_j} \tag{A.9}$$

In A.9 the vectors $\mathbf{u_i}$ and $\mathbf{v_i}$ are basis of the space of $\mathbf{u}$ and $\mathbf{v}$ respectively.

Tensor Identities

$$\nabla \cdot (\nabla \times \bar{U}) = 0 \tag{A.10}$$

$$\nabla \cdot (\Delta \bar{U}) = \Delta(\nabla \cdot \bar{U}) \tag{A.11}$$

$$\nabla \cdot (f\bar{U}) = f\nabla \cdot \bar{U} + \bar{U} \cdot \nabla f \tag{A.12}$$

$$\nabla \cdot (\bar{U} \wedge \bar{V}) = \bar{V} \cdot \nabla \times \bar{U} - \bar{U} \cdot \nabla \times \bar{V} \tag{A.13}$$

$$\nabla \cdot (\nabla \bar{\bar{U}}) = \Delta \bar{U} \tag{A.14}$$

$$\nabla \cdot (\nabla \bar{\bar{U}})^t = \nabla (\nabla \cdot \bar{U}) \tag{A.15}$$

$$\nabla \cdot (\bar{U} \otimes \bar{V}) = \bar{U} \nabla \cdot \bar{V} + \nabla \bar{\bar{U}} \cdot \bar{V} \tag{A.16}$$

$$\nabla \cdot (f \bar{\bar{T}}) = f \nabla \cdot \bar{\bar{T}} + \bar{\bar{T}} \cdot \nabla f \tag{A.17}$$

$$\nabla \cdot (\bar{\bar{T}} \cdot \bar{U}) = (\nabla \cdot \bar{\bar{T}} \cdot \bar{U})^t + \bar{\bar{T}} : \nabla \bar{\bar{U}} \tag{A.18}$$

$$\nabla \cdot (f \bar{\bar{I}}) = \nabla f \tag{A.19}$$

$$\nabla \times (\nabla \times \bar{U}) = \nabla (\nabla \cdot \bar{U}) - \Delta \bar{U} \tag{A.20}$$

$$\nabla \times (\Delta \bar{U}) = \Delta (\nabla \times \bar{U}) \tag{A.21}$$

$$\nabla \times (f \bar{U}) = f \nabla \times \bar{U} + \nabla f \wedge \bar{U} \tag{A.22}$$

$$\nabla \times (\bar{U} \wedge \bar{V}) = \nabla \bar{\bar{U}} \cdot \bar{V} + \bar{U} \nabla \cdot \bar{V} - \bar{V} \nabla \cdot \bar{U} - \nabla \bar{\bar{V}} \cdot \bar{U} \tag{A.23}$$

$$\nabla (\bar{U} \cdot \bar{V}) = \nabla \bar{\bar{U}} \cdot \bar{V} + \nabla \bar{\bar{V}} \cdot \bar{U} + \bar{U} \wedge \nabla \times \bar{V} + \bar{V} \wedge \nabla \times \bar{U} \tag{A.24}$$

$$\nabla \bar{\bar{U}} \cdot \bar{U} = \nabla \times \bar{U} \wedge \bar{U} + \nabla \frac{U^2}{2} \tag{A.25}$$

Bibliography

[1] S. Budiansky, *Battle of Wits: the Complete Story of Codebreaking in World War II*. Simon and Schuster, 2000.

[2] E. Braun, *Revolution in Miniature: the History and Impact of Semiconductor Electronics*. Cambridge University Press, 1982.

[3] F. Kaplan, *1959: The Year Everything Changed*. John Wiley & Sons, 2009.

[4] T. J. Bergin, “50 years of army computing from ENIAC to MSRC,” DTIC Document, Tech. Rep., 2000.

[5] A. Randall, “Q&A: A lost interview with ENIAC co-inventor J.Presper Eckert,” *Computerworld*, vol. 5, p. 2009, 2006. [Online]. Available: http://www.computerworld.com/s/article/print/108568/Q_A_A_lost_interview_with_ENIAC_co_inventor_J._Presper_Eckert

[6] NobelMedia. (2003, May) The history of the integrated circuit. Nobelprize.org. [Online]. Available: http://www.nobelprize.org/educational/physics/integrated_circuit/history/

[7] B. Lojek, *History of Semiconductor Engineering*. Springer, 2007.

[8] J. S. Kilby, “Method of making miniaturized electronic circuits,” US Grant US 3 261 081 A, July 19, 1966. [Online]. Available: http://www.google.com/patents/US3261081

[9] J. Kilby, “Miniaturized electronic circuits,” US Grant US3 138 743 A, June 23, 1964. [Online]. Available: http://www.google.com/patents/US3138743

[10] K. Lehovec, “Multiple semiconductor assembly,” US Grant US 3 029 366 A, April 10, 1962. [Online]. Available: http://www.google.com/patents/US3029366

[11] J. A. Hoerni, “Semiconductor device,” US Grant US 3 064 167 A, November 13, 1962. [Online]. Available: http://www.google.com/patents/US3064167

[12] NobelMedia. (2013, December) The Nobel prize in physics 2000. Nobelprize.org. [Online]. Available: http://www.nobelprize.org/nobel_prizes/physics/laureates/2000/

[13] G. Moore. (2005, April) Moore’s law. Intel corp. [Online]. Available: http://www.intel.com/pressroom/kits/events/moores_law_40th/

[14] Intel. Desktop processors - intel product information. Intel corp. [Online]. Available: http://ark.intel.com/

[15] M. Dubash. (2005, April) Moore's law is dead, says Gordon Moore. Techworld. [Online]. Available: http://news.techworld.com/operating-systems/3477/moores-law-is-dead-says-gordon-moore/

[16] W. Nawrocki, "Physical limits for scaling of integrated circuits," in *Journal of Physics: Conference Series*, vol. 248, no. 1. IOP, 2010.

[17] T. Osada and M. Godwin, "International technology roadmap for semiconductors," ITRS, Tech. Rep., 2010.

[18] M. Haselman and S. Hauck, "The future of integrated circuits: A survey of nanoelectronics," *Proceedings of the IEEE*, vol. 98, no. 1, pp. 11–38, 2010.

[19] K.-S. Yeo and K. Roy, *Low Voltage, Low Power VLSI Subsystems*. McGraw-Hill, 2004.

[20] L. R. Harriott, "Limits of lithography," *Proceedings of the IEEE*, vol. 89, no. 3, pp. 366–374, 2001.

[21] R. F. Pease and S. Y. Chou, "Lithography and other patterning techniques for future electronics," *Proceedings of the IEEE*, vol. 96, no. 2, pp. 248–270, 2008.

[22] G. Brewer, *Electron-beam Technology in Microelectronic Fabrication*. Elsevier, 2012.

[23] J. Fischer and M. Wegener, "Three-dimensional optical laser lithography beyond the diffraction limit," *Laser & Photonics Reviews*, vol. 7, no. 1, pp. 22–44, 2013.

[24] K. Banerjee, A. Amerasekera, G. Dixit, and C. Hu, "The effect of interconnect scaling and low-k dielectric on the thermal characteristics of the IC metal," in *International Electron Devices Meeting (IEDM)*. IEEE, 1996, pp. 65–68.

[25] J. J.-Q. Lu and K. Rose, "3D integration: Why, what, who, when?" *Future Fab Intl.*, vol. 23, pp. 25–27, 2007.

[26] S. Wong, A. El-Gamal, P. Griffin, Y. Nishi, F. Pease, and J. Plummer, "Monolithic 3D integrated circuits," in *International Symposium on VLSI Technology, Systems and Applications (VLSI-TSA)*. IEEE, 2007, pp. 1–4.

[27] P. Batude, M. Vinet, A. Pouydebasque, C. Le Royer, B. Previtali, C. Tabone, J.-M. Hartmann, L. Sanchez, L. Baud, V. Carron *et al.*, "Advances in 3D CMOS sequential integration," in *International Electron Devices Meeting (IEDM)*. IEEE, 2009, pp. 1–4.

[28] S.-M. Jung, H. Lim, K. H. Kwak, and K. Kim, "A 500-MHz DDR high-performance 72-Mb 3-D SRAM fabricated with laser-induced epitaxial c-Si growth technology for a stand-alone and embedded memory application," *IEEE Transactions on Electron Devices*, vol. 57, no. 2, pp. 474–481, 2010.

[29] J. Kraft, F. Schrank, J. Teva, J. Siegert, G. Koppitsch, C. Cassidy, E. Wachmann, F. Altmann, S. Brand, C. Schmidt *et al.*, "3D sensor application with open through silicon via technology," in *Electronic Components and Technology Conference (ECTC).* IEEE, 2011, pp. 560–566.

[30] A. Papanikolaou, D. Soudris, and R. Radojcic, *Three Dimensional System Integration.* Springer, 2011, ch. 2.

[31] S. W. Yoon, D. W. Yang, J. H. Koo, M. Padmanathan, and F. Carson, "3D TSV processes and its assembly/packaging technology," in *International Conference on 3D System Integration (3DIC).* IEEE, 2009, pp. 1–5.

[32] S. C. Johnson, "Via first, middle, last, or after?" *3D Packaging* , vol. 13 , pp. 2–5 , December 2009.

[33] S. Cho, "Technical challenges in TSV integration to Si," in *SEMATECH Symposium*, Korea, 2011.

[34] H. Yoshikawa, A. Kawasaki, Y. Nishimura, K. Tanida, K. Akiyama, M. Sekiguchi, M. Matsuo, S. Fukuchi, K. Takahashi, and others , "Chip scale camera module (CSCM) using through-silicon-via (TSV) ," in *International Solid-State Circuits Conference-Digest of Technical Papers (ISSCC) .* IEEE, 2009, pp. 476–477.

[35] D. Henry, F. Jacquet, M. Neyret, X. Baillin, T. Enot, V. Lapras, C. Brunet-Manquat, J. Charbonnier, B. Aventurier, and N. Sillon, "Through silicon vias technology for CMOS image sensors packaging," in *Electronic Components and Technology Conference (ECTC).* IEEE, 2008, pp. 556–562.

[36] J. Knickerbocker, P. Andry, E. Colgan, B. Dang, T. Dickson, X. Gu, C. Haymes, C. Jahnes, Y. Liu, J. Maria *et al.*, "2.5D and 3D technology challenges and test vehicle demonstrations," in *Electronic Components and Technology Conference (ECTC).* IEEE, 2012, pp. 1068–1076.

[37] G.-Q. Zhang, W. van Driel, and X. Fan, *Mechanics of Microelectronics.* Springer, 2006, vol. 141, ch. 4.

[38] L. B. Freund and S. Suresh, *Thin Film Materials: Stress, Defect Formation and Surface Evolution.* Cambridge University Press, 2003.

[39] A. F. Bower, *Applied Mechanics of Solids.* CRC Press, 2011.

[40] E. A. de Souza Neto, D. Peric, and D. R. J. Owen, *Computational Methods for Plasticity: Theory and Applications.* John Wiley & Sons, 2011, ch. 3.

[41] T. M. Atanackovic and A. Guran, *Theory of Elasticity for Scientists and Engineers.* Springer, 2000.

[42] L. N. Trefethen and D. Bau III, *Numerical Linear Algebra.* Siam, 1997, vol. 50.

[43] MatWeb LLC. (2014, January) Tungsten, W properties. MatWeb - Materials Property Data. [Online]. Available: http://www.matweb.com/search/DataSheet.aspx?MatGUID=41e0851d2f3c417ba69ea0188fa570e3

[44] MatWeb LLC. (2014, January) Copper, Cu cold drawn properties. MatWeb - Materials Property Data. [Online]. Available: http://www.matweb.com/search/DataSheet.aspx?MatGUID=1980eb23287a4408adc404dd39293942

[45] E. Török, A. Perry, L. Chollet, and W. Sproul, "Young's modulus of TiN, TiC, ZrN and HFn," *Thin Solid Films*, vol. 153, no. 1, pp. 37–43, 1987.

[46] A. Perry, "A contribution to the study of poisson's ratios and elastic constants of TiN, ZrN and HF," *Thin Solid Films*, vol. 193, pp. 463–471, 1990.

[47] MatWeb LLC. (2014, January) Titanium nitride (TiN) coating properties. MatWeb - Materials Property Data. [Online]. Available: http://www.matweb.com/search/datasheet.aspx?MatGUID=ffbf753c500949db95e502e043f9a404&ckck=1

[48] Eagle alloys corp. (2014, January) Tantalum - physical properties. Eagle Alloys Corporation. [Online]. Available: http://www.eaglealloys.com/t-tantalumproperties.html

[49] F. Cverna, *ASM Ready Reference: Thermal Properties of Metals.* ASM International, 2002, chapter 2.

[50] F. Cardarelli, *Materials Handbook: a Concise Desktop Reference.* Springer, 2008.

[51] D. Rees, *Basic Engineering Plasticity: an Introduction with Engineering and Manufacturing Applications.* Butterworth-Heinemann, 2006.

[52] M. A. Hopcroft, W. D. Nix, and T. W. Kenny, "What is the Young's modulus of silicon?" *Journal of Microelectromechanical Systems*, vol. 19, no. 2, pp. 229–238, 2010.

[53] R. Electronics, *Semiconductor Reliability Handbook.* Renesas Electronics, 2008.

[54] T. L. Anderson, *Fracture Mechanics: Fundamentals and Applications.* CRC Press, 2005.

[55] J. Gere and B. Goodno, *Mechanics of Materials.* Cengage Learning, 2008, p. 238.

[56] C. Johnson, *Numerical Solution of Partial Differential Equations by the Finite Element Method.* Dover Publications, 2012.

[57] O. Zienkiewicz, R. Taylor, and J. Zhu, *The Finite Element Method: its Basis and Fundamentals.* Butterworth-Heinemann, 2005.

[58] K. H. Huebner, D. L. Dewhirst, D. E. Smith, and T. G. Byrom, *The Finite Element Method for Engineers*. John Wiley & Sons, 2008, p. 81.

[59] S. C. Brenner and L. R. Scott, *The Mathematical Theory of Finite Element Methods*. Springer, 2008, vol. 15.

[60] P. Frey and P.-L. George, *Mesh Generation*. John Wiley & Sons, 2010, vol. 32.

[61] T. Gowers, J. Barrow-Green, and I. Leader, *The Princeton Companion to Mathematics*. Princeton University Press, 2010.

[62] A. Jeffrey and D. Zwillinger, *Table of Integrals, Series, and Products*. Elsevier, 2007, p. 1055.

[63] R. J. LeVeque, *Finite Difference Methods for Ordinary and Partial Differential Equations: Steady-State and Time-Dependent Problems*. Siam, 2007.

[64] K. E. Atkinson, *An Introduction to Numerical Analysis*. John Wiley & Sons, 2008.

[65] C. Harper, *Electronic Packaging and Interconnection Handbook*. McGraw-Hill, 2004, ch. 4.

[66] S. Wolf, *Silicon Processing for the VLSI Era: Deep-Submicron Process Technology, Vol. 4*. Lattice Press, 2002.

[67] MatWeb LLC. (2014, January) Aluminum, Al properties. MatWeb - Materials Property Data. [Online]. Available: http://www.matweb.com/search/DataSheet.aspx?MatGUID=0cd1edf33ac145ee93a0aa6fc666c0e0

[68] MatWeb LLC. (2014, January) Platinum silicide, PtSi properties. Matweb - Material Property Data. [Online]. Available: http://www.matweb.com/search/DataSheet.aspx?MatGUID=d6858030449d4d8887aa2c4623f2b0de

[69] MatWeb LLC. (2014, January) Titanium silicide, TiSi2 properties. Matweb - Material Property Data. [Online]. Available: http://www.matweb.com/search/DataSheet.aspx?MatGUID=eb5a8f94115b4d919a5f5f21fe503e22

[70] N. Stavitski, “Silicide-to-silicon specific contact resistance characterization: test structures and models,” Ph.D. dissertation, University of Twente, 2009.

[71] MatWeb LLC. (2014, January) Cobalt silicide, CoSi2 properties. Matweb - Material Property Data. [Online]. Available: http://www.matweb.com/search/DataSheet.aspx?MatGUID=f8a93e43a88b4eb3acea7d7d25a9b34c

[72] Y. Nishi and R. Doering, *Handbook of Semiconductor Manufacturing Technology*, 2nd ed. CRC Press, 2012.

[73] K. Tuck, A. Jungen, A. Geisberger, M. Ellis, and G. Skidmore, “A study of creep in polysilicon MEMS devices,” *Journal of Engineering Materials and Technology*, vol. 127, no. 1, pp. 90–96, 2005.

[74] S. P. Murarka and S. W. Hymes, "Copper metallization for ULSL and beyond," *Critical Reviews in Solid State and Material Sciences*, vol. 20, no. 2, pp. 87–124, 1995.

[75] P. C. Andricacos, "Copper on-chip interconnections," *The Electrochemical Society Interface*, vol. 8, no. 1, p. 6, 1999.

[76] G. Brase, K. Lynne Holloway, and U. P. Schroeder, "Via first dual damascene process for copper metallization," WO Application WO2 002 003 457 A3, June 6, 2002. [Online]. Available: https://www.google.com/patents/WO2002003457A3?cl=en&dq=copper+dual+damascene+ibm&hl=de&sa=X&ei=3cH3UriyLeTY7Aa-uoCQAw&ved=0CDYQ6AEwAA

[77] A. Pratt, "Overview of the use of copper interconnects in the semiconductor industry," Advanced Energy Industries, Inc., Tech. Rep., 2004.

[78] M. J. Wolf, T. Dretschkow, B. Wunderle, N. Jurgensen, G. Engelmann, O. Ehrmann, A. Uhlig, B. Michel, and H. Reichl, "High aspect ratio TSV copper filling with different seed layers," in *Electronic Components and Technology Conference (ECTC)*. IEEE, 2008, pp. 563–570.

[79] M. Koyanagi, "3D integration technology and reliability," in *International Reliability Physics Symposium (IRPS)*. IEEE, 2011, pp. 3F–1.

[80] K. Takahashi and M. Sekiguchi, "Through silicon via and 3-D wafer/chip stacking technology," in *Symposium on VLSI Circuits*, ser. Digest of Technical Papers. IEEE, 2006, pp. 89–92.

[81] S. Chen, T. V. Baughn, Z. J. Yao, and C. L. Goldsmith, "A new in situ residual stress measurement method for a MEMS thin fixed-fixed beam structure," *Journal of Microelectromechanical Systems*, vol. 11, no. 4, pp. 309–316, 2002.

[82] K. H. Lu, X. Zhang, S.-K. Ryu, J. Im, R. Huang, and P. S. Ho, "Thermo-mechanical reliability of 3-D ICs containing through silicon vias," in *Electronic Components and Technology Conference (ECTC)*. IEEE, 2009, pp. 630–634.

[83] A. P. Singulani, H. Ceric, and S. Selberherr, "Thermo-mechanical simulations of an open tungsten TSV," in *Electronics Packaging Technology Conference (EPTC)*. IEEE, 2012, pp. 107–111.

[84] C. Cassidy, J. Kraft, S. Carniello, F. Roger, H. Ceric, A. P. Singulani, E. Langer, and F. Schrank, "Through silicon via reliability," *IEEE Transactions on Device and Materials Reliability*, vol. 12, no. 2, pp. 285–295, 2012.

[85] C. Krauss, S. Labat, S. Escoubas, O. Thomas, S. Carniello, J. Teva, and F. Schrank, "Stress measurements in tungsten coated through silicon vias for 3D integration," *Thin Solid Films*, vol. 530, pp. 91–95, 2013.

[86] M. F. Doerner and W. D. Nix, “Stresses and deformation processes in thin films on substrates,” *Critical Reviews in Solid State and Material Sciences*, vol. 14, no. 3, pp. 225–268, 1988.

[87] A. Faraji, *Elastic and Elastoplastic Contact Analysis: Using Boundary Elements and Mathematical Programming.* WIT Press, 2005.

[88] M. Duncan, *Applied Geometry for Computer Graphics and CAD.* Springer, 2005.

[89] G. Janssen, M. Abdalla, F. Van Keulen, B. Pujada, and B. Van Venrooy, “Celebrating the 100th anniversary of the Stoney equation for film stress: Developments from polycrystalline steel strips to single crystal silicon wafers,” *Thin Solid Films*, vol. 517, no. 6, pp. 1858–1867, 2009.

[90] A. Toselli and O. B. Widlund, *Domain Decomposition Methods: Algorithms and Theory.* Springer, 2005, vol. 34.

[91] D. Hull and D. J. Bacon, *Introduction to Dislocations.* Butterworth-Heinemann, 2001.

[92] H. J. Frost and M. F. Ashby, *Deformation Mechanism Maps: the Plasticity and Creep of Metals and Ceramics.* Pergamon Press, 1982.

[93] D. Weiss, “Deformation mechanisms in pure and alloyed copper films,” Ph.D. dissertation, Universität Stuttgart, 2000.

[94] D. E. Goldberg, *Genetic Algorithms in Search, Optimization, and Machine Learning.* Addison-Wesley, 1989.

[95] D. M. Dobkin and M. K. Zuraw, *Principles of Chemical Vapor Deposition.* Springer, 2003.

[96] D. L. Smith, *Thin-Film Deposition: Principles and Practice.* McGraw-Hill, 1995.

[97] A. Pimpinelli and J. Villain, *Physics of Crystal Growth.* Cambridge University Press, 1998, vol. 11.

[98] S. C. Seel and C. V. Thompson, “Tensile stress generation during island coalescence for variable island-substrate contact angle,” *Journal of Applied Physics*, vol. 93, no. 11, pp. 9038–9042, 2003.

[99] S. C. Seel, “Stress and structure evolution during Volmer-Weber growth of thin films,” Ph.D. dissertation, Massachusetts Institute of Technology, 2002.

[100] A. Rajamani, B. W. Sheldon, E. Chason, and A. F. Bower, “Intrinsic tensile stress and grain boundary formation during Volmer–Weber film growth,” *Applied Physics Letters*, vol. 81, no. 7, pp. 1204–1206, 2002.

[101] J. A. Floro, E. Chason, R. C. Cammarata, and D. J. Srolovitz, "Physical origins of intrinsic stresses in Volmer–Weber thin films," *MRS Bulletin*, vol. 27, no. 01, pp. 19–25, 2002.

[102] R. Cammarata, T. Trimble, and D. Srolovitz, "Surface stress model for intrinsic stresses in thin films," *Journal of Materials Research* , vol. 15 , no. 11 , pp. 2468–2474, 2000.

[103] R. Koch, "The intrinsic stress of polycrystalline and epitaxial thin metal films," *Journal of Physics: Condensed Matter*, vol. 6, no. 45, p. 9519, 1994.

[104] R. Hoffman, "Stresses in thin films: The relevance of grain boundaries and impurities," *Thin Solid Films*, vol. 34, no. 2, pp. 185–190, 1976.

[105] W. Nix and B. Clemens, "Crystallite coalescence - a mechanism for intrinsic tensile stresses in thin films ," *Journal of Materials Research* , vol. 14 , no. 8 , pp. 3467–3473, 1999.

[106] G. Cheng-Hsin, Chiu and Huajian, "Stress singularities along a cycloid rough surface," *International Journal of Solids and Structures*, vol. 30 , no. 21 , pp. 2983–3012, 1993.

[107] L. Freund and E. Chason, "Model for stress generated upon contact of neighboring islands on the surface of a substrate," *Journal of Applied Physics*, vol. 89, no. 9, pp. 4866–4873, 2001.

[108] K. L. Johnson and K. L. Johnson, *Contact Mechanics*. Cambridge University Press, 1987.

[109] C. V. Thompson, "On the grain size and coalescence stress resulting from nucleation and growth processes during formation of polycrystalline thin films," *Journal of Materials Research*, vol. 14, no. 07, pp. 3164–3168, 1999.

List of Publications

[1] A. P. Singulani, H. Ceric, and S. Selberherr, "Stress evolution in the metal layers of TSVs with Bosch scallops," *Microelectronics Reliability* , vol. 53, no. 9, pp. 1602–1605, 2013.

[2] H. Ceric, A. P. Singulani, R. Orio, and S. Selberherr, "Impact of intermetallic compound on solder bump electromigration reliability," in *International Conference on Simulation of Semiconductor Processes and Devices (SISPAD).* IEEE, 2013, pp. 73–76.

[3] A. P. Singulani, H. Ceric, and E. Langer, "Stress reduction induced by Bosch scallops on an open TSV technology," in *International Interconnect Technology Conference (IITC).* IEEE, 2013, pp. 1–2.

[4] A. P. Singulani, H. Ceric, L. Filipovic, and E. Langer, "Impact of Bosch scallops dimensions on stress of an open through silicon via technology," in *International Conference onThermal, Mechanical and Multi-Physics Simulation and Experiments in Microelectronics and Microsystems (EuroSimE).* IEEE, 2013, pp. 1–6.

[5] A. P. Singulani, H. Ceric, and E. Langer, "Stress evolution on tungsten thin-film of an open through silicon via technology," in *International Symposium on the Physical and Failure Analysis of Integrated Circuits (IPFA).* IEEE, 2013, pp. 212–216.

[6] A. P. Singulani, H. Ceric, and S. Selberherr, "Stress estimation in open tungsten TSV," in *International Conference on Simulation of Semiconductor Processes and Devices (SISPAD).* IEEE, 2013, pp. 65–68.

[7] A. P. Singulani, H. Ceric, E. Langer, and S. Carniello, "Effects of Bosch scallops on metal layer stress of an open through silicon via technology," in *International Reliability Physics Symposium (IRPS)* . IEEE , 2013, pp. CP–2.

[8] C. Cassidy, J. Kraft, S. Carniello, F. Roger, H. Ceric, A. P. Singulani, E. Langer, and F. Schrank, "Through silicon via reliability," *IEEE Transactions on Device and Materials Reliability*, vol. 12, no. 2, pp. 285–295, 2012.

[9] A. P. Singulani, H. Ceric, and S. Selberherr, "Thermo-mechanical simulations of an open tungsten TSV," in *Electronics Packaging Technology Conference (EPTC).* IEEE, 2012, pp. 107–111.

Curriculum Vitae

Aug. 2002 – June 2007
State University of Rio de Janeiro, Rio de Janeiro - RJ, Brazil
Bachelor of Electrical Engineering

Aug. 2007 – July 2009
Pontifical Catholic University of Rio de Janeiro, Rio de Janeiro - RJ, Brazil
Graduate program in nanotechnology at the Dept. of Electrical Engineering
Masters's Thesis: "Simulation and Design of GaAs/AlGaAs Quantum Well Solar Cells Aided by Genetic Algorithm"

Aug. 2007 – April. 2011
Pontifical Catholic University of Rio de Janeiro, Rio de Janeiro - RJ, Brazil
Research Assistant at the Dept. of Electrical Engineering

Since April. 2011
Vienna University of Technology, Austria
PhD program at the Institute for Microelectronics

Since July. 2013
ams AG, Austria
TCAD Engineer at Dept. of Process Development and Integration